The evolution of galaxies in massive clusters

Stott, John Philip

The Evolution of Galaxies in Massive Clusters

John Philip Stott

A Thesis presented for the degree of
Doctor of Philosophy

Extragalactic Astronomy
Department of Physics
Durham University
UK

September 2007

Dedicated to

My Parents

for their constant love and support

The Evolution of Galaxies in Massive Clusters

John Philip Stott

Submitted for the degree of Doctor of Philosophy

September 2007

Abstract

We present a study of the evolution of galaxies in massive X-ray selected clusters across half the age of the Universe. This encompasses galaxies on the red sequence from the Brightest Cluster Galaxy (BCG) to the faint red population.

We begin at the tip of the red sequence with an investigation into the near infrared evolution of BCGs since z =1. By comparing the BCG Hubble diagram and near-infrared colour evolution to a set of stellar population and semi-analytic models we constrain the evolution and formation redshift of these massive galaxies.

Moving down in luminosity from the BCG, in chapter 3 we study the build up of the red sequence in massive clusters. To achieve this we compare the luminosity functions for red galaxies in a homogeneous sample of ten X-ray luminous clusters at $z \sim 0.5$ to a similarly selected X-ray cluster sample at $z \sim 0.1$. We quantify this result by measuring the dwarf to giant ratio to ascertain whether faint galaxies have joined the red sequence over the last 5 Gyr.

In chapter 4 we study the evolution of the red sequence slope in massive clusters from z=1 to present day. We compare our observed slope evolution to that predicted from semi-analytical models based on the Millennium simulation. We also look for trends between the red sequence slope and other cluster observables, such as X-ray luminosity, to investigate whether this will effect cluster detection methods which search for a colour-magnitude relation.

In the final science chapter we present the details of our own cluster detection algorithm. This simple algorithm is based on finding clusters through the near-infrared and optical properties of the red sequence, drawing on our galaxy cluster evolution research. We describe the application of the algorithm to object catalogues from the UKIDSS DXS fields in order to find clusters at $z \sim$1. To confirm the presence of the clusters we employ deep multi-object spectroscopy on the photometric members. The clusters found in this study are fed back into the high redshift regime of our galaxy evolution research.

Declaration

The work in this thesis is based on research carried out at the Extragalactic Astronomy Group, Department of Physics, Durham University, UK. No part of this thesis has been submitted elsewhere for any other degree or qualification and it is all my own work unless referenced to the contrary in the text.

Acknowledgements

I would first of all like to thank my supervisor Alastair Edge for his support, help and advice over the past 3 years and above all for giving me the opportunity to study towards a PhD in the first place. A PhD interview conducted in the pub with galaxy rotation curves drawn on beer mats is something I'll never forget! Thanks also go to Ian Smail for his patience and assistance in my first publication and to Mark Swinbank for showing me how to use a number of pieces of unwieldy astronomy software.

This thesis is dedicated to my parents for their love, support and understanding throughout my education. I must also give a huge thanks to Nicola for her love and motivation during the completion of this thesis.

Throughout my PhD I have greatly enjoyed the company of my fellow postgrads and postdocs. I must firstly thank Jim my office mate extradonaire without whom the last 3 years in room 311 would have been much less entertaining. And in order of current proximity to room 311, thanks go to Dave, Rich, Jim 2, Norris, Booth, Rob, Greg and finally Nic.

Final thanks go to Kevin Pimbblet and Graham Smith for useful input and scientific discussions throughout my PhD. I would also like to acknowledge financial support through a Particle Physics and Astronomy Research Council Studentship.

Contents

List of Figures

List of Tables

Chapter 1

Introduction

1.1 History of astronomy

Astronomy is often referred to as the oldest of the sciences and dates back to prehistory. The first naked eye astronomers were able to observe the motion of the Sun, Moon, stars and bright planets across the sky. Cycles such as the Sun crossing the sky once a day, the Moon waxing and waning over a period of 28 days and the regularity of the seasons formed the basis for the first calendars. These calendars probably also relied on more sophisticated observations such as the first appearances of certain constellations and bright stars during the year. Astronomical calendars were extremely important to ancient agricultural communities for they would signal the times of year to plant and harvest their crops.

We know from early historical texts that ancient Greek philosophers and mathematicians had a keen interest in studying the heavens. Using geometry they were able to provide mathematical descriptions for the motions of celestial bodies. The philosopher Plato's (427–347 BC) understanding of the Universe was that the earth was at the centre with all other heavenly bodies in a complex system of concentric spheres around it. This model was improved over the centuries by Hipparchus

(190–120 BC) and others with the spheres removed to be replaced by circular orbits. These orbits themselves had extra embedded circular orbits called epicycles to account for the observed motion of the planets.

The ancient Greek geocentric view of astronomy remained in European society for almost two millennia until the time of the Renaissance. It was in this period of scientific and cultural revolution that the Polish astronomer Nicolaus Copernicus broke with the conventional view and proposed a heliocentric system. In 1543 Copernicus gave a full mathematical treatment of this system using the geometric techniques of the ancient Greeks. With the invention of the telescope, astronomers such as Galileo Galilei were able to provide observations to bolster the heliocentric model.

Astronomy and physics were first combined at a fundamental level by Isaac Newton. In the work Philosophiae Naturalis Principia Mathematica (published 1687) he set out his law of universal gravitation. This law showed that all objects with mass were mutually attracted. He was then able to derive Johannes Kepler's empirical laws of planetary motion from first principles, demonstrating their effectiveness.

1.2 Modern cosmology

In the early 20th century the galaxies where considered to be nebulae within the Milky Way. Astronomers noticed that 'spiral nebulae' appeared to have spectral features similar to those seen in stars or in the laboratory but shifted to longer wavelengths. This was interpreted as a Doppler shift and therefore the nebulae were receding from the earth, although without a direct measure for the physical size of these objects it was not realised that they were actually at extragalactic distances. In 1929 Edwin Hubble noted that Cepheid variable stars, an astronomical standard candle, in spiral nebulae were up to 10 magnitudes fainter than their counterparts in the field. From this he concluded that the nebulae were in fact individual galaxies separate from our own, described by some as 'island universes'. Hubble's law is the relation between the redshift and luminosity of a galaxy. He found that the speed of galaxy recession was proportional to its distance from Earth. This is summarised in the equation $v = H_0 r$ where v is the velocity, r is the distance and H_0 is the Hubble

constant.

The major theoretical contribution to 20th century cosmology was Albert Einstein's general theory of relativity published in 1915. This was an extension of his previous work on the special relativity of moving objects to include gravity. By applying general relativity to cosmology Alexander Friedmann was able to demonstrate that the Universe could either expand or contract. The equations that describe this behaviour are known as the Friedmann-Lemaitre-Robertson-Walker (FLRW) equations as they were independently derived by a number of researchers. In 1927 Georges Lemaitre, of the FLRW equations, proposed that the Universe was expanding from an explosion of a 'primeval atom'. This would later be known as the Big Bang theory.

Hubble's law was used as evidence to prove Lemaitre's Big Bang theory. That is to say if all galaxies are receding from each other, then at some time in the past all matter in the Universe must have been in a hot dense state. An alternative theory was given by Fred Hoyle who preferred the steady state model of the Universe. In this model the Universe remained in perpetual steady state as new matter formed in the space between the receding galaxies.

Although these competing theories had equal stature for a time, evidence began to emerge that gave overwhelming support to the Hot Big Bang. One major piece of evidence came in 1965 when Arno Penzias and Robert Woodrow Wilson discovered the cosmic microwave background radiation (CMB). The CMB is radiation with a near perfect thermal black body spectrum across the whole sky with a characteristic temperature of 2.7K. This radiation is a redshifted, and therefore cooled, remnant from a time when the Universe was in a causally connected hot dense state in line with the Big Bang theory. The CMB is radiation from the epoch of recombination, the period roughly 400,000 years after the Big Bang, when the Universe had cooled to a temperature where electrons could combine with protons to form atoms. Therefore at recombination matter decoupled from radiation and the Universe finally became transparent to photons, the CMB is redshifted light from this surface of last scattering.

1.2.1 Dark Matter and Dark Energy

Our 21st century understanding of the nature of the Universe, 'Lambda Cold Dark Matter' (ΛCDM), has a significant 'Dark' component. We now discuss the concepts of Dark Matter and Dark Energy and the evidence that points to their existence.

Dark Matter is thought to be a non-baryonic form of matter that does not interact via the electromagnetic force. As such it is incredibly difficult to detect directly. However, there appears to be a extremely large amount of 'missing mass' in the Universe which can be explained by invoking Dark Matter.

Fritz Zwicky was the first astronomer to notice the effects of Dark Matter. In 1933 he estimated the mass of the nearby Coma Cluster of galaxies from the motion of its outer members. Zwicky found more than a 2 orders of magnitude discrepancy between this dynamical mass and that which he calculated from the luminosities of the cluster members. From this he concluded that there must be some missing invisible mass. Even with cluster mass values calculated from X-ray observations and gravitational lensing techniques, modern astronomers find typical cluster mass to light ratios well in excess of 100 to 1.

Further evidence for Dark Matter came in the 1970s with radio observations of the 21cm emission from neutral hydrogen and the advent of sensitive optical spectrometers. It was then possible to accurately study the rotation speed of edge-on spiral galaxies. Plotting rotation velocity vs distance from the centre of the spiral galaxy gave a surprising result. Stars and gas orbiting galaxies at large radii, where the density of observable mass is low, appear to have the same velocity as those closer to the massive central bulge of the galaxy. Indeed the velocity curve was found to be essentially flat out to large radii. This implies uniform mass density out to large radii where the galaxy appeared to have a much lower density of stars. The missing mass was the Dark Matter Zwicky had inferred 40 years earlier. Within a few years this elusive mass was also found to be present in elliptical galaxies when studying their velocity dispersions, although this is still disputed (e.g. Romanowsky et al. 2003).

More recent evidence for Dark Matter comes from large scale structure studies from both observations and simulations. Dark Matter is found to be required in a Universe

where objects form hierarchically, with small objects forming first and merging to form larger structure. After the Big Bang baryonic matter was still too energetic to overcome its own pressure and collapse into the first small structures. However, the structure we observe in CMB anisotropies and in large scale surveys suggest that objects did form more rapidly than that expected by baryonic matter. Therefore a form of cold matter, that only interacts significantly with itself and ordinary matter through gravity, is required to form structure in the early Universe.

The effects of Dark Matter in galaxy clusters has now been studied directly and independently of the cluster X-ray gas in observations of the 'Bullet Cluster' (1E 0657-56, Markevitch et al. 2004, Clowe et al. 2006). The Bullet Cluster is a high-velocity cluster merger taking place in the plane of the sky. The galaxies of the two sub-clusters, being essentially collisionless, have passed through each other leaving behind their hot gas components. This gas can easily be observed at X-ray wavelengths as being separate from the optical observations of the two main galaxy populations. When a gravitational lensing analysis is performed on the entire structure, the majority of the mass is found to be associated with the regions containing the galaxies and not where the gas is located (Fig. 1.1). As X-ray and mass to light ratio studies find the gas in clusters to be more massive than the galaxies, a modified version of gravity would still find the mass peak in the high density gas region. This observation is therefore very difficult to explain without invoking collisionless Dark Matter.

In addition to Dark Matter the ΛCDM paradigm also includes Dark Energy (Λ). This is a form of energy that is thought to permeate the entire Universe. Its effect is to apply a negative pressure that increases the rate of expansion of the Universe. Like Dark Matter, the nature of Dark Energy does not lend itself to direct detection. However, its effects were first noted when astronomers studied distant supernova which could be calibrated as 'standard candles' and found them to be fainter than expected within the cosmology of the time indicating an increase in the rate of Universal expansion (Perlmutter et al., 1998; Riess et al., 1998).

Dark Energy may be in one of two forms, a cosmological constant or quintessence. A cosmological constant describes a homogeneous constant energy density permeating all space. The alternative, quintessence, is a dynamic energy field which varies in

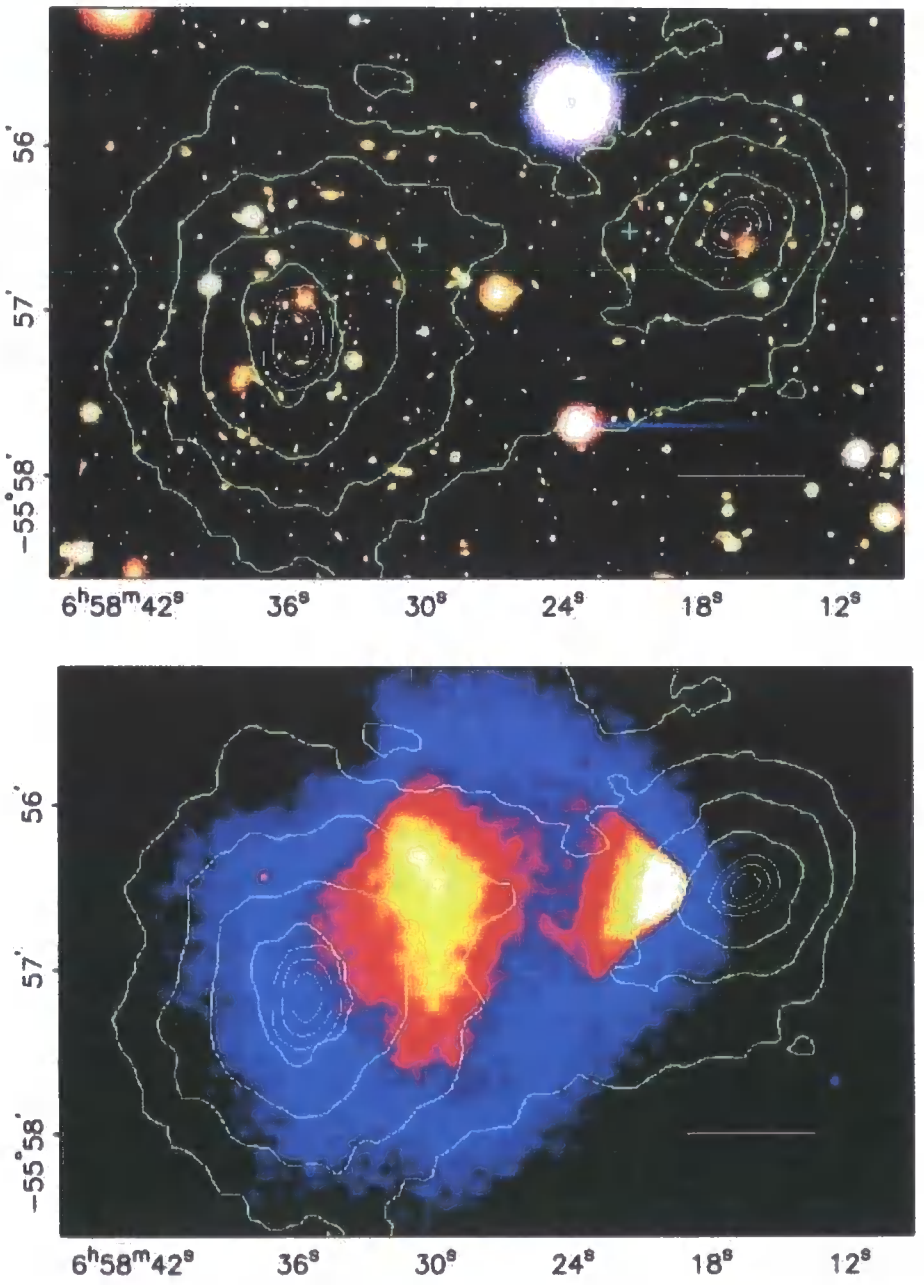

Figure 1.1: *Upper panel*: Optical image of the Bullet Cluster with the weak lensing mass map contours over plotted. The crosses indicate the centres of the X-ray emission and therefore the location of the peak in the hot gas component. *Lower panel*: X-ray emission from the Bullet Cluster indicating the location of the hot gas component. Again the mass contours are over plotted (Clowe et al., 2006)

space and time. Dark Energy's form is parameterised by $w = P/\rho$ where P the is negative pressure exerted by Dark Energy and ρ is its energy density. If w=-1 we have the cosmological constant, if w <-1/3 which can also vary with space and time we have quintessence. It will be possible to distinguish between these two forms with high precision measurements of how the expansion of the Universe evolves with time.

The density parameter of the Universe, Ω, is the ratio of the observed density to the critical density ($\Omega = \rho/\rho_c$). The critical density is the mean density of matter required for gravity to halt the expansion of the Universe. The density of the different components of the Universe are measured relative to Ω. The results of the Wilkinson Microwave Anisotropy Probe (WMAP) observations of anisotropies and structure in the CMB provide the relative quantities of ordinary matter, Dark Matter and Dark Energy in the Universe and excellent constraints on other important cosmological parameters (Spergel et al. 2003, 2007). The results demonstrate that the Universe is composed of 4% ordinary baryonic matter, 22% Dark Matter and 74% Dark Energy. That is to say Ω_b=0.04, Ω_{dm}=0.22 and Ω_Λ=0.74 for a flat Universe where the critical density Ω=1. The Hubble constant is found to be 70 $^{+2.4}_{-3.2}$ km s^{-1} Mpc^{-1} with the Universe being 13.7 $\pm 0.2 \times 10^9$ years old and possessing a geometry that is consistent with being flat (Spergel et al., 2007). The basic components of the ΛCDM Universe are represented in Fig. 1.2.

Alternatives to Dark Matter/Energy have been proposed which involve the modification of Newtonian gravitation and General Relativity. However, such models are unable to simultaneously reproduce the observational results on Solar System, Galaxy, Cluster and Universe scales.

1.3 Galaxies

In addition to his work on the redshift luminosity relation that bears his name, Edwin Hubble set about classifying galaxies based on their morphology. He classified galaxies as elliptical, lenticular, spiral, barred spiral or irregular. The Hubble Sequence of galaxies is displayed in the classic 'tuning fork' diagram in Fig. 1.3.

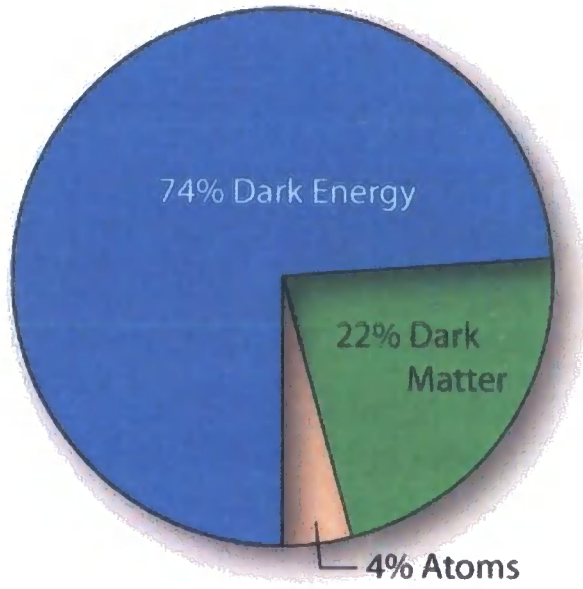

Figure 1.2: A pie chart displaying the constituents of the Universe according to the WMAP result (Spergel et al. 2003, 2007).

The 'tuning fork' diagram begins on the left with elliptical galaxies. These galaxies are elliptical in shape and are composed of old, evolved population II stars. They appear to have no significant gas, dust or recent star formation and are as such often referred to as early type or passive galaxies. Elliptical galaxies are classified from E0-E7 depending on their eccentricity, E0 being spherical and E7 having an eccentricity of 0.7.

Beyond the E7 ellipticals the tuning fork splits into spirals (S) and barred spirals (SB). However, before this split are the lenticular galaxies (S0 or SB0). These galaxies have a central bulge of old stars and a younger disk but no spiral arm structure. The top fork contains the spirals galaxies. These are galaxies with a central spheroidal bulge containing old population II stars. Around this bulge is a disk containing star forming spiral arms. The arms and disk are host to a significant amount of young population I stars, gas and dust. The lower case letter following the S denotes how tightly wound the arms are. They range from 'a' to 'd' with 'a' being the most tightly wound. A barred spiral (SB) in the lower fork is also spiral in appearance but the spiral arms protrude from a bar structure in the central bulge.

Again, the lower case letter following the SB denotes the winding of the arms.
A class of galaxies not shown on the classic Hubble tuning fork is the irregular galaxies. Galaxies of this type are generally star forming with either an irregular spiral (Irr-I) or an irregular structure with no obvious classification (Irr-II).
It is important to note that although Hubble classification diagram was originally used to represent the evolution of galaxies, this is no longer the case. It is now purely a representation of the morphologies of galaxies in the Universe.

1.4 Galaxy Clusters

A galaxy cluster is a collection of gravitationally bound galaxies, with a comparable but greater mass in hot X-ray emitting gas. These observable components are contained in a massive Dark Matter halo. Galaxy clusters appear prominent in optical and near-infrared images as they are dominated in this region of the spectrum by large passive elliptical galaxies. Large galaxy clusters contain 1000's of galaxies within a region several Mpc across and can have total masses in excess of $10^{15}M_{\odot}$. Local examples of clusters are the Virgo Cluster and the Coma Cluster. Fig. 1.4 is a false colour image of the Abell 1703 cluster.
In the mid 20th century George Abell compiled a comprehensive catalogue of rich galaxy clusters in the local Universe. His catalogue contains over 4000 clusters covering the entire sky. The northern and equatorial part of this catalogue was completed during his time as a PhD student at the Palomar observatory (Abell, 1958). This was followed by his posthumously published southern catalogue (Abell et al., 1989). Fritz Zwicky also compiled his own larger catalogue of clusters (Zwicky & Kowal, 1968).
Galaxy cluster observations can be undertaken across the electromagnetic spectrum. Optical and near infrared wavelengths are used to observe the galaxy population. This is extended to the mid-infrared for high redshift clusters. The intracluster medium (ICM) of hot plasma emits both high energy bremsstrahlung and atomic line emission. This extended emission is observed at X-ray wavelengths. Clusters are also seen to emit in the radio from AGN and the 21cm line from diffuse HI

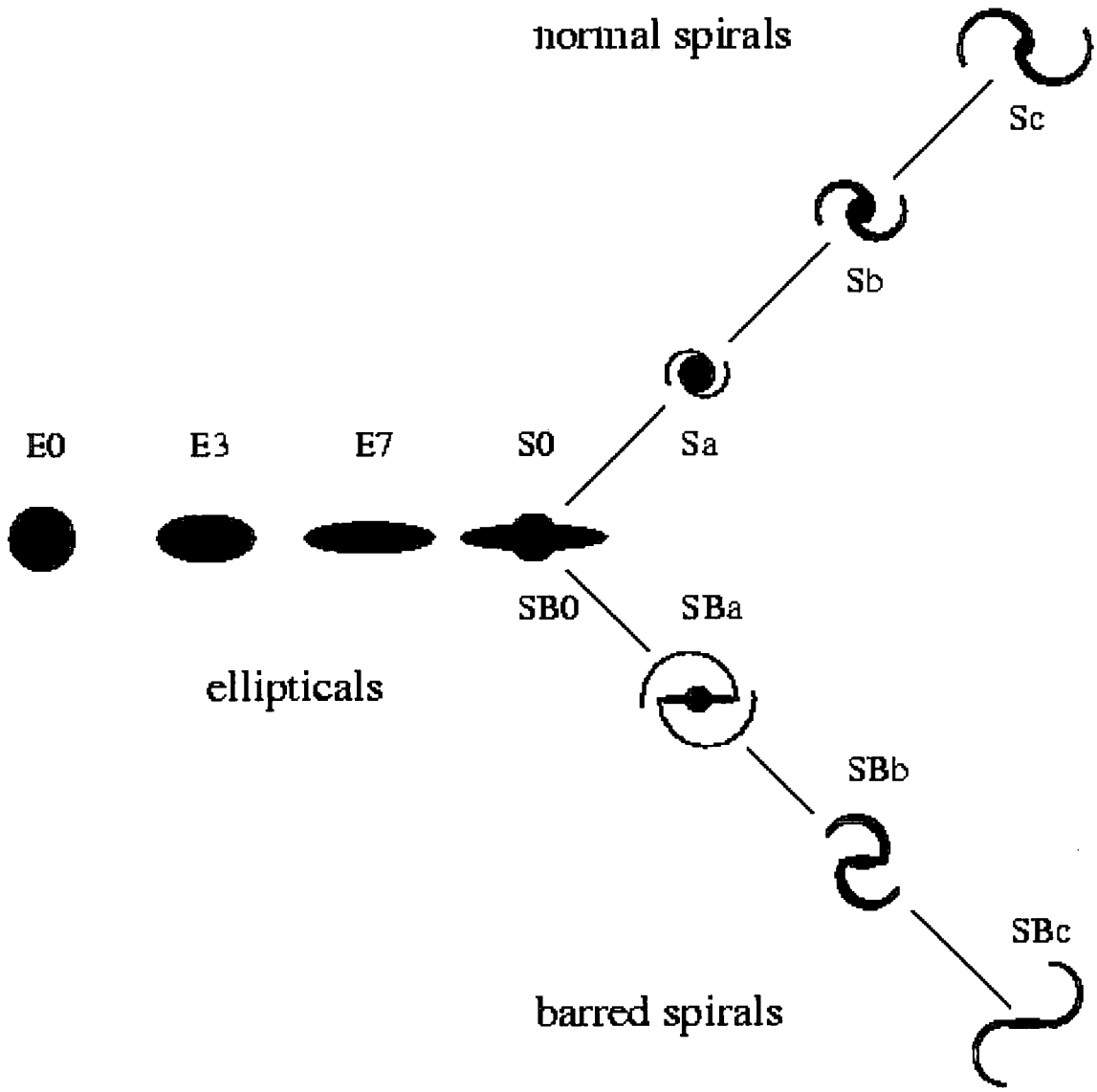

Figure 1.3: The Hubble Sequence 'tuning fork' diagram explaining the classification of galaxies (source: http://www.astro.caltech.edu/ aam/).

Figure 1.4: Optical image of the galaxy cluster Abell 1703 (source: RGB image created from *Hubble Space Telescope* archival images).

regions. It is also possible to study clusters by measuring their effect on the CMB. The Sunyaev-Zel'dovich effect is the distortion of the CMB due to inverse Compton scattering of CMB photons by the ICM.

Galaxy clusters being very massive can be used as 'gravitational telescopes' to view objects in the early Universe as they bend and amplify the light from distant background objects through gravitational lensing. Gravitational lensing is predicted by Einstein's theory of General Relativity and acts in a similar way to lensing by a magnifying glass, only the light is bent by the mass of the galaxy cluster rather than refraction. This lensing creates arcs and other distorted images of the background galaxies (see Fig. 1.4 for examples). We can therefore perform analyses on the lensed objects (morphologies, photometry and spectroscopy). By fitting models to the observed distortions of background galaxies a total mass and a mass map of the galaxy cluster can be made. Gravitational lensing is divided into two regimes, strong and weak. Strong lensing describes the distortions such as arcs and multiple images that occur in the region of the cluster's critical curve (the locus of maximum magnification). Weak lensing refers to distortions that are only detected through statistical analysis of a large number of background galaxies. Both strong and weak lensing analysis are important for Dark Matter studies and are key to the Bullet Cluster study discussed in §1.2.1.

We are now in an era where it is possible to use clusters to perform tests on our understanding of cosmology. Surveys such as UKIRT Infrared Deep Sky Survey (UKIDSS, Lawrence et al. 2006), the Panoramic Survey Telescope and Rapid Response System (Pan-STARRS) and the Deep Extragalactic Evolutionary Probe 2 (DEEP2, Davis et al. 2005) will probe the abundance of galaxy clusters at high redshifts. This abundance depends on $\sigma_8(\Omega_m)^{0.5}$, where σ_8 is the rms mass fluctuation amplitude in spheres of size $8h^{-1}$ Mpc and Ω_m is the total density in matter. The degeneracy between these two parameters can be broken by measuring the evolution of the abundance of clusters. This is a sensitive measure of Ω_m even if measurements extend only to moderate redshift, z=0.5. The best current measurements from X-ray surveys agree within errors to those of WMAP yielding Ω_m=0.35±0.10 (Borgani et al., 2001). The differences between cosmologies are greatest for the most

massive clusters and the highest redshifts. Beyond redshift z=0.6 the test can start to distinguish between cosmologies of the same Ω_m, but different Λ, and beyond z=1 it is theoretically possible to place constraints on the Dark Energy equation of state parameter $w = P/\rho$ (Haiman et al., 2001).

1.5 This work

Galaxy clusters are extremely important laboratories for the study of galaxy formation and evolution as they contain a concentrated population of many galaxies in a relatively small volume. Early workers in the field found that when a colour-magnitude diagram was plotted for members of local clusters such as Virgo and Coma, the Elliptical/S0 galaxies were found to be confined to a prominent linear feature in colour space (Visvanathan & Sandage, 1977). This feature is known as the red sequence and be easily seen in the colour-magnitude diagram for the cluster Abell 1703 (Fig. 1.5). The red sequence has a very small intrinsic scatter (typically <0.1 mag) and has been interpreted as evidence that the passive galaxies in clusters formed coevally at high redshift (Bower et al., 1992).

In this thesis we present the results of our investigations into galaxy cluster evolution. We achieve this with analysis of deep optical and near-infrared observations of $\sim$ 150 rich galaxy clusters in the redshift range $0< z <1$. For this work we have selected the most X-ray luminous clusters known. These clusters correspond to the most extreme high mass, high density environments at their respective epochs. This homogeneity is key to our study as we wish to compare clusters over a range of redshifts.

We begin in Chapter 2 at the bright end tip of the red sequence by investigating the evolution of the brightest cluster galaxy (BCG). The BCG is normally found near the centre of cluster's mass and X-ray gas emission. This is, by definition, the brightest elliptical galaxy in the cluster. The BCG in the Abell 1703 cluster can easily be identified near the centre of Fig. 1.4. BCGs are the most luminous and homogeneous population of non-active galaxies in the Universe. Because of this we can use them to study the evolution of cluster elliptical galaxies across half the age of the Universe. One important test of galaxy formation is to use BCGs to distinguish

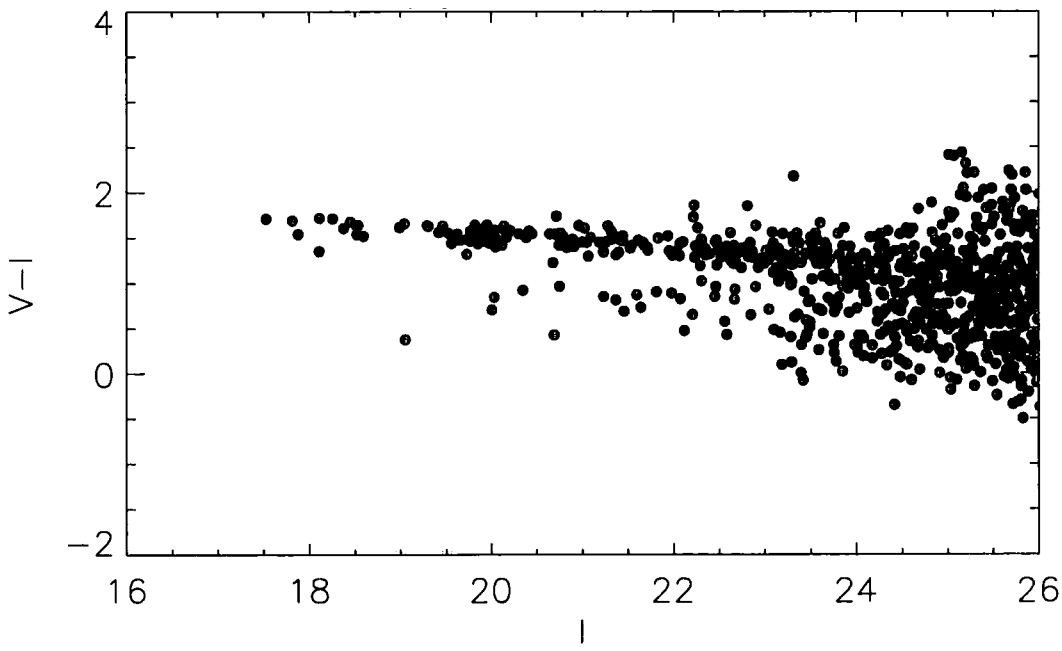

Figure 1.5: A V-I vs I Colour-magnitude diagram for the cluster Abell 1703.

between monolithic collapse and hierarchical merger models. The former describes a situation where a galaxy forms at high redshift from collapsing material which results in a short burst of intense star formation. Hierarchical merging is now the favoured model as it is predicted by modern computer simulations of the Universe. In this situation the galaxies are built up through mergers of smaller systems.

Moving down in luminosity from the BCG, the red sequence itself has a number of observable parameters that can be used to constrain the evolution of cluster member galaxies. In Chapter 3 we observe the build up of this sequence over time. This is achieved by studying the evolution of the relative numbers of giant and dwarf galaxies along the red sequence since z=1. The observation of this build up is an important step on the way to understanding how dwarf cluster ellipticals are formed and if this is related to other cluster observations such as the increase in blue galaxy fraction with redshift (Butcher & Oemler, 1984) through transformation processes.

A further galaxy cluster observable shown to evolve with redshift is the slope of the red sequence in colour-magnitude space. In Chapter 4 we compare this observed evolution in both near-infrared and optical bands to semi-analytic models based on the Millennium N-body simulation (Springel et al., 2005). Such work is an excellent test of the mass-metallicity relation in simulations and is applicable to red sequence cluster selection processes such as the ones employed in chapter 6.

In chapter 5 we move on to discussing the UKIDSS Deep eXtragalactic Survey (DXS, Survey Head: Alastair Edge). This is the 2nd deepest part of the ongoing UKIDSS northern sky near-infrared survey. We outline this survey and include our initial data processing and analysis of the early data releases.

Robust methods of cluster selection are required in the era of large area cluster surveys to probe cosmology. In Chapter 6 we discuss a method of cluster selection in the UKIDSS DXS fields utilising a red sequence finding algorithm on near-infrared and optical catalogues. The photometric results are then tested with spectroscopic analysis of the candidate clusters. The clusters selected here, although not X-ray selected, feed back into the high redshift regime of our other studies.

Lambda Cold Dark Matter (ΛCDM) cosmology (Ω_M =0.3, Ω_{Vac} =0.7, H_0 =70 km s^{-1} Mpc^{-1}) is used throughout this work.

1.6 Papers related to this work

Several of the chapters in this thesis are based papers that are either published, submitted or in preparation. A list of chapters and their corresponding papers is provided below.

- Chapter 2: Near-infrared evolution of brightest cluster galaxies in the most X-ray luminous clusters since z=1

  J. P. Stott, A. C. Edge, G. P. Smith, A. M. Swinbank, H. Ebeling. *MNRAS submitted*

- Chapter 3: An increase in the faint red galaxy population in massive cluster s since z$\sim$0.5.

  J. P. Stott, I. Smail, A. C. Edge, H. Ebeling, G. P. Smith, J. -P. Kneib, K. A. Pimbblet. *ApJ, 661, 95, astro-ph/0703484*

- Chapter 4: Evolution of the cluster red sequence slope since z$\sim$1.

  J. P. Stott, K. A. Pimbblet, A. C. Edge, J. L. Wardlow. *MNRAS in preparation*

- Chapter 6: The discovery of a massive supercluster at z=0.90 in the UKIDSS DXS.

  A. M. Swinbank, A. C. Edge, I. Smail, **J. P. Stott**, UKIDSS DXS Working Group. *MNRAS, 379, 1343*

Chapter 2

The evolution of brightest cluster galaxies since z =1

Overview

We begin this thesis at the bright end of the red sequence with an investigation into the nature of the evolution of brightest cluster galaxies (BCGs) from a sample of rich galaxy clusters. By employing an X-ray selection of $L_X > 10^{44}$erg s^{-1} we limit environmental effects by selecting BCGs in comparably high density regions. We find a positive relationship between X-ray and near-infrared luminosity for BCGs in clusters with $L_X > 5 \times 10^{44}$erg s^{-1}. Applying a correction for this relation we reduce the scatter in the BCG absolute magnitude by a factor 30% and confirm that the evolution of these galaxies is passive. The near-infrared $J-K$ colour evolution demonstrates that the stellar population in BCGs has been in place since at least z =2 and that we expect a shorter period of star formation than that predicted by current hierarchical merger models. We also confirm that there is a relationship between 'blue' $J-K$ colour and the presence of BCG emission lines associated with star formation in cooling flows.

2.1 Introduction

A Brightest Cluster Galaxy (BCG) is a giant elliptical galaxy near the spatial and gravitational centre of a galaxy cluster. BCGs are the brightest and most massive stellar systems in the Universe. Their high luminosities and small scatter in absolute magnitude makes them effective standard candles. As such they were originally used by astronomers to confirm and considerably increase the range of Hubble's redshift - distance law (e.g Sandage 1972). BCGs are particularly important for galaxy formation and evolution studies as the above properties make them less prone to selection effects and biasing. Near-infrared photometry is often chosen for BCG studies as K correction, stellar evolution and extinction by dust in this region of the spectrum are considerably less than at optical wavelengths.

There is considerable observational evidence that suggests giant ellipticals were formed at high redshift and have been passively evolving to the present day (Aragon-Salamanca et al., 1993; Bower et al., 1992; Stanford et al., 1998; van Dokkum et al., 1998). Passive evolution describes a situation where the stellar population in a galaxy forms in a single burst at a redshift z_f. This population then matures, without further star formation. No evolution describes the case where the observed luminosity changes over cosmic time of a stellar population are purely attributed to the effects of distance and K correction. Depending on the cluster selection technique the BCG photometry can follow drastically different evolutionary tracks. For example highly luminous X-ray clusters tend to prefer evolving models whereas low L_X clusters are seen to have stellar populations preferring no evolution (Aragon-Salamanca et al. 1998, Burke et al. 2000 and Nelson et al. 2002).

The latest hierarchical simulations of BCG formation predict that the stellar components of BCGs are formed very early (50 per cent at $z \sim 5$ and 80 per cent at $z \sim 3$, De Lucia & Blaizot 2007). This star formation occurs in separate sub-components which then accrete to form the BCG through 'dry' mergers. It is important to note that in these simulations local BCGs are not directly descended from high-z ($z > 0.7$) BCGs. However, De Lucia & Blaizot (2007) find little physical difference between the progenitors of local BCGs and high-z BCGs or between the local BCGs and the descendants of the high-z BCGs. This means that observed evolution

presented here can still be compared to the simulation.

In this chapter we aim to test the above results and provide further constraints to simulations by comparing the K band and $J-K$ colour evolution of a well defined X-ray selected sample of BCGs to a set of evolution models.

We study a large sample of the most X-ray luminous clusters known which correspond to the most extreme environments at their respective epochs. The motivation for studying an X-ray selected sample of clusters is to ensure that we are observing objects in similar high mass, high density environments. This homogeneity is key to our study as we wish to compare clusters over a range of redshifts. By incorporating clusters from the MAssive Cluster Survey (MACS, Ebeling et al. 2001) we are going to higher X-ray luminosity than any previous BCG study.

Lambda CDM cosmology (Ω_M =0.3, Ω_{Vac} =0.7, H_0 =70) and the Vega magnitude system are used throughout.

2.2 Data

2.2.1 The sample

To select BCGs in a homogeneous sample of massive clusters from z =0 – 1 we require X-ray selected clusters from a number of large surveys. These clusters are all selected to have X-ray luminosities in excess of 10^{44}erg s^{-1} (0.1 – 2.4 keV) and therefore correspond to the most massive clusters known. The z <0.3 sample are taken from the *ROentgen SATellite* (*ROSAT*) Brightest Cluster Survey (BCS), extended BCS (Ebeling et al., 1998) and the X-ray Brightest Abell Clusters Survey (XBACS, Ebeling et al. 1996). We then select a comparable sample at $0.3 < z < 0.7$ from the MAssive Cluster Survey (MACS, Ebeling et al. 2001). Additional high redshift clusters are sourced from analysis of archival observations of the clusters MS1054-0321 and RCS0224-0002. Details of the sample can be found in tables 2.1, 2.2 and 2.3.

Our sample also contains additional BCGs from spectroscopically confirmed high redshift optical-infrared selected clusters discovered in Swinbank et al. (2007) (see also chapter 6). These BCGs where found in the UKIRT Infrared Deep Sky Survey

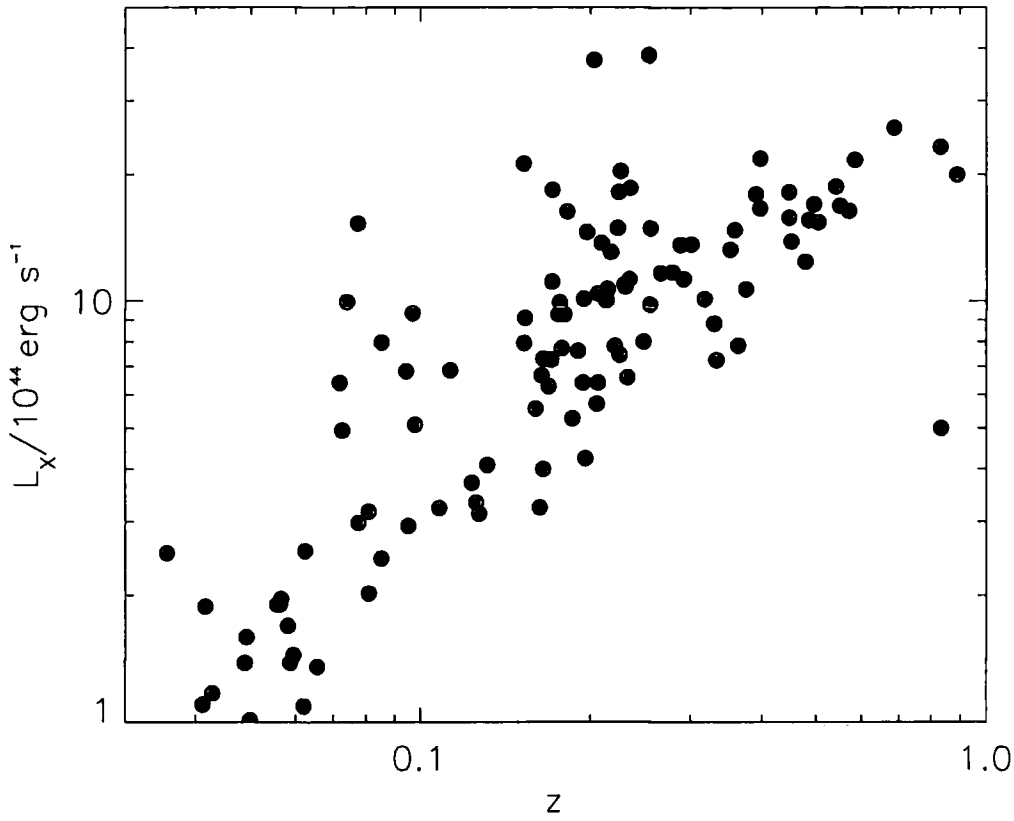

Figure 2.1: The X-ray luminosity vs z for our sample.

(UKIDSS, Lawrence et al. 2006) Deep eXtragalactic Survey (DXS, Survey Head: Alastair Edge). They are not yet confirmed as high L_X clusters but they do have absolute magnitudes comparable with the rest of our sample (mean absolute magnitude of DXS BCGs is -26.6).

Fig. 2.1 shows the X-ray luminosity vs redshift for our sample which demonstrates that we are going to higher X-ray luminosity than any previous BCG study as we have excellent coverage in the $L_X > 10^{45}$erg s^{-1} range. In total we have a sample of 121 BCGs available for analysis of which 47 are in the $L_X > 10^{45}$erg s^{-1} regime compared to only 7 from the Burke et al. (2000) sample.

2.2.2 Photometry

To study a sample of BCGs spanning such a wide redshift range we obtain data from several sources.

A combination of the Two Micron All Sky Survey (2MASS) extended and point source catalogues (Skrutskie et al., 2006) is used for the z ~0.03 – 0.15 BCS, eBCS and XBACS BCGs. The limiting magnitudes for the XSC are J =15.1, and K_s =13.5 mag. The eXtended Source Catalogue (XSC) K20 fiducial elliptical total magnitudes are used throughout incorporating the same aperture size in both J and K bands which is crucial to ensure precise colour photometry.

The z ~0.15 – 0.3 BCS, eBCS and XBACS observations were performed in 2004 and 2005 in variable seeing (0.9" – 1.5") with the Wide field InfraRed Camera (WIRC, Wilson et al. 2003) instrument on the Palomar 200" Hale telescope (P.I: G. P. Smith). These observations were performed as a poor seeing back up for a campaign to image MACS clusters. These data were reduced with the WIRCTASK IRAF scripts.

The $z \sim 0.3 - 0.7$ MACS data are from 3 separate observing campaigns. Part of these data were obtained in 2002 in 0.4" – 0.7" seeing using the UKIRT Fast-Track Imager (UFTI) camera on the United Kingdom InfraRed Telescope (UKIRT). The data were reduced using the ORAC-DR pipeline. More MACS were observed in ~1.0" seeing in 2002 again with the WIRC instrument on the Palomar 200" Hale telescope (P.I: G. P. Smith). This was reduced with the WIRCTASK IRAF scripts. The remaining clusters were observed in 2004 (P.I: J.-P. Kneib) in ~0.6" seeing conditions using the Infrared Spectrometer And Array Camera (ISAAC) on the Very Large Telescope (VLT). These data were reduced with the ISAAC eclipse pipeline.

The high-z clusters MS1054-0321 and RCS0224-0002 are sourced from archival data. The MS1054-0321 data are from VLT/ISAAC observations obtained as part of the Faint InfraRed Extragalactic Survey (FIRES, Förster Schreiber et al. 2006) and the RCS0224-0002 cluster was observed using WIRC/Palomar (P.I: G. P. Smith).

We include additional high redshift photometry from the literature. Photometry for near-infrared selected $z \sim 0.9$ clusters is sourced from UKIDSS DXS data described in chapters 5 and 6 and Swinbank et al. (2007). The Wide Angle *ROSAT* Pointed Surveys (WARPS, Scharf et al. 1997, Jones et al. 1998) X-ray selected $z \sim 0.9$ photometry was sourced from data described in Ellis & Jones (2004).

The BCG photometry for all of our near-infrared data is extracted using SExtractor's 'Best' magnitude Bertin & Arnouts (1996). The centre of clusters can be very densely populated so for crowded objects the 'Best' magnitude uses the isophotal magnitude which excludes the light from close neighbours and is therefore more reliable than a fixed aperture. This choice of aperture is shown to be robust as we find no trend between ellipticity of the aperture/BCG and the absolute K band magnitude. The SExtractor photometry is run in dual mode with the K-band apertures used to extract the J-band photometry to ensure good colour determination. The photometry calibration for our data was achieved with a combination of 2MASS and/or standard star observations.

All magnitudes are corrected for Galactic extinction using Schlegel et al. (1998). The typical extinction values for our clusters were in the range 0.01 – 0.04 mag in K.

2.3 Analysis and Results

2.3.1 The BCG Degree of Dominance

We now look to see if differing cluster core environments effect our results. A measure of environment which can easily be extracted from photometric data is the degree of dominance. This parameterises the difference in luminosity between the BCG and the next brightest galaxies in the cluster. The BCG may be the dominant elliptical in a cluster centre containing much smaller galaxies or it may be in a system were it is only marginally brighter than the next brightest members. The degree of dominance is defined as $\Delta m_{1-2,3} = (m_2 + m_3)/2 - m_1$ where m_1 is the magnitude of the BCG and m_2 and m_3 are the magnitudes of the 2nd and 3rd brightest members respectively (Kim et al., 2002). The 2nd and 3rd brightest galaxies are selected as the next two brightest galaxies on the cluster red sequence within a radius of 500kpc of the BCG. Taking the average of the 2nd and 3rd ranked galaxies is slightly more robust to contamination than just using the 2nd. It also removes the weighting from cases where there are two BCG candidates that are far more luminous than the rest of the cluster. Fig. 2.2 shows a histogram of the distribution of the degree of K band

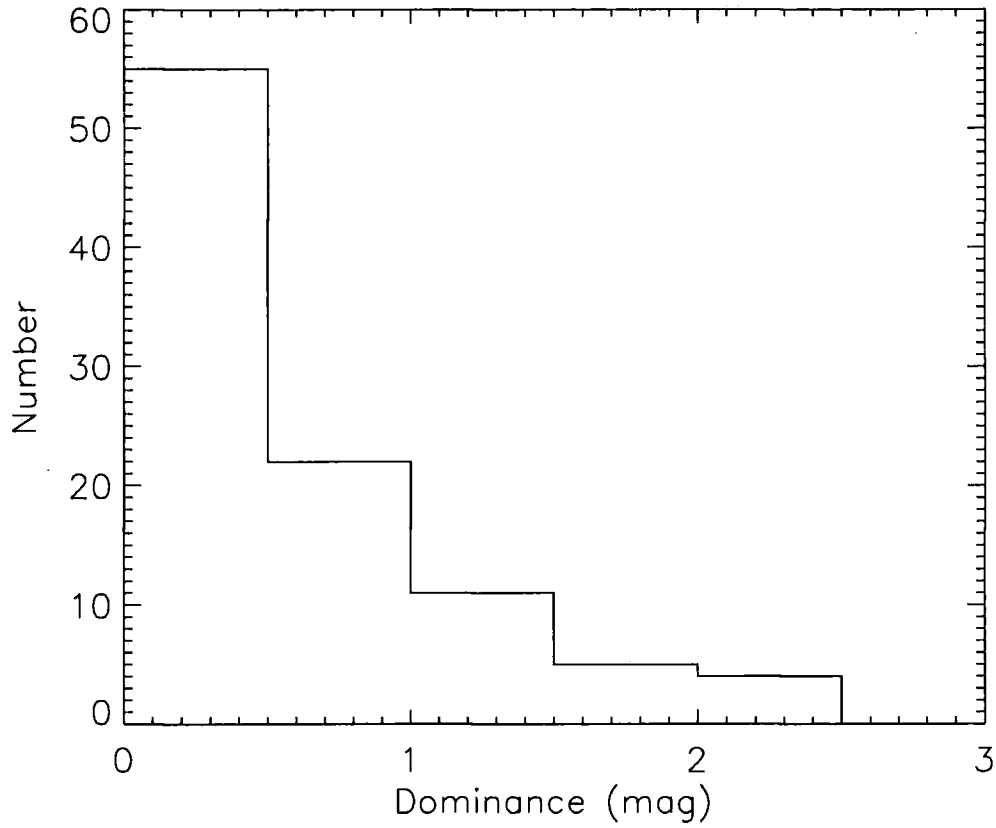

Figure 2.2: A histogram of the degree of BCG dominance for our sample.

dominance for our sample. The maximum cluster dominance found in our sample is 2.43 mag. We find that the majority of our BCGs are in cluster environments where they are not highly dominant. We plot dominance vs a number of other observables in Fig. 2.3. This plot shows that there is no obvious trend between dominance and redshift, X-ray luminosity or absolute K band magnitude. We are therefore satisfied that the differing galaxy environment between cluster cores has no effect on the results presented in this chapter.

2.3.2 K Band Correction

To observe whether BCGs from the most X-ray luminous clusters can be considered as 'standard candles' we present the absolute K band magnitude vs the X-ray luminosity (Fig. 2.4). The absolute K magnitude was calculated using K and passive evolution corrections from a Bruzual & Charlot (2003) SED with a simple stellar

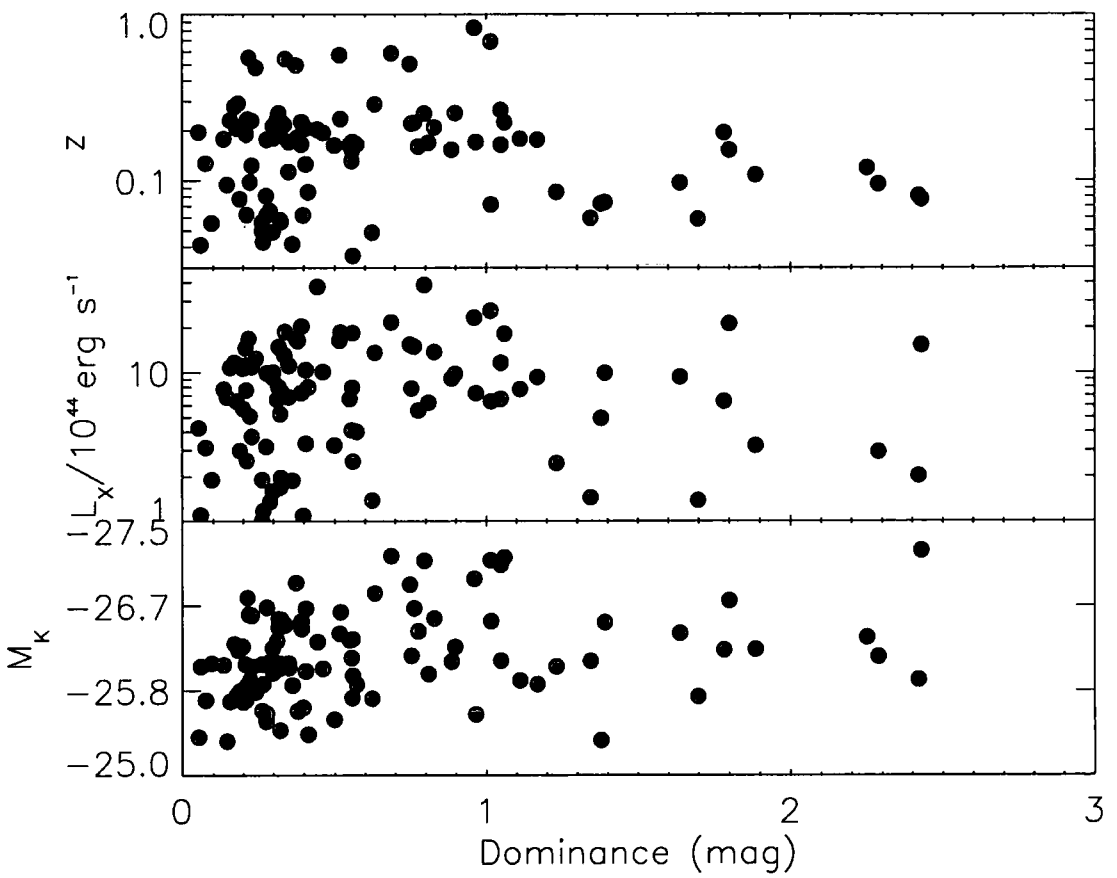

Figure 2.3: Redshift, X-ray luminosity and absolute K band magnitude vs BCG dominance.

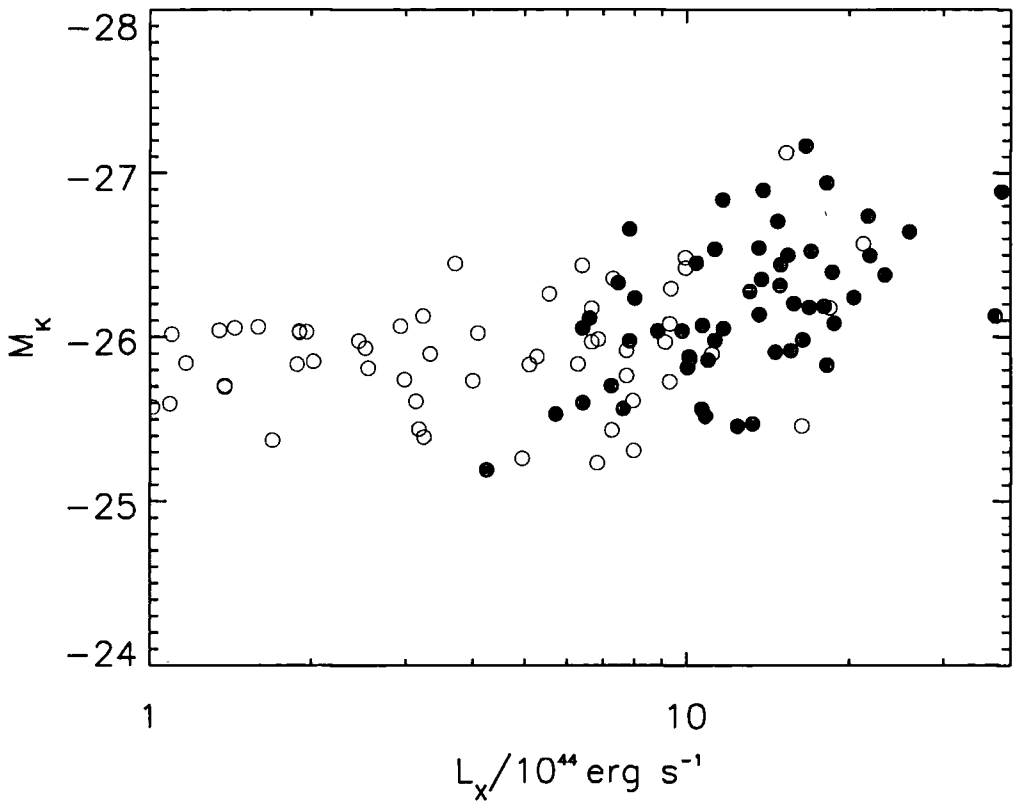

Figure 2.4: Absolute K band magnitude vs X-ray luminosity. The unfilled and filled points are BCGs below and above the median redshift of the sample (z=0.19) respectively.

population (SSP), z_f =5 and solar metallicity.

From Fig. 2.4 we find that there is no correlation between absolute magnitude and L_X below $L_X \sim 5 \times 10^{44}$erg s^{-1}, however beyond this value there appears to be a positive relationship. To demonstrate that this is not caused by redshift we highlight the BCGs above the median redshift (z=0.19) which indicates that the high and low z BCGs in the trend region are well mixed. We quantify the trend with a two parameter chi square minimised fit to the $L_X > 5 \times 10^{44}$erg s^{-1} BCGs. The gradient of this fit is found to be -1.1±0.3 mag per decade of L_X. We then use this fit to correct for the effect of L_X on the magnitude, shown in Fig 2.5. In Fig. 2.6 we plot the 1σ dispersion in the absolute magnitude versus z for both the corrected and uncorrected samples. From this we can see that the applied correction reduces

the scatter by a factor of ~30%.

The mean absolute K band magnitude for the L_X corrected cluster sample is -25.81 ± 0.35 compared to a mean M_K of -26.23 ± 0.45 mag for the uncorrected K band data. The mean magnitude of our sample is therefore comparable to the -26.40 ± 0.47 mag of Collins & Mann (1998). For comparison with simulation, De Lucia & Blaizot (2007) find their mean $M_K = -26.6 \pm 0.16$ mag which, although brighter, is within 1 sigma of our uncorrected mean. This demonstrates that the results from our findings can be compared to the observations of Collins & Mann (1998) and the simulations of De Lucia & Blaizot (2007).

Instead of a M_K correction with L_X we could assume that the trend in Fig. 2.4 is caused by redshift as our clusters are increasingly more X-ray luminous at higher z (Fig. 2.1). If we do ascribe the trend to redshift then we require $\gtrsim$2 mag of passive evolution to provide the same M_K correction as that with L_X (shown in Fig. 2.7). This magnitude of passive evolution at z =1 is not seen in stellar population models so we believe that our M_K – L_X trend is real and we concentrate on this for the remainder of the chapter.

2.3.3 Hubble Diagram

Now that we are satisfied that we have limited environmental effects within our sample we can test the nature of the BCG evolution. Figure 2.8 shows the uncorrected and X-ray luminosity corrected K band Hubble diagrams for the whole BCG sample respectively. The uncorrected Hubble diagram is included for comparison to demonstrate the success of the L_X – magnitude correction introduced in §2.3.2.

The lines plotted represent various stellar population models from the Bruzual & Charlot (2003) GALAXEV code. All models assume a Salpeter IMF (Salpeter, 1955) and solar metallicity (Humphrey & Buote, 2006). The models are normalised to the median BCG magnitude at $z \lesssim 0.1$. The formation redshifts of z_f =5, z_f =2 and a no evolution model are chosen for comparison with Burke et al. (2000).

By measuring the residuals about each model track in the corrected Hubble diagram we can identify which scenario best describes the data. Fig. 2.9 shows these residuals. We find that the passive evolution models provide a better description than

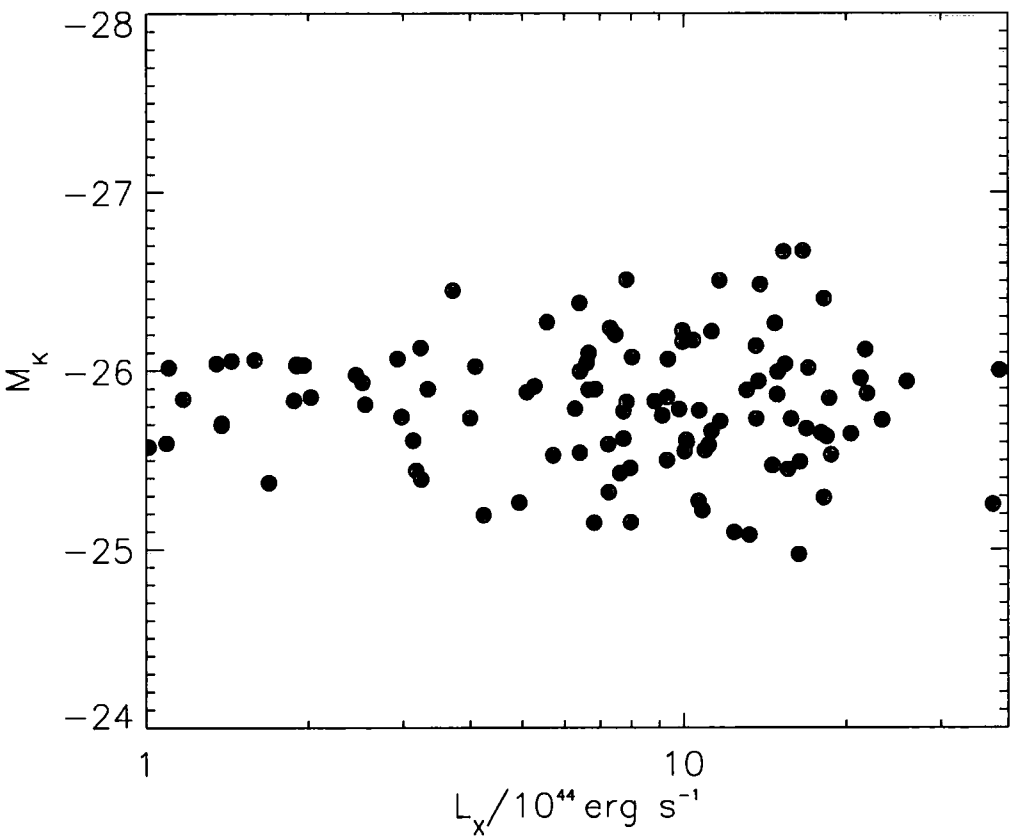

Figure 2.5: The corrected absolute K band magnitude vs X-ray luminosity.

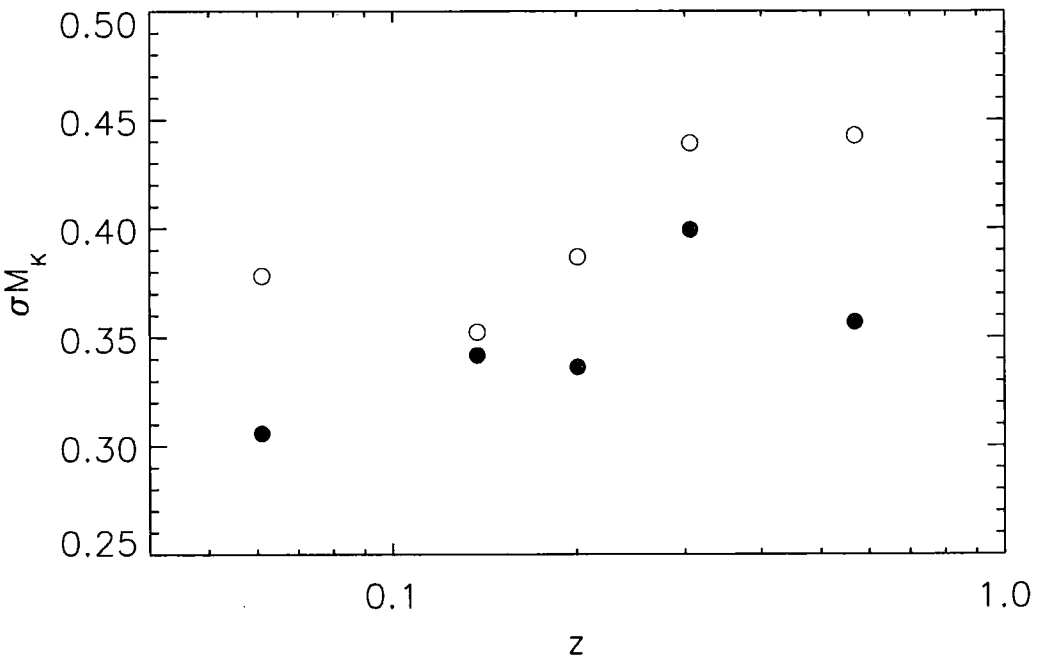

Figure 2.6: The 1σ dispersion in Absolute K band magnitude vs redshift. The filled/unfilled points are for the corrected/uncorrected M_K values.

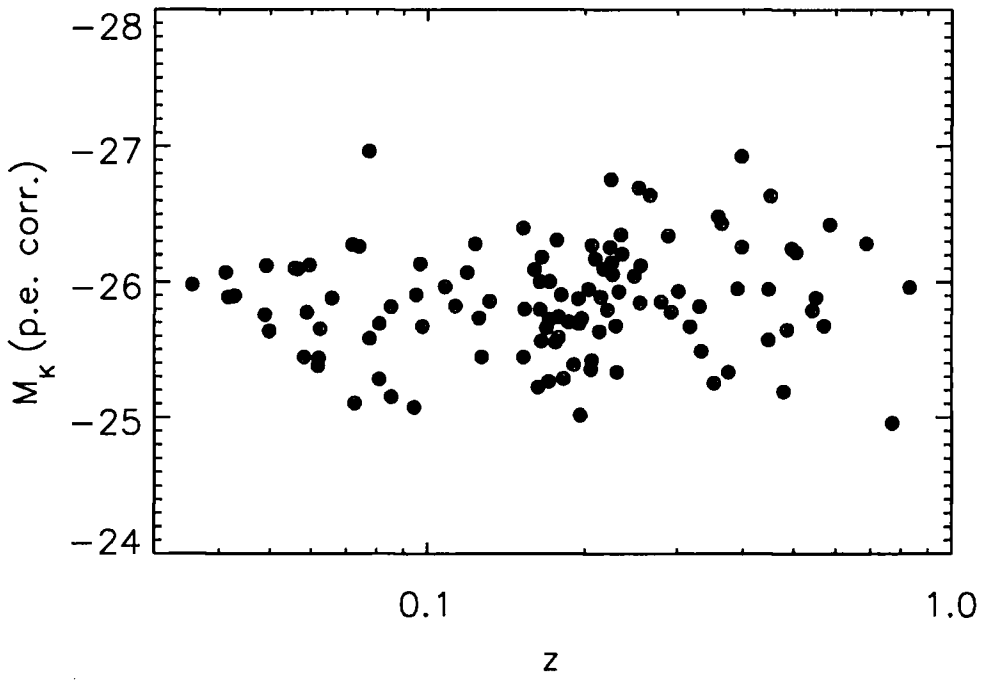

Figure 2.7: Absolute K band magnitude (corrected assuming passive evolution alone is responsible for the trend in Fig. 2.4) vs z. This magnitude of passive evolution ($\gtrsim$2 mag at z=1) is unrealistically large and not seen in stellar population models so we can rule this out as the cause of the observed trend in Fig. 2.4.

no evolution to a significance of 2.2σ. This is in agreement with the work of Burke et al. (2000) and De Lucia & Blaizot (2007).

As the significance of this result is low we look to further constrain the evolution of BCGs by investigating $J-K$ colour evolution with redshift in §2.3.4.

2.3.4 Colour Evolution with Redshift

Most BCG studies concentrate on the K band evolution with redshift but here we introduce the J band to observe the evolution of the $J-K$ colour. Fig. 2.10 is the $J-K$ colour vs z for our BCG sample. As in §2.3.3 the models we compare to are calculated using the Bruzual & Charlot (2003) GALAXEV codes. These models assume a Salpeter IMF and solar metallicity.

In addition, the dash dot line represents the model from De Lucia & Blaizot (2007). This model forms 50 per cent of the BCG stellar content by z ~5 and 80 per cent by z ~3. We calculate that this corresponds to an exponentially decreasing star formation rate with an e-folding time τ ~0.93Gyr. For consistency we calculate this photometric model using the same population synthesis as De Lucia & Blaizot (2007), a Bruzual & Charlot (2003) model with a Chabrier (2003) IMF.

The data show no real preference for a particular evolution track up to z ~0.4 as the models show little divergence up to this point. However, beyond this redshift the ISAAC, UKIDSS DXS and WARPS BCGs appear to favour the no evolution or passive z_f =5 models over z_f =2. We quantify this for the redshift range 0.8<z<1 by comparing the mean $J-K$ colour to the model values. We find a formation redshift z_f =2 is ruled out to a significance of 6σ while the z_f =5 and no evolution models are both within 3σ of the mean BCG colour. These results are in agreement with the observations of Burke et al. (2000) who favour $z_f > 5$. The De Lucia & Blaizot (2007) model is shown to be in good agreement with our observations at low z but becomes too blue compared to our current high z data, suggesting its star formation lasts for too long. We calculate that this model would provide a better description to our data if it had an exponentially decreasing star formation rate with e-folding time τ ~0.5Gyr.

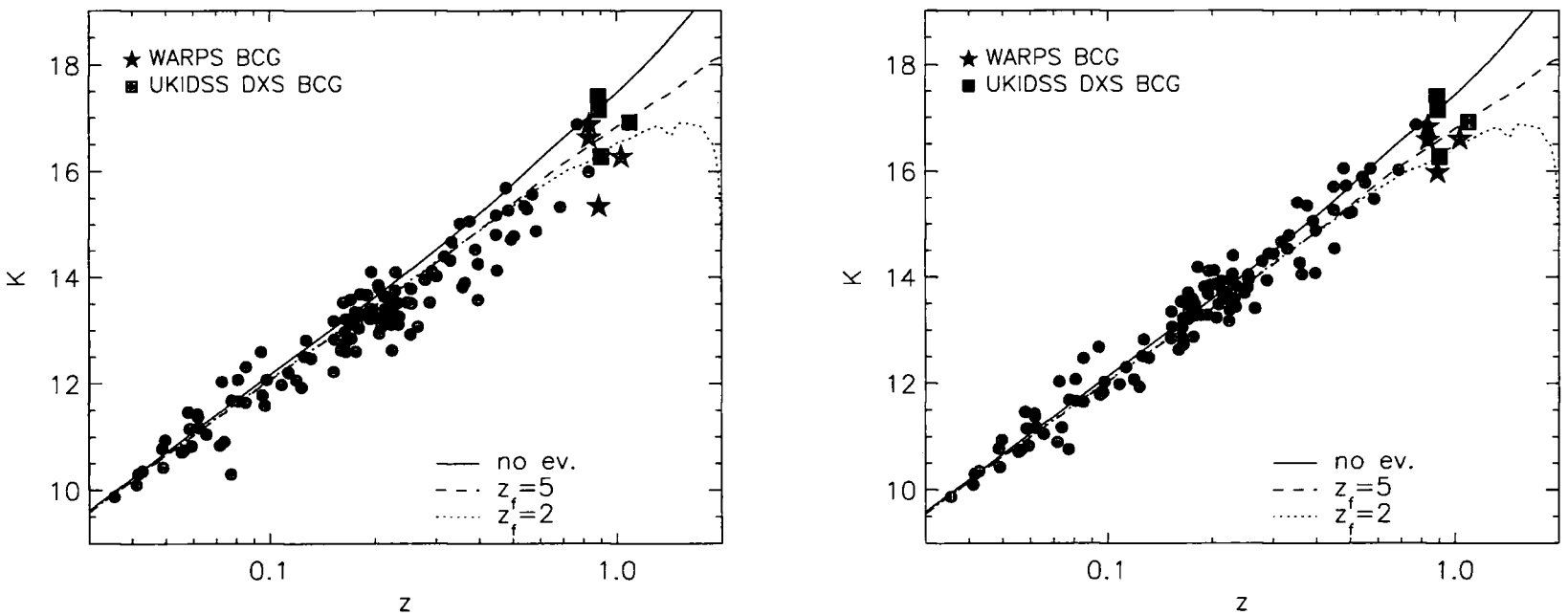

Figure 2.8: *Left*: K vs z Hubble diagram for the entire BCG sample. The lines represent different models from the Bruzual & Charlot (2003) GALAXEV codes. All models assume a Salpeter IMF and Solar metallicity. *Right*: The corrected K vs z Hubble diagram for the entire BCG sample.

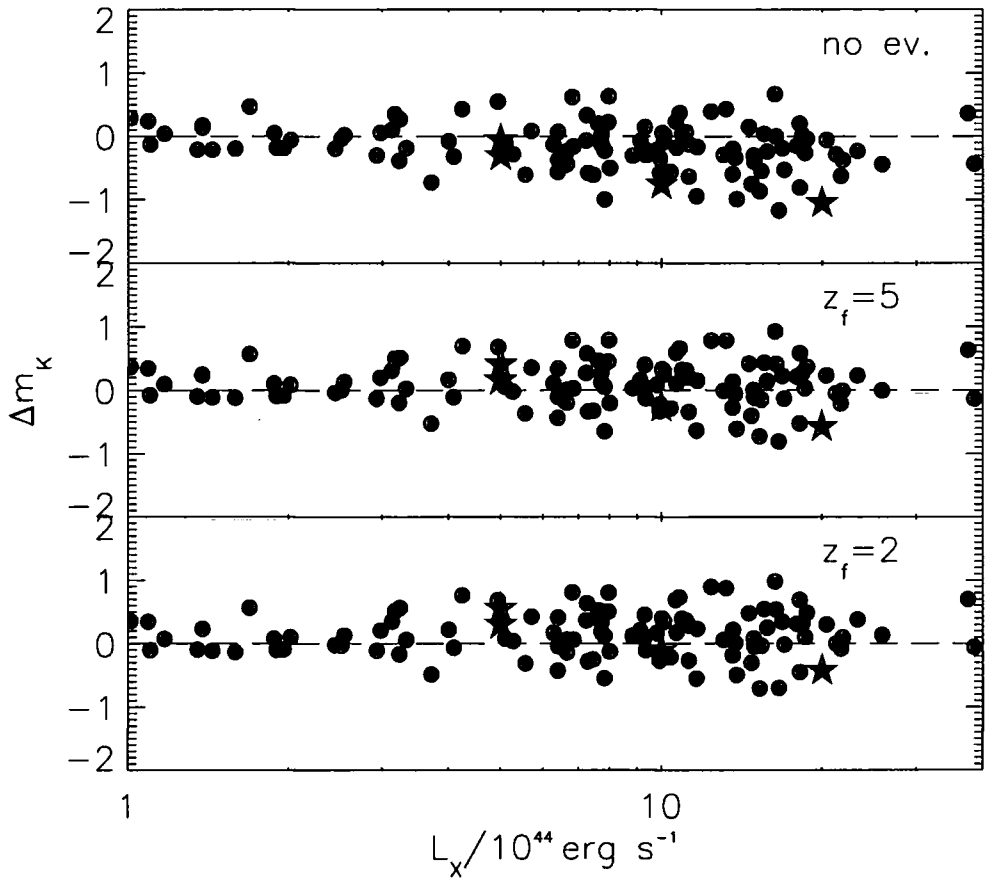

Figure 2.9: The residuals of the BCG corrected m_K about the non-evolution and the z_f =5 and z_f =2 passive evolution models from Fig. 2.8. $\Delta m_K = m_{BCG} - m_{model}$. The stars represent the WARPS BCGs.

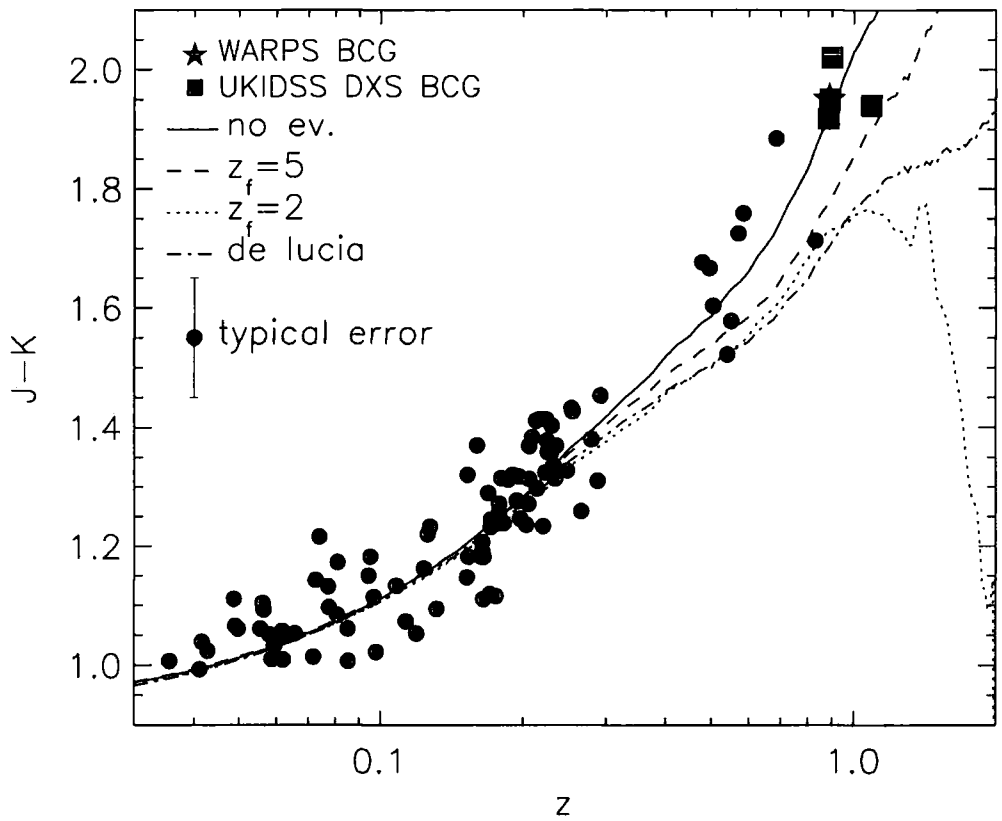

Figure 2.10: J-K vs z for the entire BCG sample. The Lines represent different models from the Bruzual & Charlot (2003) GALAXEV codes and the hierarchical merger model of De Lucia & Blaizot (2007). All of the GALAXEV models assume a Salpeter IMF and Solar metallicity. The De Lucia & Blaizot (2007) model forms 50 per cent of the BCG stellar content by $z \sim 5$ and 80 per cent by $z \sim 3$ with a Chabrier IMF. The WARPS BCG with J band data is from the cluster ClJ1226.9+3332.

2.3.5 Emission Lines

With the unprecedented wealth of colour information available for our sample in combination with spectroscopy from Crawford et al. (1999) we can investigate the sub-population of BCGs that have line emission. This emission originates from star forming activity attributed to cooling flows (see review by Fabian 1994). In this process intracluster gas cooling near the cluster centre accretes onto the BCG where it can trigger star formation and therefore line emission.

BCGs with the most luminous line emission (L(Hα) $> 10^{41}$erg s^{-1}) are found to have a significantly bluer continuum and therefore a bluer optical colour than those with less or no line emission (Crawford et al., 1999). Here we look for this same trend in the near-infrared colour which may aid selection of high redshift cooling flow clusters for future studies.

The Crawford et al. (1999) table of the *ROSAT* BCS (Ebeling et al. 1998) contains BCG emission line data for all of the members of the BCS sample. We have also obtained emission line data for more of our sample from the VLT (A. C. Edge private communication) and Keck (H. Ebeling private communication). This information is included in our $J-K$ vs z plot to see if there is any trend between line emission and near infrared colour (Fig. 2.11). For this plot the sample has been normalised to fit the $J-K$ non-evolution track from Fig. 2.10 to ensure there are no errors due to an unknown colour term.

Fig. 2.12 shows a histogram of the BCG distribution about the no evolution line in Fig. 2.11. Negative values are blue-ward of the model and positive values are red-ward. The figure shows that we find that both our high (L(Hα) $> 10^{41}$erg s^{-1}) and low luminosity Hα emitting BCG populations have a peak in the centre and then a blue tail. This is also seen in optical studies which find a Gaussian around the zero position and a number of populated bins tailing off on the blue side (e.g. Courtney 2003). We can therefore say that we do find a correspondence between the presence of BCG Hα emission lines and blue near-infrared colour.

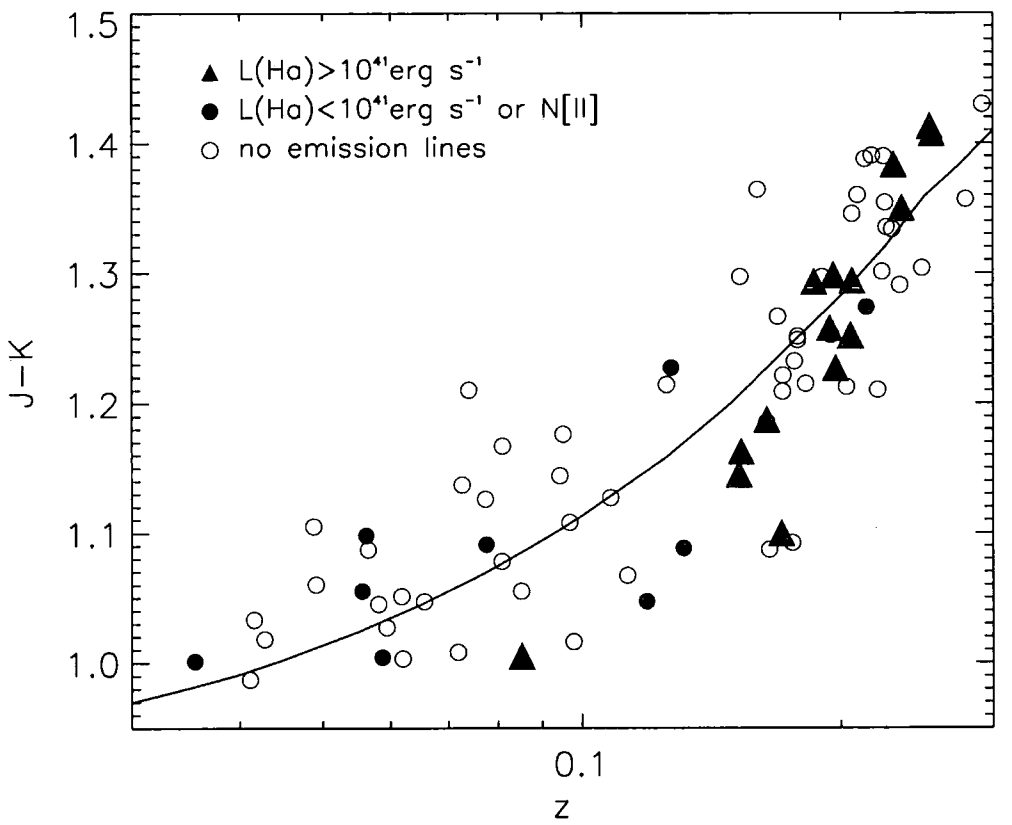

Figure 2.11: $J-K$ vs z for BCGs with spectral information normalised to the solid non-evolution line from figure 2.10.

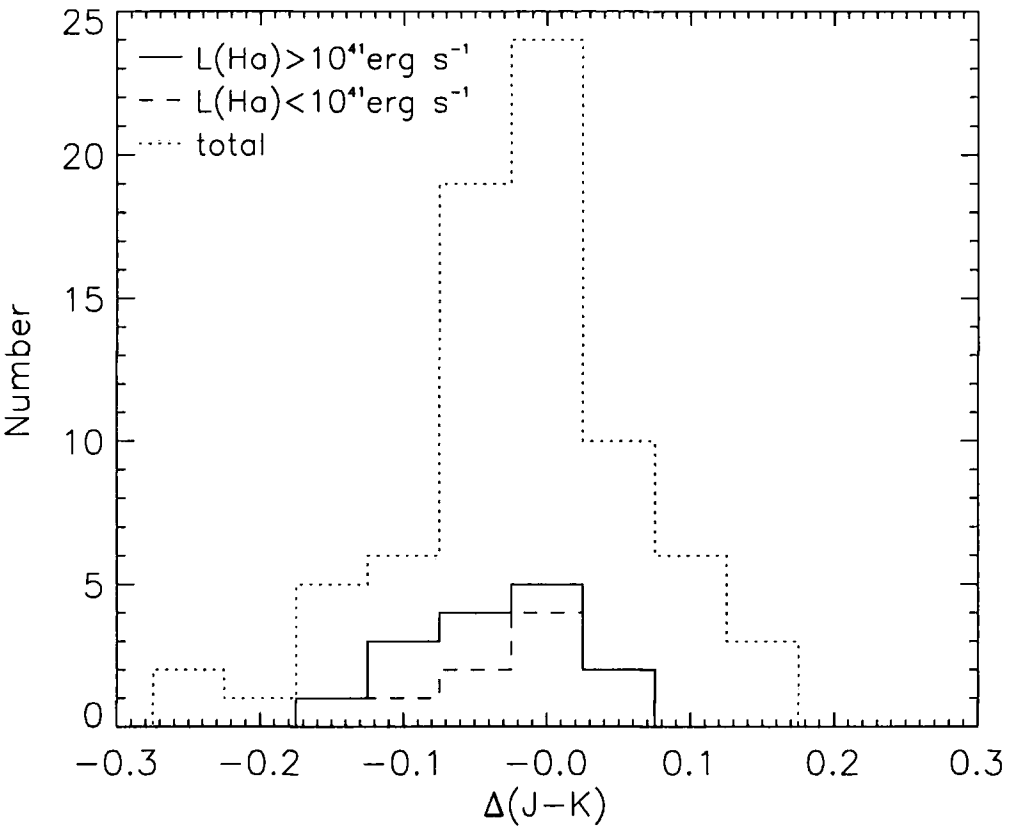

Figure 2.12: The histogram of the BCG distribution about the no evolution line. Negative values are blue-ward of the no evolution line, positive values are red-ward. A K-S test finds that there is a 35% probability that the BCGs with strong H_α emission are taken from the same parent population as the total BCG sample.

2.4 Summary

We have studied the evolution and environment of BCGs in the most X-ray luminous clusters since $z \sim 1$.

We find a positive relationship between the near infrared luminosity of the BCG and the X-ray luminosity of its host cluster for clusters where $L_X > 5 \times 10^{44}$erg s^{-1}. Previous studies have lacked the sample coverage of this work in the high L_X regime required to observe this trend. When a correction for this M_K–L_X relation is applied the scatter in the BCG absolute magnitude is reduced.

The K band Hubble diagram, which probes both build up of mass and stellar evolution of the BCGs, for the corrected sample is shown to follow passive evolution. This result is in agreement with the observations of Burke et al. (2000) and the simulations of De Lucia & Blaizot (2007).

To improve the constraints on BCG evolution we include J-band photometry allowing us to compare the $J - K$ colour vs redshift, which probes just the stellar evolution of our sample, to a set of evolution models . We find that the high redshift BCGs from our MACS, UKIDSS DXS and WARPS data appear to rule out passive evolution with a formation redshift less than 2. We therefore expect that the stellar population of BCGs has been in place since at least redshift 2, in agreement with the observations of Burke et al. (2000). However, the caveat to this result is that our high redshift BCGs are generally from higher L_X, and therefore higher mass, clusters which may introduce an evolutionary bias. For comparison with simulation, the De Lucia & Blaizot (2007) model (50 per cent stellar content in place by $z \sim 5$ and 80 per cent in place by $z \sim 3$) provides a good description to our observations at low z but is too blue compared to our current high z data. This suggests that the simulated BCGs form stars for a longer time period than the observed BCGs. We look to confirm this result in the future with additional high redshift data.

When studying the spectra of individual BCGs we observe a correlation between blue near-infrared colour and the presence of high luminosity (L(Hα) $> 10^{41}$erg s^{-1}) emission lines. Fig. 2.12 shows that such emission line BCGs mainly lie on the blue side of the near-infrared colour distribution. This has been seen previously in optical studies (Courtney 2003) and will be a useful tool in concert with X-ray observations

for selecting high redshift cooling flow clusters.

2.5 The BCG Sample

Cluster	ra	dec	z	J	K	M_K	L_X	$H_\alpha^\dagger$
	(J2000)						(10^{44}erg s^{-1})	
Abell 1902	14:21:40.53	+37:17:31.0	0.160	14.00	12.63	-26.42	5.56	n
Abell 193	01:25:07.62	+08:41:57.6	0.049	11.49	10.43	-26.12	1.59	n
Abell 1930	14:32:37.96	+31:38:48.9	0.131	13.57	12.47	-26.16	4.09	y
Abell 1991	14:54:31.48	+18:38:32.5	0.059	12.16	11.15	-25.77	1.38	y
Abell 2029	15:10:56.13	+05:44:42.4	0.077	11.43	10.30	-27.21	15.29	n
Abell 2034	15:10:11.71	+33:29:11.2	0.113	13.28	12.21	-26.10	6.85	n
Abell 2052	15:16:44.49	+07:01:17.7	0.035	10.88	9.88	-25.98	2.52	y
Abell 2065	15:22:24.02	+27:42:51.7	0.073	13.18	12.03	-25.34	4.94	n
Abell 2072	15:25:48.66	+18:14:09.5	0.127	14.05	12.82	-25.74	3.13	y
Abell 2107	15:39:39.05	+21:46:57.9	0.041	11.10	10.10	-26.07	1.10	n
Abell 2124	15:44:59.03	+36:06:34.1	0.066	12.10	11.05	-26.12	1.35	n
Abell 2175	16:20:31.14	+29:53:27.5	0.095	12.96	11.78	-26.17	2.93	n
Abell 2204	16:32:46.71	+05:34:30.9	0.152	13.37	12.23	-26.72	21.25	y
Abell 2244	17:02:42.50	+34:03:36.7	0.097	12.70	11.59	-26.40	9.34	n
Abell 2254	17:17:45.89	+19:40:48.4	0.178	14.60	13.34	-25.93	7.73	n
Abell 2259	17:20:09.65	+27:40:07.9	0.164	13.96	12.77	-26.33	6.66	n
Abell 2292	17:57:06.69	+53:51:37.5	0.119	13.12	12.06	-26.36	0.73	y
Abell 2345	21:27:13.72	-12:09:46.3	0.177	13.84	12.60	-26.65	9.93	n
Abell 2377	21:45:57.12	-10:06:18.7	0.081	13.16	12.07	-25.53	3.17	n
Abell 2382	21:51:55.63	-15:42:21.6	0.062	12.49	11.43	-25.61	0.91	n
Abell 2384	21:52:21.97	-19:32:48.6	0.094	13.74	12.59	-25.34	6.82	n
Abell 2402	21:58:28.89	-09:47:49.7	0.081	12.84	11.67	-25.94	2.02	n
Abell 2415	22:05:35.49	-05:32:09.7	0.058	12.51	11.46	-25.44	1.69	n
Abell 2426	22:14:31.59	-10:22:26.3	0.098	13.09	12.07	-25.94	5.10	n
Abell 2428	22:16:15.60	-09:19:59.7	0.085	12.71	11.64	-26.07	2.45	n
Abell 2443	22:26:07.93	+17:21:23.5	0.108	13.11	11.98	-26.24	3.23	n
Abell 2457	22:35:40.80	+01:29:05.6	0.059	11.86	10.83	-26.12	1.44	n
Abell 2495	22:50:19.73	+10:54:12.8	0.078	12.78	11.69	-25.83	2.98	y
Abell 2496	22:50:55.85	-16:24:22.0	0.123	13.09	11.92	-26.57	3.71	...
Abell 2589	23:23:57.45	+16:46:38.1	0.042	11.35	10.31	-25.89	1.88	n
Abell 2593	23:24:20.09	+14:38:49.7	0.043	11.38	10.36	-25.90	1.17	n
Abell 2597	23:25:19.72	-12:07:27.0	0.085	13.32	12.31	-25.40	7.97	y
Abell 2622	23:35:01.50	+27:22:20.5	0.062	12.39	11.38	-25.67	1.09	n
Abell 2626	23:36:30.59	+21:08:49.8	0.057	11.84	10.75	-26.10	1.96	n
Abell 2627	23:36:42.10	+23:55:29.1	0.126	13.73	12.51	-26.03	3.33	n
Abell 2665	23:50:50.56	+06:08:58.9	0.056	11.77	10.71	-26.10	1.90	y
Abell 2665	23:50:50.56	+06:08:58.9	0.056	11.85	10.74	-26.09	1.90	y
Abell 2717	00:03:12.98	-35:56:13.6	0.050	12.00	10.94	-25.64	1.01	...
Abell 2734	00:11:21.66	-28:51:15.5	0.062	12.22	11.17	-25.88	2.55	...
Abell 376	02:46:03.93	+36:54:18.8	0.049	11.89	10.78	-25.76	1.38	n
Abell 399	02:57:53.13	+13:01:51.2	0.072	11.85	10.84	-26.52	6.40	n
Abell 401	02:58:57.78	+13:34:57.7	0.074	12.13	10.91	-26.50	9.94	n

Table 2.1: The $z \lesssim 0.15$ 2MASS BCGs. † denotes prescence of H_α emission. y: H_α emission, n: no H_α emission

Cluster	ra	dec	z	J	K	M_K	L_X	$H_\alpha^\dagger$
	(J2000)						(10^{44}erg s^{-1})	
Abell 115	00:56:00.24	+26:20:31.7	0.197	14.65	13.40	-26.09	14.59	y
Abell 1201	11:12:54.50	+13:26:08.9	0.169	14.45	13.16	-26.00	6.28	n
Abell 1204	11:13:20.52	+17:35:42.5	0.171	14.70	13.58	-25.60	7.26	y
Abell 1246	11:23:58.75	+21:28:47.3	0.190	14.99	13.67	-25.74	7.62	n
Abell 1423	11:57:17.38	+33:36:40.9	0.213	15.06	13.65	-26.01	10.03	n
Abell 1553	12:30:48.94	+10:32:48.4	0.165	13.71	12.60	-26.51	7.30	n
Abell 1682	13:06:45.82	+46:33:32.9	0.234	14.43	13.12	-26.75	11.26	n
Abell 1704	13:14:24.67	+64:34:32.2	0.221	14.79	13.56	-26.18	7.83	n
Abell 1758	13:32:38.59	+50:33:38.7	0.279	15.34	13.96	-26.29	11.68	n
Abell 1763	13:35:20.14	+41:00:03.8	0.223	14.44	13.11	-26.64	14.93	n
Abell 1835	14:01:02.06	+02:52:43.1	0.253	14.36	12.92	-27.11	38.53	y
Abell 1914	14:25:56.64	+37:48:59.4	0.171	14.09	12.85	-26.34	18.39	n
Abell 1961	14:44:31.82	+31:13:36.7	0.232	14.86	13.52	-26.32	6.60	...
Abell 2009	15:00:19.51	+21:22:10.6	0.153	14.02	12.83	-26.12	9.12	y
Abell 209	01:31:52.51	-13:36:41.0	0.209	14.46	13.07	-26.54	13.75	n
Abell 2111	15:39:41.81	+34:24:43.3	0.229	15.10	13.75	-26.07	10.94	n
Abell 2163	16:15:33.57	-06:09:16.8	0.203	14.98	13.24	-26.31	37.50	n
Abell 2218	16:35:49.39	+66:12:45.1	0.176	14.46	13.35	-25.90	9.30	n
Abell 2219	16:40:19.90	+46:42:41.4	0.226	14.70	13.34	-26.44	20.40	n
Abell 2254	17:17:45.91	+19:40:49.3	0.178	14.46	13.19	-26.09	7.73	n
Abell 2261	17:22:27.24	+32:07:57.9	0.224	14.04	12.62	-27.14	18.18	n
Abell 2445	22:26:55.80	+25:50:09.4	0.165	14.40	13.22	-25.89	4.00	...
Abell 2561	23:13:57.31	+14:44:21.9	0.163	14.71	13.53	-25.55	3.24	...
Abell 291	02:01:46.80	-02:11:56.9	0.196	15.42	14.10	-25.37	4.24	y
Abell 521	04:54:06.86	-10:13:23.0	0.248	14.86	13.53	-26.45	8.01	n
Abell 586	07:32:20.26	+31:38:01.9	0.171	14.36	13.13	-26.06	11.12	n
Abell 661	08:00:56.78	+36:03:23.6	0.288	14.84	13.53	-26.79	13.60	...
Abell 665	08:30:57.34	+65:50:31.4	0.182	14.92	13.69	-25.63	16.33	n
Abell 68	00:37:06.82	+09:09:24.3	0.255	14.94	13.51	-26.54	14.89	n
Abell 750	09:09:12.70	+10:58:27.9	0.180	14.36	13.05	-26.25	9.30	n
Abell 773	09:17:53.57	+51:44:02.5	0.217	14.64	13.22	-26.48	13.08	n
Abell 907	09:58:21.98	-11:03:50.3	0.153	14.50	13.18	-25.76	7.95	n
Abell 963	10:17:03.65	+39:02:52.0	0.206	14.31	12.94	-26.64	10.41	n
RX J1720.1+2638	17:20:10.08	+26:37:33.5	0.164	14.18	12.97	-26.13	6.66	y
RX J2129.6+0005	21:29:39.91	+00:05:19.7	0.235	14.64	13.27	-26.60	18.59	y
Zw 1432	07:51:25.15	+17:30:51.8	0.186	14.62	13.31	-26.06	5.27	y
Zw 1693	08:25:57.82	+04:14:48.7	0.225	14.62	13.24	-26.53	7.46	n
Zw 1883	08:42:55.99	+29:27:26.0	0.194	14.50	13.22	-26.23	6.41	y
Zw 2089	09:00:36.86	+20:53:41.2	0.230	15.50	14.10	-25.73	10.82	y
Zw 2379	09:27:10.68	+53:27:33.7	0.205	15.13	13.86	-25.72	5.71	y
Zw 2701	09:52:49.22	+51:53:05.8	0.214	14.70	13.40	-26.27	10.68	y
Zw 348	01:06:50.60	+01:04:10.1	0.255	15.21	13.78	-26.26	9.80	y
Zw 3916	11:14:27.43	58:22:43.5	0.206	15.11	13.80	-25.79	6.41	y
Zw 5247	12:34:17.45	+09:45:59.4	0.195	14.69	13.41	-26.05	10.12	n
Zw 5768	13:11:46.22	+22:01:37.2	0.266	14.33	13.08	-27.07	11.64	...
Zw 7215	15:01:23.09	+42:20:39.8	0.292	15.57	14.12	-26.23	11.26	n

Table 2.2: The $0.15 \lesssim z \lesssim 0.3$ WIRC BCGs. † denotes prescence of H_α emission. y: H_α emission, n: no H_α emission

Cluster	ra	dec	z	J	K	M_K	L_X
	(J2000)						(10^{44}erg s^{-1})
MACS J0018.5+1626	00:18:33.68	+16:26:15.1	0.541	16.87	15.35	-26.48	18.74
MACS J0150.3-1005	01:50:21.24	-10:05:29.6	0.363	0.00	13.90	-26.95	7.83
MACS J0329.6-0211	03:29:41.68	-02:11:48.9	0.451	0.00	14.13	-27.24	13.85
MACS J0404.6+1109	04:04:32.71	+11:08:03.5	0.358	0.00	13.82	-27.00	14.75
MACS J0429.6-0253	04:29:36.14	-02:53:08.3	0.397	0.00	13.58	-27.48	16.61
MACS J0454.1-0300	04:54:11.13	-03:00:53.8	0.550	16.87	15.29	-26.58	16.86
MACS J0647.7+7015	06:47:51.45	+70:15:04.4	0.584	16.63	14.87	-27.16	21.70
MACS J0744.8+3927	07:44:51.98	39:27:35.1	0.686	17.21	15.33	-27.11	25.90
MACS J1359.8+6231	13:59:54.32	+62:30:36.3	0.330	0.00	14.32	-26.31	8.83
MACS J2050.7+0123	20:50:43.12	+01:23:29.4	0.333	0.00	14.67	-25.98	7.24
MACS J2214.9-1359	22:14:56.51	14:00:17.2	0.495	16.38	14.71	-26.89	17.00
MACS J2241.8+1732	22:41:56.18	+17:32:12.1	0.317	0.00	14.39	-26.15	10.10
MACS J2245.0+2637	22:45:04.62	+26:38:05.2	0.301	0.00	14.03	-26.39	13.62
RCS0224-0002	02:24:00.00	-0:02:00.0	0.770	0.00	16.87	-25.87	0.70
MS1054-0321	10:57:00.20	-03:37:27.4	0.830	17.70	15.99	-26.93	23.30

Table 2.3: The $z \gtrsim 0.3$ MACS and archival BCGs

Chapter 3

The build up of the cluster red sequence

Overview

We compare the luminosity functions for red galaxies lying on the restframe $(U-V)$ colour-magnitude sequence in a homogeneous sample of ten X-ray luminous clusters at $z \sim 0.5$ to a similarly selected X-ray cluster sample at $z \sim 0.1$. We exploit deep *Hubble Space Telescope* ACS imaging in the F555W and F814W passbands of the central 1.2-Mpc diameter regions of the distant clusters to measure precise colours for the galaxies in these regions and statistically correct for contamination by field galaxies using observations of blank fields. We apply an identical analysis to ground-based photometry of the $z \sim 0.1$ sample. This comparison demonstrates that the number of faint, $M_V \sim -19$, red galaxies relative to the bright population seen in the central regions of massive clusters has roughly doubled over the 4 Gyrs between $z \sim 0.5$ and $z \sim 0.1$. We quantify this difference by measuring the dwarf to giant ratio on the red sequence which increases by a factor of at least 2.2 ± 0.4 since $z \sim 0.5$. This is consistent with the idea that many faint, blue star-forming galaxies in high density environments are transforming onto the red sequence in the last half of the Hubble time.

3.1 Introduction

Recent studies have precisely quantified the variation in the photometrically classified galaxy population as a function of environment at low redshifts (Hogg et al. 2004). These studies separate galaxies into red passive or blue star-forming systems and find that the proportion of the latter decreases in higher density regions in the local Universe (Baldry et al., 2006). The identification of the physical process responsible for this trend is still contentious, in part because it is likely that a number of processes contribute in different environments, at different epochs and acting on galaxies of different luminosities/masses. The presence of a range of potential evolutionary pathways linking star forming and passive galaxies may be reflected in the diversity of star formation histories derived for passive early type galaxies. While the formation of luminous early type galaxies in clusters has been interpreted in terms of a narrow range in star formation histories (Aragon-Salamanca et al., 1993; Bower et al., 1992; Stanford et al., 1998; van Dokkum et al., 1998), there is evidence of much more variety in lower luminosity systems (see Ferguson & Binggeli, 1994, for a review). Several lines of evidence illustrate this, for example Poggianti et al. (2001) find a broad range in ages but a slight decrease in age for fainter dwarf galaxies in the Coma cluster. Smail et al. (2001) reached a similar conclusion for the luminosity weighted ages of low luminosity early type galaxies in the $z = 0.18$ cluster A 2218. An even wider variety is found in much lower luminosity systems, Grebel (1999) finds that star formation timescales and ages vary significantly for the local group dwarf ellipticals. Indeed, this same effect may underlie the varying morphological mix seen in the passive galaxy populations in clusters, where there is a claim of a deficit of early type disk galaxies (predominantly S0) in distant clusters (Dressler et al. 1997). Thus it appears that passive galaxies may be formed via a number of different processes and that the mixed nature of the population may be most easily discerned at the lowest luminosities.

These different pathways may also result in a changing passive galaxy population in clusters at different redshifts. The most fundamental measure of the transformational processes forming passive galaxies in high density regions is to look at the build up of the luminosity function of this population. De Lucia et al. (2004) inves-

tigated this scenario by measuring the colour-magnitude relation in four optically selected $z \sim 0.75$ clusters and comparing these to the nearby Coma cluster. They find that the high redshift clusters exhibit a deficiency in low luminosity red galaxies compared to Coma. Similarly, Kodama et al. (2004) found a deficit of red sequence galaxies when looking at high density regions at $z \sim 1$ in the Subaru/*XMM-Newton* Deep Survey. This led them to conclude that many faint red galaxies in clusters have only moved onto the red sequence since $z \sim 0.75$ (see also De Lucia et al. 2007). This result is controversial as Andreon (2006) claims there is no evidence for this red sequence build up when comparing the luminosity function of a cluster at $z = 0.831$ to those of local clusters.

In this chapter we aim to test these results by comparing the evolution in the luminosity function of galaxies on the red sequence in two well-defined samples of X-ray selected clusters at $z \sim 0.5$ and $z \sim 0.1$. We employ *Hubble Space Telescope (HST)* optical imaging of ten $z \sim 0.5$ X-ray luminous clusters and compare these to a similar sample at $z \sim 0.1$ to examine evolution in the faint end of the red sequence luminosity function. In the ΛCDM cosmology we adopt lookback times to $z = 0.13$ and 0.54 of 1.6 and 5.3 Gyrs and angular scales such that $1''$ corresponds to 2.3 and 6.4 kpc respectively. An AB magnitude system is used throughout this chapter.

3.2 Observations and Reduction

Our analysis employs restframe optical imaging of two cluster samples at $z \sim 0.1$ and $z \sim 0.5$. The $z \sim 0.5$ sample are selected from the MAssive Cluster Survey (MACS, Ebeling et al. 2001). MACS is a survey of distant X-ray luminous, ($L_X > 10^{44}\,\mathrm{erg\,s^{-1}}$) and therefore massive, galaxy clusters selected from the *ROSAT* All-Sky Survey. The ten clusters in this sample, along with a further two for which archival *HST* observations exist, are the twelve most distant clusters, $z \sim 0.5$–0.7, from MACS and all have X-ray luminosities of $L_X(0.1\text{–}2.4\,\mathrm{keV}) > 15 \times 10^{44}\,\mathrm{erg\,s^{-1}}$ (Table 3.1). These ten clusters were imaged with the Advanced Camera for Surveys (ACS) Wide Field Channel (WFC) on *HST* during Cycle 12 (GO#9722). Each cluster was imaged for two orbits (4.5 ks) through both the F555W (V_{555}) and F814W

(I_{814}) filters. These data were retrieved from the STScI archive and reduced using standard STScI software (MULTIDRIZZLE v2.7) to provide final images with 0.05″ sampling and good cosmetic properties.

We extracted the photometry from the ACS images using SExtractor (Bertin & Arnouts, 1996) run in dual-image mode so that photometric information from the V_{555}-band was extracted for all sources detected on the I_{814}-band image and ensuring that we have precise aperture photometry for even crowded sources. Throughout this chapter we use 1.4-″ apertures (9 kpc diameter) to calculate the $(V_{555} - I_{814})$ colour and the 'Best' magnitude is used for the total I_{814}-band magnitude (these correspond closely to restframe $(U - V)$ colours and V absolute magnitudes).

The low-redshift, $z \sim 0.1$, comparison sample for our analysis comes from the Las Campanas/AAT Rich Cluster Survey (LARCS, Pimbblet et al. 2001, 2006). This survey obtained panoramic, ground-based B- and R-band imaging of ten X-ray luminous ($L_X > 5 \times 10^{44}\,\mathrm{erg\,s^{-1}}$) clusters at $z = 0.08$–0.15 selected from the *ROSAT* All-Sky Survey (Table 3.1). The observations and their reduction and analysis are described in detail in Pimbblet et al. (2001). We use 4-″ $(B - R)$ colours (corresponding to restframe $(U-V)$ colours in 9 kpc apertures) and total magnitudes derived from these restframe $\sim V$-band selected galaxy catalogues in our analysis. These data are thus well-matched to the observations of the distant sample: the absolute V-band surface brightness limits are $\mu_V = -15.4$ and -15.8 mag. arcsec^{-2} for LARCS and MACS respectively, with spatial resolution of 2.8 and 1.0 kpc. In our analysis we only consider the inner parts of each cluster, within a radius of 600 kpc of the cluster centre as identified from the X-ray emission (usually corresponding to the position of the brightest cluster galaxy) as this provides uniform coverage across both the LARCS and MACS datasets.

Both the MACS and LARCS cluster samples were selected from the same X-ray survey and the luminosities for the clusters are sufficiently large that they should correspond to some of the most extreme environments at their respective epochs. The median X-ray luminosities of the high- and low-redshift samples are 17.0 and $7.3 \times 10^{44}\,\mathrm{ergs\,s^{-1}}$ respectively, corresponding to a difference of less than a factor of two in the typical total mass (Reiprich & Boehringer, 2002). However, an im-

portant issue to address is that the mass of the $z \sim 0.5$ progenitors of the LARCS clusters would be even lower than the MACS clusters. Using the results of Tormen (1998) we see that the progenitors of the LARCS clusters at $z \sim 0.5$ would be $\sim 3.5\times$ less massive than the MACS sample (with corresponding X-ray luminosities of $\sim 2 \times 10^{44}\,\mathrm{ergs\,s^{-1}}$, Reiprich & Boehringer (2002)). There is no evidence for strong variations in the galaxy luminosity function between clusters spanning such a relatively modest difference in typical mass (de Propris et al., 1999). In addition, Wake et al. (2005) see no variation in the blue galaxy fraction in clusters covering a similar range in mass. Combining these two results, we therefore expect that any differences between the galaxy populations in these two samples will primarily reflect evolutionary differences between $z \sim 0.5$ and $z \sim 0.1$.

Finally, to better define the evolutionary trends we are searching for, we also include similar observations of seven additional clusters in our analysis of the dwarf-giant ratio in §3.3.3. We include a low redshift point from U- and V-band observations of the Coma cluster from a dataset of known members (Godwin et al., 1983). This is well matched to our main MACS and LARCS samples. Next, we include four additional clusters which are at redshifts intermediate between the LARCS and MACS samples and a further two clusters at redshift beyond the MACS sample (see Table 3.1). These clusters all have deep archival observations with *HST* in the F555W/F606W and F814W filters (from GO projects 9033, 9290, 9722, 10325, 10491, 10872 and 10875) and we obtain the data from the *HST* archive. We note that the *HST* ACS observations of the four intermediate clusters do not reach the 600-kpc radius adopted for our analysis and so we have corrected the dwarf-giant ratio using the average observed radial trend in this ratio for the composite MACS sample. The dwarf-giant ratio is observed to increase in value from the cluster centre outwards and flatten at larger radii. For the most extreme case, cluster Abell 1703 at $z = 0.258$, this correction gives an enhancement of 15% in dwarf-giant ratio. In addition we caution that the K-corrections for the additional *HST* clusters are not as well-matched to restframe $(U - V)$ as those for the LARCS or MACS samples and so there may be systematic uncertainties related to these data points.

Table 3.1: Details of the cluster samples used in our analysis.

Cluster	R.A. (J2000)	Dec.	z	L_X (10^{44}erg s^{-1})	N^1_{Red}	DGR
MACS $z \sim 0.5$ Sample						
MACS J0025.4−1222	00 25 15.84	−12 19 44	0.478	12.4	168±13	1.56±0.35
MACS J0257.6−2209	02 57 07.96	−23 26 08	0.504	15.4	157±13	1.47±0.34
MACS J0647.7+7015	06 47 51.45	+70 15 04	0.584	21.7	183±14	1.39±0.29
MACS J0717.5+3745	07 17 31.83	+37 45 05	0.548	27.4	321±18	1.25±0.20
MACS J0744.8+3927	07 44 51.98	+39 27 35	0.686	25.9	173±13	1.00±0.22
MACS J0911.2+1746	09 11 10.23	+17 46 38	0.506	13.2	169±13	1.54±0.34
MACS J1149.5+2223	11 49 34.81	+22 24 13	0.544	17.3	266±16	1.43±0.25
MACS J1423.8+2404	14 23 47.95	+24 04 59	0.544	15.0	155±13	1.11±0.25
MACS J2129.4−0741	21 29 25.38	−07 41 26	0.570	16.4	194±14	1.27±0.26
MACS J2214.9−1359	22 14 56.51	−14 00 17	0.495	17.0	215±15	1.25±0.24
LARCS $z \sim 0.1$ Sample						
Abell 22	00 20 38.64	−25 43 19	0.142	5.3	220±21	2.55±0.64
Abell 550	05 52 51.84	−21 03 54	0.099	7.1	277±22	2.05±0.43
Abell 1084	10 44 30.72	−07 05 02	0.132	7.4	111±18	4.00±1.79
Abell 1285	11 30 20.64	−14 34 30	0.106	5.45	391±25	2.94±0.53
Abell 1437	12 00 25.44	+03 21 04	0.134	7.7	376±25	2.04±0.35
Abell 1650	12 58 41.76	−01 45 22	0.084	7.8	182±20	3.00±0.88
Abell 1651	12 59 24.00	−04 11 20	0.085	8.3	232±21	4.52±1.24
Abell 1664	13 03 44.16	−24 15 22	0.128	5.34	127±18	2.49±0.91
Abell 2055	15 18 41.28	+06 12 40	0.102	4.8	201±21	4.54±1.37
Abell 3888	22 34 32.88	−37 43 59	0.153	14.5	124±19	1.89±0.68
Additional Clusters						
Cl J0152−1357	01 52 43.91	−13 57 21	0.831	5.0	276±17	0.77±0.14
MACS J0451.9+0006	04 51 54.63	+00 06 18	0.430	10.4	179*±14	1.41±0.30
MACS J0712.3+5931	07 12 20.45	+59 32 20	0.328	6.8	90*±10	1.63±0.44
Cl J1226.9+3332	12 26 58.13	+33 32 49	0.890	20.0	232±15	1.16±0.22
Abell 1703	13 15 00.70	+51 49 10	0.258	8.7	94†±10	3.48±1.13
MACS J1354.6+7715	13 54 19.71	+77 15 26	0.397	8.2	156†±13	1.66±0.37

1) N_{red} is the number of galaxies on the red sequence down to $M_V = -17.75$ within a 600 kpc radius of cluster centre except: $\star$ within a 400 kpc radius, † within a 300 kpc, due to the size of the ACS image. The limited radius of MACS 1354 is due to size of ACS image and flaring on the image from a bright star. The LARCS redshifts are from Pimbblet et al. (2006). MACS redshifts come from Ebeling et al. (2007).

3.3 Analysis and Discussion

We show in Fig. 3.1 the colour-magnitude diagrams for the individual MACS $z \sim 0.5$ clusters (similar plots for the individual LARCS clusters are given in Pimbblet et al. 2002). These display strong linear features in the distributions of the brighter and redder galaxies in the fields. These are the colour-magnitude relations for the passive, early-type cluster members (Bower et al., 1992; Sandage & Visvanathan, 1978). For the brighter galaxies in the clusters this sequence is thought to represent variations in the metallicity and to a lesser extent age of the stellar populations in the galaxies (Chapter 4, Kodama & Arimoto 1997; Terlevich et al. 2001).

As our MACS and LARCS cluster samples are homogeneously selected and observed and cover a small range in redshift ($\delta z/z \sim 0.15$), we are able to combine them to reduce the influence of variations in field contamination and to improve the statistics of our analysis. We show in Figs 3.2 and 3.3 the combined colour-magnitude relations for the MACS and LARCS samples. The combined colour-magnitude plots were created by correcting the data to the median redshifts of the MACS and LARCS samples, $z = 0.54$ and $z = 0.13$ respectively, using the K-corrections from a Bruzual & Charlot (2003) solar metallicity, simple stellar population, $z_f = 5$ model and the appropriate distance modulae. We also define limits to the colour-magnitude relation in these combined samples to allow us to quantitatively compare them. We define the limits on the basis of an error weighted two-parameter fit to the slope of the combined MACS red sequence with a stripe width of 0.75 mags which is chosen to include the observed scatter while limiting contamination from foreground and background sources. The corresponding boundaries for the LARCS red sequence are then determined by K-correcting and colour converting the limits from the MACS sample using Bruzual & Charlot (2003) and the formulae given in Skiff (2003) and Natali et al. (1994). A correction for the observed change in red sequence slope between the two epochs is also included by using the gradient found from error weighted fitting to the combined LARCS red sequence. We plot in Figs 3.2 and 3.3 the corresponding colour boundaries for the two samples. It is these red sequences that are used below to estimate the combined red sequence luminosity functions and the relevant field correction.

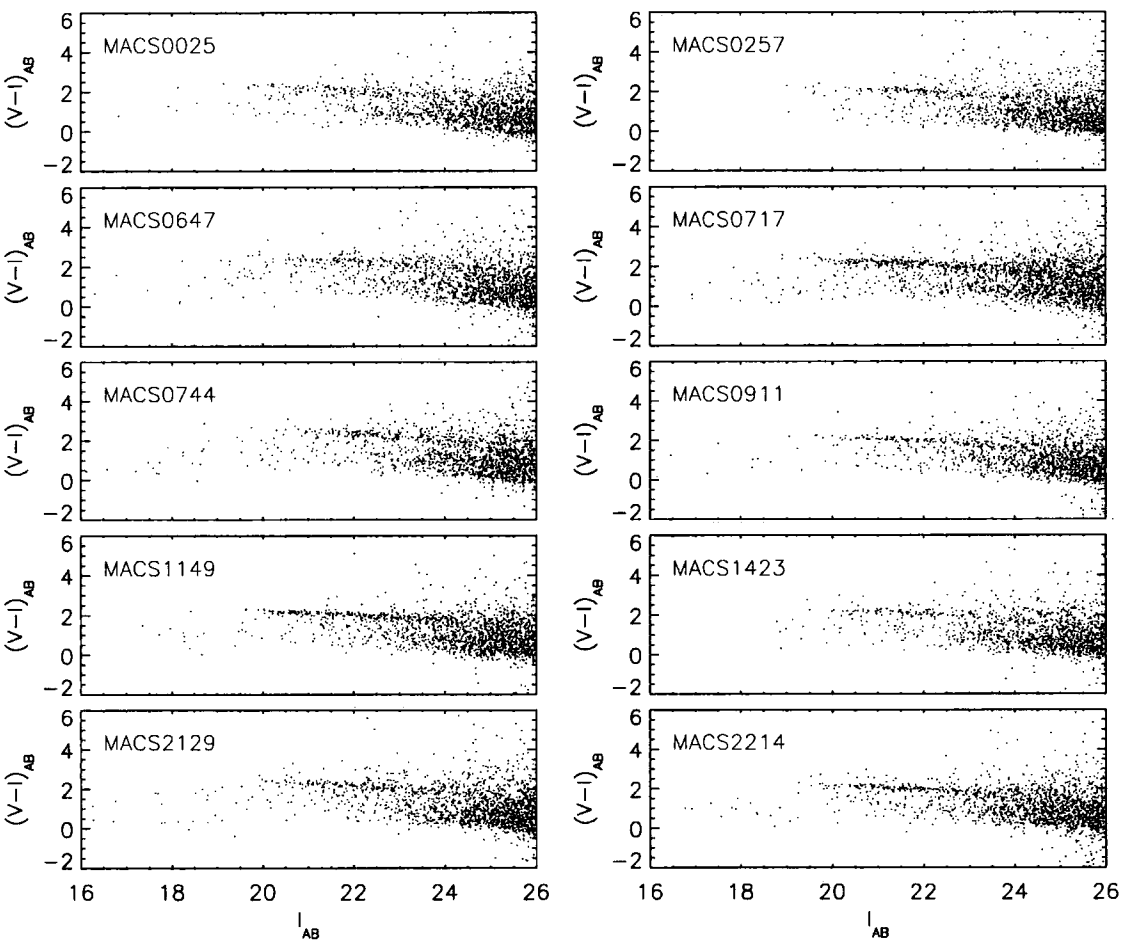

Figure 3.1: The individual ($V_{555} - I_{814}$) colour-magnitude diagrams for the MACS clusters. Colour-magnitude plots for individual clusters in the LARCS survey can be found in Pimbblet et al. (2002).

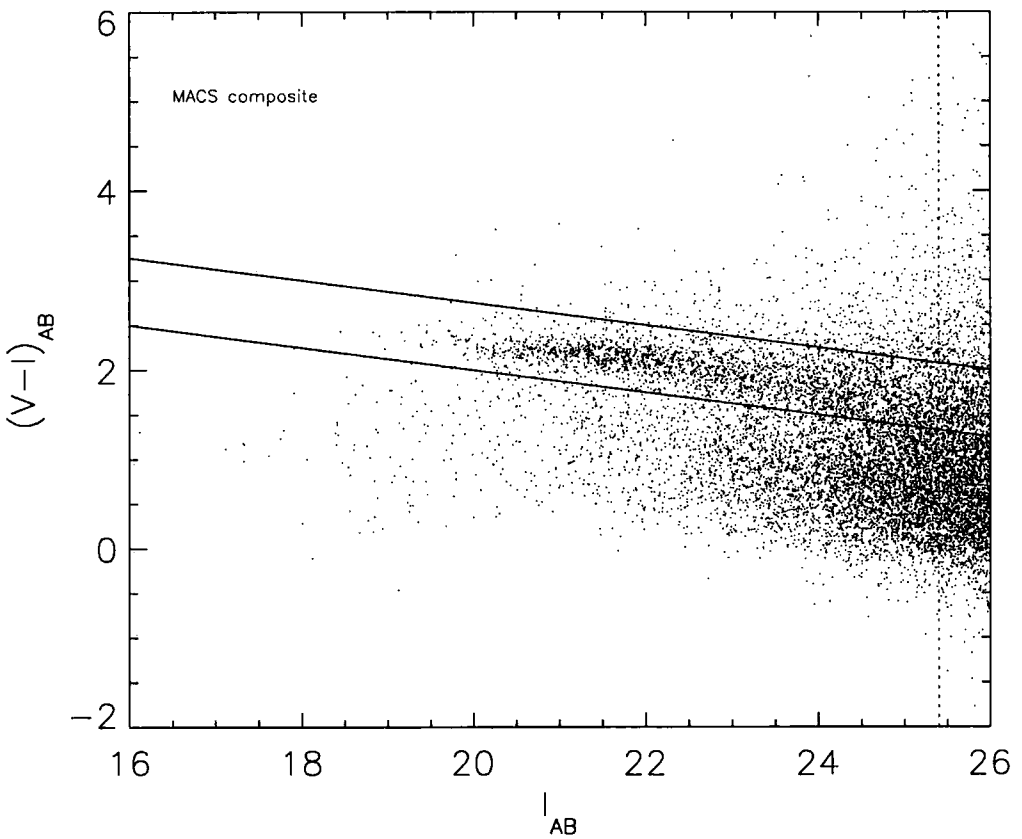

Figure 3.2: The combined $(V-I)$–I colour-magnitude diagram for the MACS sample (corresponding to restframe $(U-V)$–V), all clusters have been K-corrected to $z = 0.54$. The solid lines show the limits used to define and select the red sequence in the combined clusters and the dotted line is the 5-σ limit $I = 25.4$.

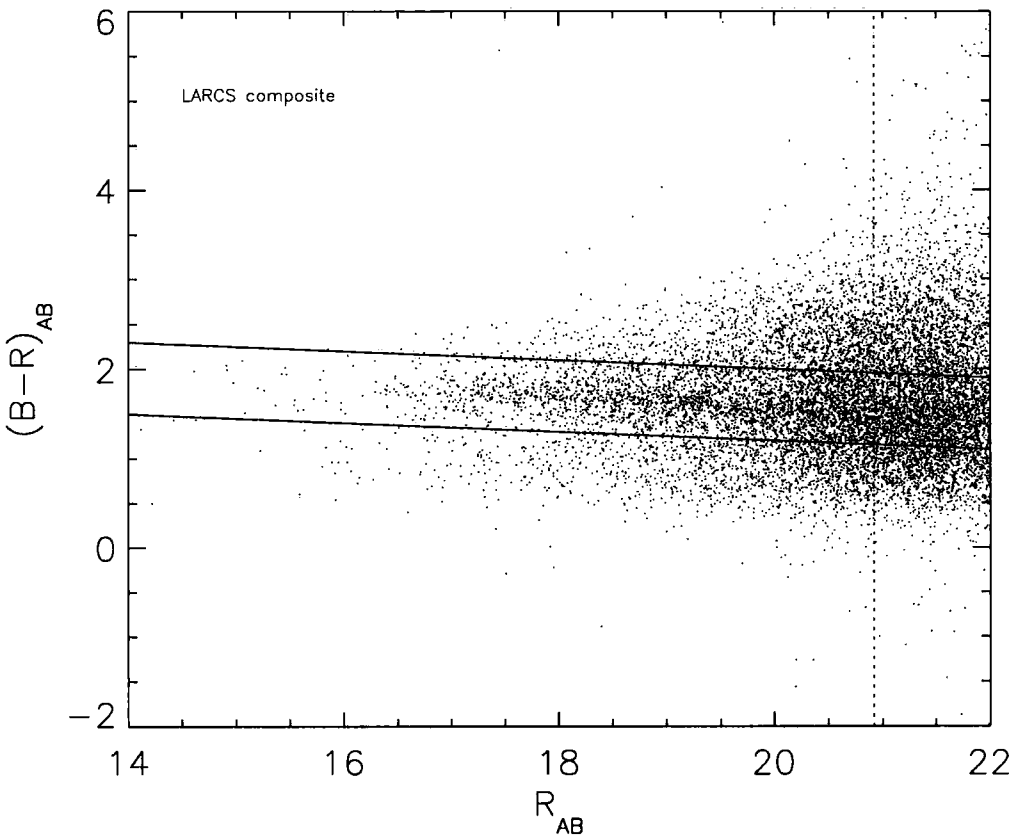

Figure 3.3: The combined $(B-R)$–R (restframe $(U-V)$–V) colour-magnitude diagram for the LARCS sample. The dotted line denotes the 5-σ limit of $R = 20.92$ and all clusters have been K-corrected to $z = 0.13$. Again the solid lines show the limits used to select the red sequence in the combined clusters, these are transformed from the equivalent boundaries for the MACS sample as described in the text.

3.3.1 Field Correction

The removal of field galaxies from our samples is crucial to provide a clean measurement of the cluster luminosity function. For the MACS *HST* sample we used blank fields from The Great Observatories Origins Deep Survey North (GOODS, Giavalisco et al. 2004). These provide estimates of the correction for field contamination in each bin in our colour-selected luminosity functions. The variation in this correction between independent 16 arcmin^2 subregions of the 112 arcmin^2 blank field is included in the luminosity function errors. The correction for field contamination for the ground-based observations of the LARCS sample is calculated in a similar way. Here, however, we make use of the fact that the panoramic, 2-degree diameter, imaging of these clusters extends into the field population surrounding the clusters and so we can use the outskirts of the images to determine the field contamination. These estimates have been shown to be robust by Pimbblet et al. (2002). Again we determine the reliability of our field corrections by dividing the total 4600 arcmin^2 field region into 290 arcmin^2 subregions and determining the scatter in these independent areas. These field subregions are on scales comparable to the regions of the MACS and LARCS clusters we analyse. The typical 1-sigma errors for the field correction are in the region of 10 percent for MACS and 20 percent for LARCS. We propagate these uncertainties through our entire analysis.

An additional source of contamination comes from higher redshift galaxies that have been gravitationally lensed by our clusters. This would effectively alter the field contamination in our sample, either increasing or decreasing it depending upon the slope of the number counts (Taylor et al., 1998). To estimate the scale of this effect we compare the number counts of galaxies on the colour-magnitude plane which are just redward of the cluster's colour-magnitude sequence (and hence should be at higher redshifts) to similar regions of the colour-magnitude plane for the blank fields. This provides an estimate of the potential enhancement in the surface density of red galaxies in the cluster centres due to lensing of $\sim$0.1 percent. Although only a very small effect, we include this factor in the field correction.

3.3.2 Luminosity Function

The field-corrected luminosity functions for the two composite cluster samples are shown in Fig. 3.4. Luminosity functions are traditionally fitted with a single Schechter function (Schechter, 1976). Recent papers on clusters, however, have instead fitted a Gaussian to the bright end of the luminosity function and a Schechter function to the faint end as these give a better fit to observations (Dahlen et al., 2004; Thompson & Gregory, 1993). We compare the single Schechter to the Gaussian+Schechter parameterisation of the luminosity function for galaxies on the red sequences in the LARCS and MACS samples. To avoid incompleteness we only consider the luminosity function down to the K-corrected 5-σ limit of the highest redshift cluster in the shallower LARCS data ($R = 20.92$ from A 3888 corresponding to $M_V = -17.75$). Table 3.3.2 contains the best-fit Schechter and Gaussian parameters converted to absolute V-band magnitudes using the method described above and the reduced χ^2 for these fits. The errors quoted here are estimated using a bootstrap method.

When fitting combined Gaussian+Schechter functions we fix the mean magnitude and width of the Gaussian components (Table 3.3.2), within their errors, so as to constrain the evolution of the bright-end Gaussian between $z \sim 0.5$ and $z \sim 0.1$. We do this as the luminosity evolution of galaxies in the bright end of the LF is well-constrained from fundamental plane studies (van Dokkum et al., 1998) and so we can focus on changes in the faint-end. The passive evolution of the luminosity between the two epochs is fixed as 0.3 magnitudes from van Dokkum & Franx (2001). We find that both a Gaussian+Schechter or a Schechter function give acceptable fits to our two samples. Both parametric forms also demonstrate the same difference between the two samples: an increase in the number of faint red galaxies compared to the brighter red population at lower redshifts. For the Schechter fits this is shown by the steeper faint end slope (α) in the LARCS clusters than MACS clusters, -1.11 ± 0.06 versus -0.91 ± 0.02 respectively, a difference of approximately 3.2σ. We find no evidence for variations of the form of the luminosity function looking at either the bluest or reddest halves of the colour-magnitude sequence or between different clusters when ranked by richness.

For the Gaussian+Schechter fits, the change in the luminosity function is shown

in part by the relative normalisation of the faint Schechter and bright Gaussian components, ϕ^*/Amp, which decreases from 1.94 ± 0.58 in LARCS to 1.26 ± 0.67 for the MACS sample. However, the covariance between the parameters in the two components functional fits makes such a comparison complex to interpret and so we turn to another, shape-independent, parameterisation of the relative numbers of faint and luminous galaxies: the dwarf-giant ratio.

3.3.3 Dwarf-Giant Ratio

The results from §3.3.2 are difficult to interpret in part because the form of the luminosity function is complex and its evolution is uncertain. A far simpler approach to quantify the relative evolution of the numbers of bright and faint galaxies is to use the ratio of the number of dwarfs to giants along the red sequence: the Dwarf-Giant Ratio (DGR) which provides a single number to parameterize the distribution of galaxy luminosities within a population. The variation of this quantity (or its inverse GDR) with distance from cluster centre, density and cluster richness have been studied by a number of workers (Dahlen et al., 2004; Driver et al., 1998; Goto et al., 2005). Therefore to provide a shape-independent comparison of the red galaxy populations in the MACS and LARCS clusters we have measured the DGR on the red sequence (RDGR).

The boundary between giants and dwarfs is arbitrary and is usually defined as the magnitude where the faint-end Schechter function begins to dominate over the bright-end Gaussian (Goto et al., 2005). Looking at the distributions in Fig.3.4, we therefore choose an absolute magnitude of $M_V \sim -19.9$ at $z = 0.13$ as our dividing point. This absolute magnitude brightens to $M_V \sim -20.2$ at $z = 0.54$ as we take into account the passive evolution models of van Dokkum & Franx (2001) (we have confirmed that our results are not sensitive to applying this factor). To ensure that our measurements of the RDGR in the different samples are not effected by incompleteness we adopt the same faint-end limit as for fitting the luminosity functions ($M_V \sim -17.75$) and as in §3.3.2 we only consider galaxies within a 600 kpc radius of the centre of each cluster. The limits chosen for our RDGR analysis are comparable to those of De Lucia et al. (2004). We note that we see no trend between

Table 3.2: The best-fitting parameters for the luminosity function of red sequence galaxies for the MACS and LARCS clusters.

	χ^2/ν	Schechter			Gaussian[1]		
		α	M_V^*	ϕ^*	$\langle M_V \rangle$	σ_M	Amp.
LARCS	0.28	-1.11 ± 0.05	-21.10 ± 0.11	177.7 ± 22.2	...	...	...
	0.38	-0.92 ± 0.14	-19.43 ± 0.17	331.6 ± 57.2	-20.39 ± 0.12	0.89 ± 0.05	170.5 ± 21.8
MACS	1.29	-0.91 ± 0.02	-21.39 ± 0.05	215.1 ± 10.9	...	...	...
	1.14	-0.94 ± 0.19	-20.08 ± 0.67	223.0 ± 75.4	-20.86 ± 0.16	0.83 ± 0.08	177.2 ± 33.9

1) Where the Gaussian fit parameters are not given this is a purely Schechter function fit to the luminosity function.

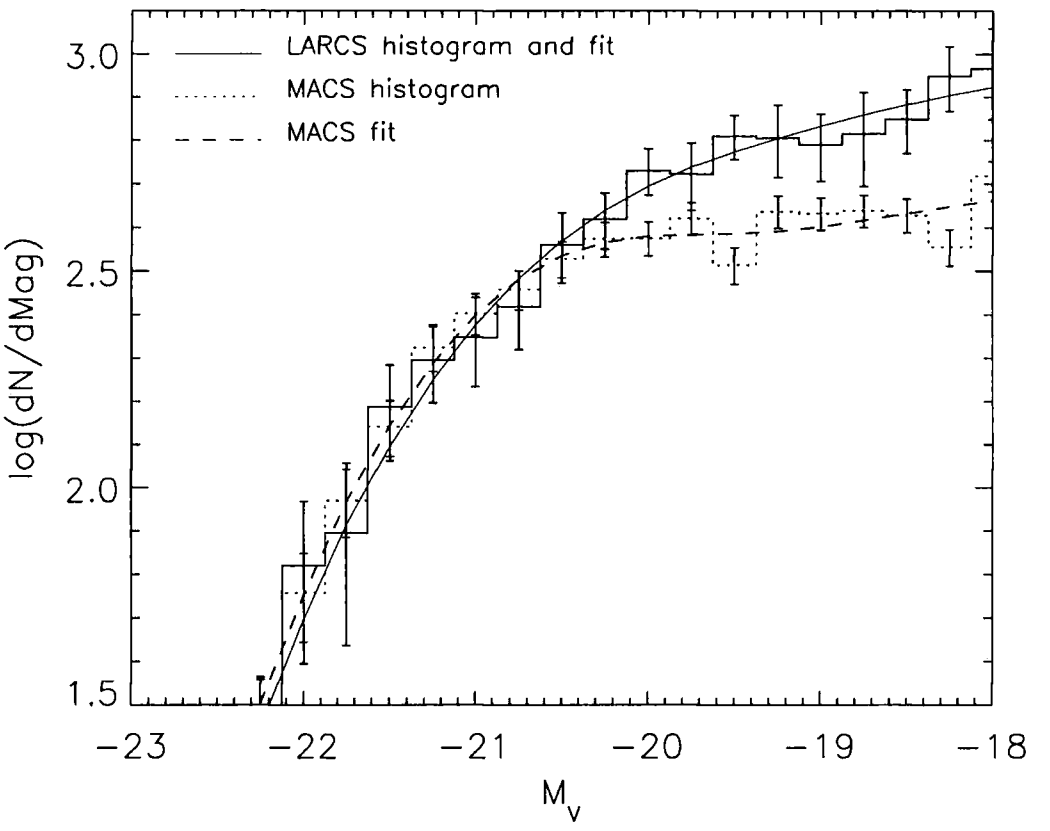

Figure 3.4: The luminosity functions in the restframe V-band for the red sequence galaxies in the combined MACS and LARCS samples (normalised to the bright-end of the LARCS sample). We plot the background-corrected data and our best-fit Gaussian+Schechter function fits. The errors are a combination of the Poisson uncertainty and the field correction error. Note the excess of faint red galaxies in the lower redshift LARCS sample, compared to the more distant MACS sample.

RDGR and cluster richness within the limited cluster mass range of our sample. Fig. 3.5 shows the variation of the RDGR with redshift. The RDGR increases with cosmic time and we attribute this to an increasing number of dwarfs on the red sequence. We determine weighted mean RDGRs for the MACS sample of 1.33 ± 0.06 and 2.93 ± 0.45 for LARCS, a difference of 3.7σ. This corresponds to an increase in RDGR of a factor of 2.2 ± 0.4 from $z = 0.54$ to $z = 0.13$, or a lookback interval of 4 Gyrs. An alternative way to look at this evolution is the variation in the proportion of integrated red light at the faint-end of the colour-magnitude relation, which increases by a factor of 1.46 ± 0.14 from $z = 0.54$ to $z = 0.13$. This means that the stellar mass in the passive dwarf population ($M_V \lesssim -20$) now almost equals that in luminous cluster galaxies, whereas at $z \sim 0.5$ the giants dominated the total V-band luminosity from galaxies on the colour-magnitude relation. The errors shown are a combination of the Poisson uncertainty and the field correction error.

We note that the LARCS RDGR errors are larger than those for MACS mainly due to the fact that at $z \sim 0.1$ the field galaxies and the faint end of the red sequence occupy the same region of $(B - R)$–R colour-magnitude space increasing the field correction error at the faint end (see Fig. 3.3). In contrast the faint red sequence in the MACS sample at $z \sim 0.5$ is much easier to distinguish from the field using V and I bands.

To parameterise the evolution in the RDGR we fit a $(1 + z)^{-\beta}$ power-law to the LARCS and MACS samples in Fig. 3.5. We see that this provides a good description of the evolution for $\beta = 2.5 \pm 0.5$, with all of the clusters consistent with the fit. This confirms that the luminosity function of the red sequence in the central regions of massive clusters appears uniform with no clear evidence from our study of real cluster-to-cluster variations although the errors on individual clusters are large. We also find that the six additional clusters and Coma (RDGR= 2.8 ± 1) follow the same trend defined by the MACS and LARCS samples. De Lucia et al. (2004), who use a similar definition of DGR, found a value of 1.23 for clusters at $z = 0.75$ and a value of 2.9 for Coma which are in good agreement with the trend we observe. The trend is also in qualitative agreement with the work of Kodama et al. (2004).

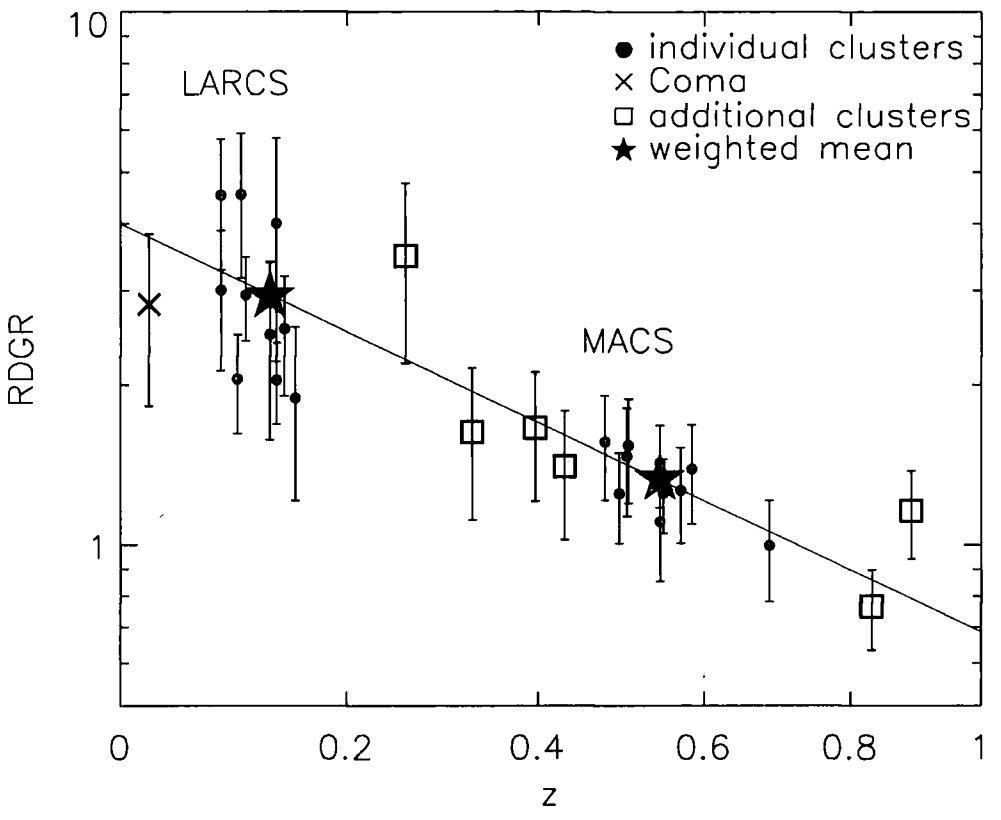

Figure 3.5: The variation in the red sequence Dwarf-Giant Ratio (RDGR) with redshift for clusters in our two samples within 600 kpc of the cluster centre and brighter than $M_V = -17.75$. We also plot the weighted mean values for each of the MACS and LARCS sample. A fit of the form $(1+z)^{-\beta}$ to the MACS and LARCS points is plotted and yields $\beta = 2.5 \pm 0.5$. For comparison we show the equivalent measures for six additional high redshift clusters and Coma (RDGR$= 2.8 \pm 1$), which follow the same trend.

3.4 Conclusions

Our analysis of the red galaxy populations in X-ray luminous clusters shows clear differences in the form of the luminosity function over the redshift range $z = 0.1$–0.5. These changes reflect an increase in the proportion of dwarf to giant galaxies in the population since $z \sim 0.5$ which we attribute to an increase in the number of dwarfs on the red sequence. We quantify this evolution using the shape independent estimate of the relative evolution of the faint end of the luminosity function, the red sequence Dwarf-Giant ratio (RDGR), which shows an increase by a factor of 2.2 ± 0.4 between $z = 0.54$ and $z = 0.13$. This is equivalent to an increase of 1.46 ± 0.14 in the relative V-band luminosity (or stellar mass) in faint red galaxies with $M_V \lesssim -20$ compared to brighter systems over this period. This increase means that in local clusters, the luminosity contributed by giant and dwarf galaxies is comparable, whereas at $z = 0.5$ the giants were the dominant population on the colour-magnitude relation. Our results show that there is significant evolution since $z \sim 0.5$ in the faint passive galaxy population in a well-defined sample of X-ray luminous clusters. This agrees with the early results from De Lucia et al. (2004) and Kodama et al. (2004) on red galaxies in a more diverse range of structures. However, this is in disagreement with the work of Andreon (2006) who sees no such evolution. This disagreement may be simply due to Andreon's use of a single cluster, as our analysis shows a large cluster to cluster scatter but with large errors (due to an uncertain field correction). We conclude that a large proportion of the passive galaxy population at the faint end of the colour-magnitude sequence in local clusters either did not reside in similar, high-density environments 5-Gyrs ago (at $z \sim 0.5$) or if they were present in these regions then they had significantly bluer colours (suggesting they were actively star forming) and so do not fall within the colour-magnitude relation.

Clusters in the mass range studied in this work are expected to have roughly doubled their masses since $z \sim 0.5$ (Tormen 1998) and hence many of the faint red galaxies (or at least their progenitors) may have arrived in the core regions of the cluster between $z \sim 0.5$ and $z \sim 0.1$. However, we believe that the major driver of the evolution we see is the transformation of blue, star-forming galaxies into passive, red systems which lie on the colour-magnitude relation. If correct, this suggests

that there will be an increasing diversity in the star formation histories of passive galaxies at $M_V \lesssim -20$ in intermediate redshift clusters (at $z \sim 0.3$–0.4), and studies of age-sensitive indicators at these depths may uncover evidence for recent star-formation activity within these galaxies (e.g. Smail et al. 2001).

We end by noting that studies such as this one can be extended to a wider range of environments and redshifts out to $z \sim 1$ using the data from current and future surveys such as the UKIRT Infrared Deep Sky Survey (UKIDSS, Lawrence et al. 2006) and the *XMM Newton* Cluster Survey (XCS, Romer et al. 2001). Such studies will allow the evolution of the passive population on the colour-magnitude relation and its build-up to be tracked as a function of environment and epoch and will demonstrate the importance of including environmental effects when modelling the colour-magnitude relation in galaxy evolution models.

Chapter 4

The slope of the cluster red sequence

Overview

Building on our work in chapter 3 we look to further investigate the properties of the cluster red sequence. Here we study the evolution of the red sequence slope in massive clusters from z=1 to present day. We confirm that this slope is comparable for clusters at similar redshifts. The slope is shown to increase with redshift due to the effects of K correction and the build up of the red sequence (chapter 3). Good agreement is found between our observed slope evolution and predicted slope evolution from semi-analytical models based on the Millennium simulation. This demonstrates that models that include feedback from active galactic nuclei are able to reproduce the observed cluster red sequence slope over the range of redshifts considered here. We observe no trend between the red sequence slope and the X-ray luminosity, velocity dispersion or the Brightest Cluster Galaxy dominance of the cluster. This suggests that the slope is unaffected by cluster environment at a given redshift therefore searching for clusters using the colour-magnitude relation is a robust approach (chapter 6).

4.1 Introduction

The cluster red sequence has a number of observable parameters that can be used in cluster evolution analysis. One such parameter is the slope of the sequence in colour-magnitude space. The origin of the slope has been controversial due to the age metallicity degeneracy for stellar populations. Worthey et al. (1995) showed that the sequence of colours that comprise the slope can be equally well explained by a progressive decrease in either metallicity or stellar age. The slope is now thought to be due to a mass-metallicity relation along the red sequence. Kodama & Arimoto (1997) broke this degeneracy by comparing colour-magnitude simulations to observations of distant clusters. The massive metal-rich galaxies appear progressively redder than their less massive counterparts. The origin of the mass-metallicity relation is the heating of the interstellar medium (ISM) by supernovae which triggers the formation of a galactic wind when the thermal energy of the gas exceeds the binding energy. This wind ejects gas more efficiently in smaller galaxies due to their shallower potential wells, resulting in the trend of increased metallicity with mass (Carlberg, 1984).

Clusters observed at similar redshifts are found to have comparable red sequence slopes (Lopez-Cruz, 1997). The slope is also shown to evolve with cosmic time (Gladders et al. 1998, Lopez-Cruz et al. 2004). The favoured explanation for this evolution is that this is a result of K correction and the mass metallicity relation in cluster ellipticals (Kodama & Arimoto 1997; Kauffmann & Charlot 1998). The build up of the red sequence may also contribute to this slope evolution (chapter 3, Stott et al. 2007). Faint galaxies falling into the cluster will appear bluer than the more massive metal-rich galaxies on the red sequence due to the mass-metallicity relation. With time these galaxies will become more metal-rich due to enrichment, decreasing the metallicity differential along the sequence. As the red sequence is found to be built up with progressively fainter galaxies this will contribute to the slope evolution causing an increased gradient at high redshift. There may also be an age contribution to the red sequence slope from recent star forming galaxies transforming onto the sequence at the faint end.

This change of slope with redshift has been used as a method to constrain cluster

evolution. Comparisons of the observed slope evolution to models conclude that the elliptical galaxies in cluster cores have been in place since at least $z = 2$ (Gladders et al., 1998). The reverse can also be achieved by using the colour and slope of the sequence to predict the redshift of a cluster. This is found to be in good agreement with spectroscopic redshifts and can therefore be used as an effective two waveband photometric redshift. This technique is important for current and future large area photometric surveys which hope to study cluster abundance (e.g. RCS, Gladders & Yee (2000); Pan-STARSS; SDSS, Adelman-McCarthy et al. 2006; UKIDSS, Lawrence et al. 2006).

In this work we will investigate the red sequence slope evolution in both optical (V-I/I) and near infrared (J-K/K) bands for a homogeneous sample of X-ray selected galaxy clusters in the range z ~0–1. This is the most comprehensive study of the red sequence slope undertaken thus far. We compare our findings with latest synthetic slopes calculated from analysis of the semi-analytical model of Bower et al. (2006) based on the Millennium N-body simulation (Springel et al., 2005). This model includes feedback from active galactic nuclei (AGN) which has both a radiative and mechanical effect on star formation. Emission from AGN causes the heating of the ISM so it cannot condense to form stars whereas the wind and jet mechanisms destroy the ISM physically removing the fuel to make new stars. This quenches star formation in massive halos to match the observed break in the luminosity function seen at bright magnitudes. We move on to look for trends in red sequence slope with other observables such as X-ray luminosity, velocity dispersion and brightest cluster galaxy (BCG) dominance.

4.2 Observations and Reduction

To observe the evolution of the red sequence we study X-ray selected clusters in the range z =0–1 in both near-infrared and optical bands. The clusters all have X-ray luminosities in excess of 10^{44}erg s^{-1} (0.1 – 2.4 keV). As discussed in chapter 2, the motivation for studying an X-ray selected sample is to ensure that we are observing objects in comparable high mass environments.

For the sample to span such a large range in redshift we need to study cluster data from different surveys and instruments.

The sample of the 34 optically observed (V and I or B and R bands) clusters used in our analysis is presented in table 4.1. The clusters belong to the following surveys: the MAssive Cluster Survey (MACS, Ebeling et al. 2001); the Las Campanas/AAT Rich Cluster Survey (LARCS, Pimbblet et al. 2001, 2006) and archival *Hubble Space Telescope* (*HST*) data. The observations were taken with the instruments: the Advanced Camera for Surveys (ACS) and the Wide Field Planetary Camera (WFPC) on *HST* and the 1m Swope telescope. For a more detailed description of the data and reduction see chapter 3 (MACS) and Pimbblet et al. (2001) (LARCS).

The $z \sim 0.2$ Abell clusters were observed in the B and R bands with the CFH12k camera on 3.6m Canada France Hawaii Telescope. Details of the data and reduction can be found in Smith et al. (2001) and Bardeau et al. (2005).

The 27 clusters studied in the near-infrared (J and K band) are displayed in table 4.2. The clusters belong to the following surveys: The *ROentgen SATellite* (*ROSAT*) Brightest Cluster Survey (BCS) and extended BCS (Ebeling et al., 1998), the X-ray Brightest Abell Clusters Survey (XBACS, Ebeling et al. 1996) and the MACS survey (Ebeling et al., 2001). The observations were taken with the instruments: the Wide field InfraRed Camera (WIRC) instrument on the Palomar 200" Hale telescope and the Infrared Spectrometer And Array Camera (ISAAC) on the Very Large Telescope (VLT). An additional low redshift data point is included for the Coma Cluster which we source from a combination of the Two Micron All Sky Survey (2MASS) extended and point source catalogues (Skrutskie et al., 2006). For a more detailed description of the data and reduction see chapter 2.

We include a high redshift cluster (ClJ1226.9+3332, $z \sim 0.9$) from the Wide Angle *ROSAT* Pointed Surveys (WARPS, Scharf et al. 1997, Jones et al. 1998). This X-ray selected cluster was observed in the J and K bands using the UFTI camera on UKIRT (Ellis & Jones, 2004).

The colour (V-I, B-R and J-K) photometry extracted for the clusters employs 9kpc apertures for colours and the magnitude used is SExtractor's 'Best' magnitude (Bertin & Arnouts, 1996). The SExtractor colour photometry was run in dual

mode with the 9kpc 'red'-band (R, I, K) apertures used to extract the corresponding 'blue'-band (B, V, J) photometry. This is to ensure the same size aperture for both bands which is important for good colour determination. We only consider within 600kpc radius of the cluster centre, to limit contamination from field galaxies. For all of our observations we reach a depth which allows us to see to at least 4 magnitudes fainter than the BCG and thus perform a reliable fit to the slope.

4.3 Analysis and Results

4.3.1 Fitting red sequence the slope

Fig. 4.1 is an example of the prominent red sequences we see in the rich clusters of our sample. To fit the slope of the red sequence we need to use a robust and consistent method. We therefore employ the same technique as described in Gladders et al. (1998), an iterated 3 σ clipped fit. The fit is performed as follows: first we set a limiting magnitude for the red sequence which corresponds to the mean of the next 2 brightest galaxies down from the BCG magnitude+3. The reason for this is that in some cases there can be a large luminosity gap ($\sim$1 mag) between the BCG and the start of the red sequence so this ensures we measure the slope without this gap (chapter 2). We then select the region of colour magnitude space containing the red sequence and estimate an initial fit from visual inspection. The residuals about this estimate are calculated and a Gaussian is fitted to the resulting colour distribution with the slope removed. The peak of this Gaussian corresponds to the red sequence. We then perform a fit to points that are within 3 sigma of this fit. This is a two parameter linear fit of the form $y = \kappa x + c$ where κ is the slope of the red sequence. The process is iterated until it converges to a solution. We confirm the work of Gladders et al. (1998) that this is a robust method for reasonable choices of limiting magnitude and initial fit.

It should be noted that our colour-magnitude diagrams are not field corrected. At the colours and magnitudes we consider this a very small contribution to the red sequence, typically 5% contamination for $z \gtrsim 0.2$ clusters and 10% for the $z \sim 0.1$ clusters. We perform a statistical field correction test to a sub-sample of our low

Table 4.1: Details of the optical cluster samples used in our analysis.

Cluster	R.A. (J2000)	Dec.	z	L_X (10^{44}erg s^{-1})	κ_{VI}
LARCS $z \sim 0.1$ Sample					
Abell 22	00 20 38.64	−25 43 19	0.142	5.3	-0.042 ±0.012
Abell 550	05 52 51.84	−21 03 54	0.099	7.1	-0.028 ±0.011
Abell 1084	10 44 30.72	−07 05 02	0.132	7.4	-0.027 ±0.013
Abell 1285	11 30 20.64	−14 34 30	0.106	5.45	-0.014 ±0.014
Abell 1437	12 00 25.44	+03 21 04	0.134	7.7	-0.008 ±0.014
Abell 1650	12 58 41.76	−01 45 22	0.084	7.8	-0.015 ±0.010
Abell 1651	12 59 24.00	−04 11 20	0.085	8.3	-0.019 ±0.009
Abell 1664	13 03 44.16	−24 15 22	0.128	5.34	-0.026 ±0.017
Abell 2055	15 18 41.28	+06 12 40	0.102	4.8	-0.021 ±0.009
Abell 3888	22 34 32.88	−37 43 59	0.153	14.5	-0.025 ±0.031
MACS $z = 0.4$–0.7 Sample					
MACS J0025.4−1222	00 25 15.84	−12 19 44	0.478	12.4	-0.123 ±0.021
MACS J0257.6−2209	02 57 07.96	−23 26 08	0.504	15.4	-0.101 ±0.016
MACS J0451.9+0006	04 51 54.63	+00 06 18	0.430	10.4	-0.054 ±0.005
MACS J0647.7+7015	06 47 51.45	+70 15 04	0.584	21.7	-0.064 ±0.020
MACS J0712.3+5931	07 12 20.45	+59 32 20	0.328	6.8	-0.051 ±0.006
MACS J0717.5+3745	07 17 31.83	+37 45 05	0.548	27.4	-0.107 ±0.012
MACS J0744.8+3927	07 44 51.98	+39 27 35	0.686	25.9	-0.129 ±0.019
MACS J0911.2+1746	09 11 10.23	+17 46 38	0.506	13.2	-0.078 ±0.014
MACS J1149.5+2223	11 49 34.81	+22 24 13	0.544	17.3	-0.092 ±0.017
MACS J1354.6+7715	13 54 19.71	+77 15 26	0.397	8.2	-0.053 ±0.013
MACS J1423.8+2404	14 23 47.95	+24 04 59	0.544	15.0	-0.080 ±0.015
MACS J2129.4−0741	21 29 25.38	−07 41 26	0.570	16.4	-0.082 ±0.023
MACS J2214.9−1359	22 14 56.51	−14 00 17	0.495	17.0	-0.093 ±0.013
Additional *HST* archival clusters					
Cl J0152−1357	01 52 43.91	−13 57 21	0.831	5.0	-0.102 ±0.022
Cl J1226.9+3332	12 26 58.13	+33 32 49	0.890	20.0	-0.085 ±0.014
Abell 1703	13 15 00.70	+51 49 10	0.258	8.7	-0.059 ±0.011

The LARCS redshifts are from Pimbblet et al. (2006). MACS redshifts come from Ebeling et al. (2007).

Table 4.2: Details of the near-infrared cluster sample used in our analysis. Data reduction information can be found in chapter 2.

Cluster	R.A.	Dec.	z	L_X	κ_{JK}
	(J2000)			(10^{44}erg s^{-1})	
Abell 115	00:56:00.24	+26:20:31.7	0.197	14.59	-0.031 ±0.006
Abell 1201	11:12:54.50	+13:26:08.9	0.169	6.28	-0.013 ±0.007
Abell 1246	11:23:58.75	+21:28:47.3	0.190	7.62	-0.031 ±0.008
Abell 1758	13:32:38.59	+50:33:38.7	0.279	11.68	-0.027 ±0.011
Abell 1763	13:35:20.14	+41:00:03.8	0.223	14.93	-0.029 ±0.010
Abell 1914	14:25:56.64	+37:48:59.4	0.171	18.39	-0.021 ±0.006
Abell 209	01:31:52.51	-13:36:41.0	0.209	13.75	-0.022 ±0.009
Abell 2111	15:39:41.81	+34:24:43.3	0.229	10.94	-0.033 ±0.012
Abell 2163	16:15:33.57	-06:09:16.8	0.203	37.50	-0.022 ±0.006
Abell 2218	16:35:49.39	+66:12:45.1	0.176	9.30	-0.025 ±0.007
Abell 2445	22:26:55.80	+25:50:09.4	0.165	4.00	-0.027 ±0.009
Abell 291	02:01:46.80	-02:11:56.9	0.196	4.24	-0.024 ±0.009
Abell 665	08:30:57.34	+65:50:31.4	0.182	16.33	-0.020 ±0.008
Abell 773	09:17:53.57	+51:44:02.5	0.217	13.08	-0.033 ±0.006
Cl J1226.9+3332	12 26 58.13	+33 32 49	0.890	20.0	-0.088 ±0.010
Coma Cluster	12:59:48.70	27:58:50.0	0.0231	7.26	-0.017 ±0.009
MACS J0018.5+1626	00:18:33.68	+16:26:15.1	0.541	18.74	-0.048 ±0.009
MACS J0025.4-1222	00:25:27.44	-12:22:28.3	0.478	12.40	-0.047 ±0.010
MACS J0257.6-2209	02:57:09.78	-23:26:09.8	0.504	15.40	-0.065 ±0.012
MACS J0454.1-0300	04:54:11.13	-03:00:53.8	0.550	16.86	-0.040 ±0.009
MACS J1359.8+6231	13:59:54.32	+62:30:36.3	0.330	8.83	-0.039 ±0.007
MACS J2129.4-0741	21:29:26.35	-07:41:33.5	0.570	16.40	-0.068 ±0.009
MACS J2214.9-1359	22:14:56.51	14:00:17.2	0.495	17.00	-0.035 ±0.014
MS1054-0321	10:57:00.20	-03:37:27.4	0.830	23.30	-0.073 ±0.011
RCS0224-0002	02:24:00.00	-0:02:00.0	0.770	0.70	-0.055 ±0.020
RX J1720.1+2638	17:20:10.08	+26:37:33.5	0.164	6.66	-0.023 ±0.007
Zw 1432	07:51:25.15	+17:30:51.8	0.186	5.27	-0.022 ±0.010

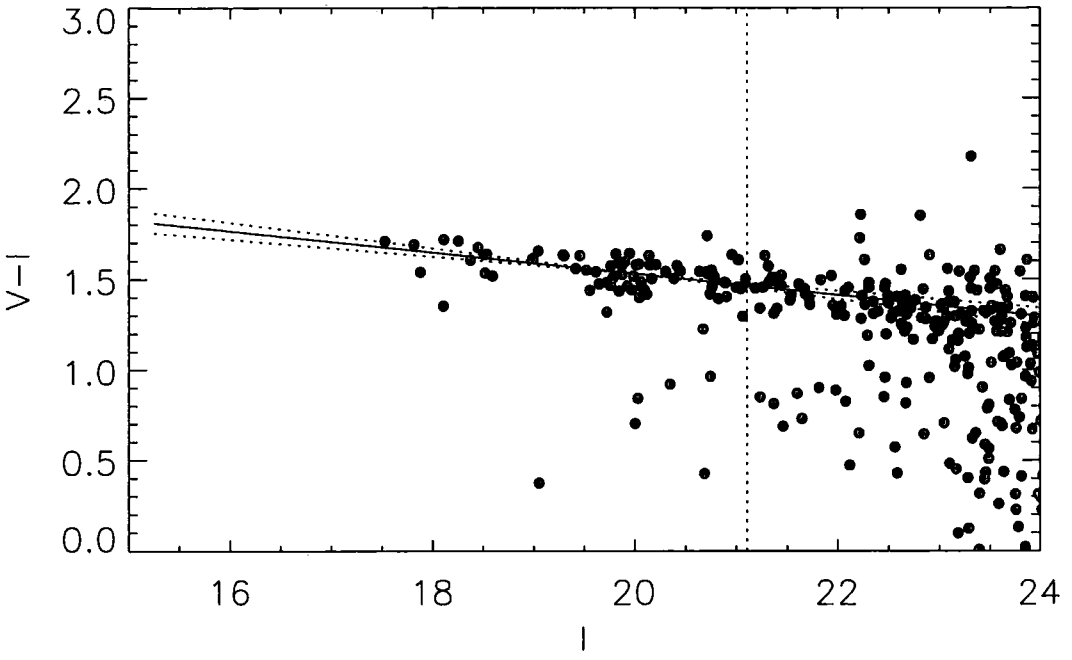

Figure 4.1: The V-I vs I colour-magnitude diagram for the cluster Abell 1703. The slope fit, 1σ fit errors and limiting magnitude are included

z clusters and find that the slope of the sequence varies randomly by less than 1σ than that obtained for the uncorrected sequence. We therefore feel justified in not applying this correction. For details of the statistical field correction technique used see chapter 3.

4.3.2 Slope evolution

Fig. 4.2 displays the observed red sequence slope evolution for our near infrared sample. This slope (κ_{JK}) is shown to steepen with redshift. This steepening will have contributions from both K correction and the build up of the red sequence. The contribution from K correction is due to the observed J and K bands sampling increasingly bluer rest wavebands at higher redshift (Gladders et al., 1998). The red sequence build up causes the faint end of the red sequence to be bluer compared

to the bright end at high redshift as it is populated with less metal-rich galaxies. The metallicity differential along the red sequence decreases with age as the galaxies mature.

We include a slope evolution model on Fig.4.2 which is calculated by analysing the semi-analytical model of Bower et al. (2006) based on the Millennium N-body simulation (Springel et al., 2005). We access these data online through Virgo Millennium Database. The Bower et al. (2006) model accounts for the recent observations that the stellar mass in bright galaxies was in place at high redshift by including feedback from active galactic nuclei. We model the red sequence slope evolution by creating colour magnitude diagrams from the Bower et al. (2006) model output at a distinct set of redshift intervals between z=0 and z=1. For the creation of these colour-magnitude diagrams we ensure we only study the passive red sequence galaxies by selecting galaxies with no star formation (L(Hα) =0). We also select only those galaxies in dark matter halos more massive than the mean halo mass at their corresponding redshift ($4.5 \times 10^{12} M_{\odot}$ at z =0) to select galaxies in overdense regions for comparison with our cluster environments while maintaining good statistics at high redshift. We calculate the model for the slope evolution by fitting the synthetic red sequence slopes at each redshift interval with the method described in §4.3.1. As with the observations, the model slope is shown to steepen with redshift. The model is normalised to our low redshift data. When the model is plotted with our complete near-infrared dataset in Fig.4.2 we find good qualitative agreement between the two. The rms scatter about the model is 0.0087. The supposition that the metallicity differential along the sequence decreases with redshift is borne out in the models as the gradient at z =0 is -0.0029±0.0004 $Z_{\odot}$ mag^{-1} and at z=1 it is -0.061±0.009 $Z_{\odot}$ mag^{-1}.

We now look to the slope evolution for our optical observations. As above, the simulated slope evolution plotted is calculated from semi-analytical model of Bower et al. (2006). There is an additional complication as our optical data are sourced from two different filter sets so we have to account for the observed difference in red sequence slope between them. To achieve this we normalise all data to the $V-I/I$ filters by correcting for the difference between the $V-I/I$ model and the model

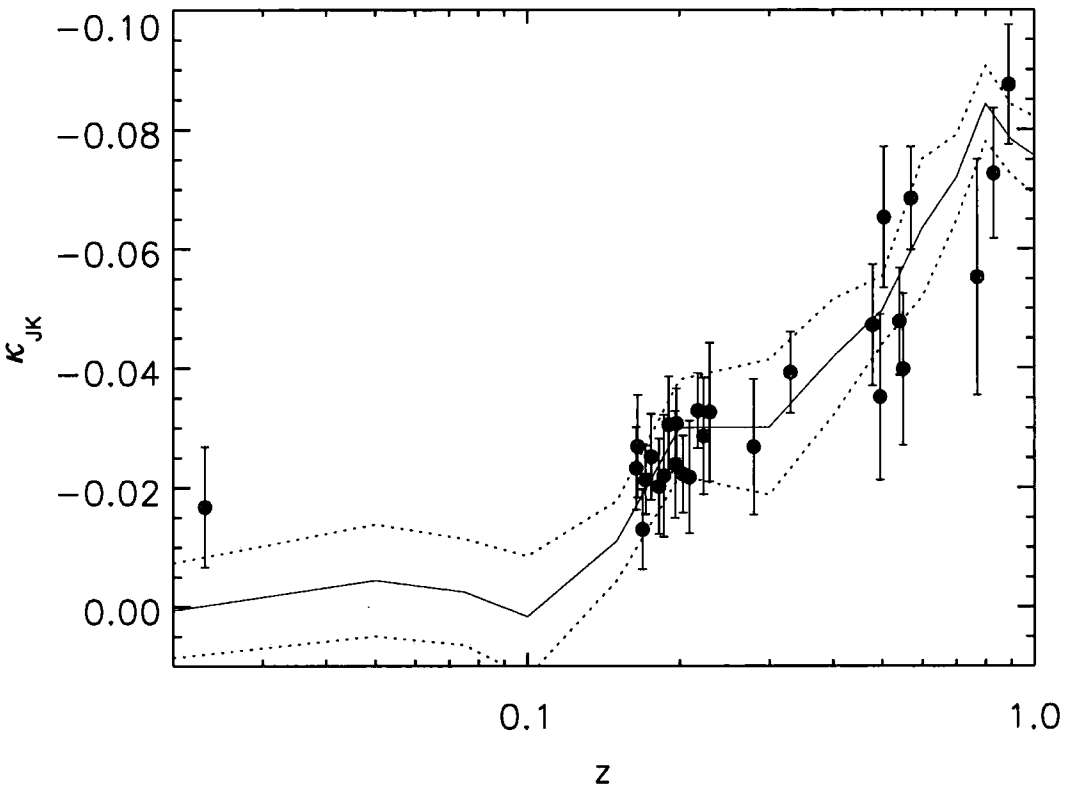

Figure 4.2: The evolution of the red sequence slope (κ_{JK}) for our near-infrared sample. A model calculated from Bower et al. (2006) is included for comparison with theory. Solid line: model. Dotted line: 1 σ error on model.

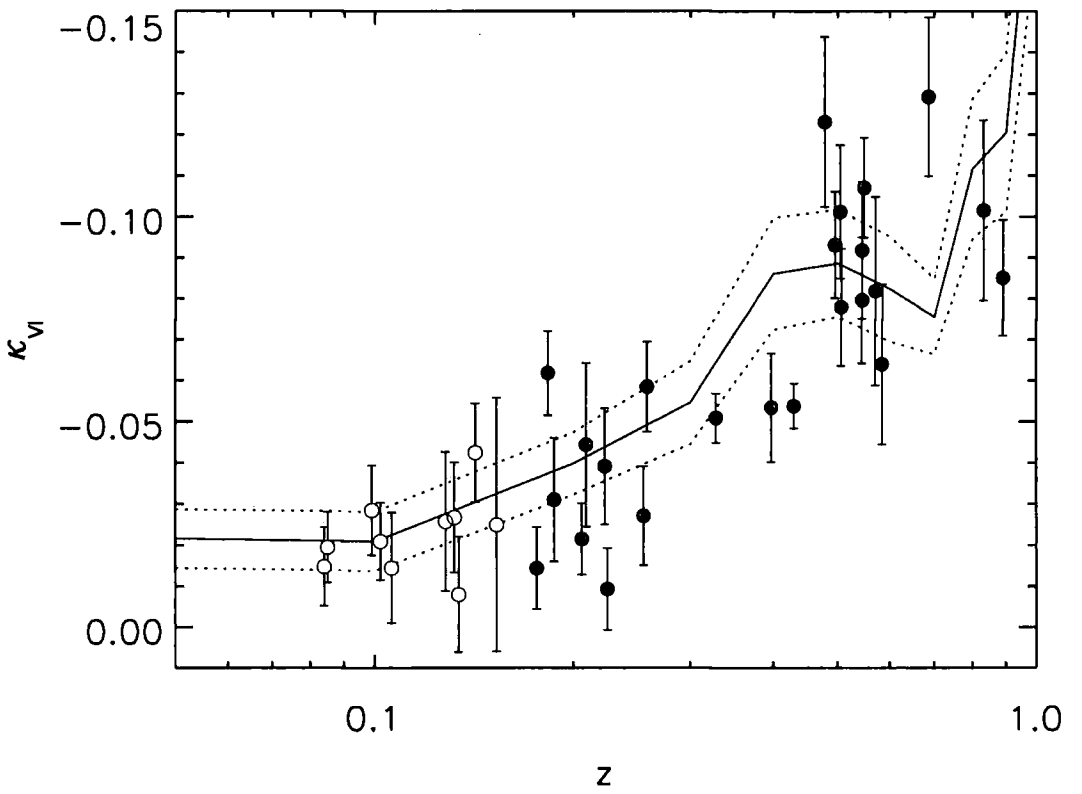

Figure 4.3: The evolution of the red sequence slope (κ_{VI}) for our optical sample. The open circles represent the κ_{VI} values calculated from the $B - R$ vs R colour magnitude relations. The model again comes from analysis of Bower et al. (2006). Solid line: model. Dotted line: 1 σ error on model.

for the $B - R/R$ filter combination (as in Gladders et al. 1998). The resultant data-points and model are plotted in Fig. 4.3. The slope is shown to increase with redshift in-line with K correction and red sequence build up. The rms scatter about the model is 0.019. As with the near-infrared observations we find good agreement between the model and the data.

4.3.3 Evolution with other observables

We now investigate whether there are further trends in red sequence slope with other observable cluster properties. The most obvious of these being the X-ray luminosity, which is a proxy for mass in a relaxed system. In Figs 4.4 and 4.5 we plot the residual values of the slope about the model lines in Figs 4.2 and 4.3 against L_X. From this we see no obvious trend between scatter about the model and L_X. In Fig. 4.6 (*right*) we also show that there is no trend between red sequence slope and another mass proxy, the cluster velocity dispersion, σ.

In addition to the X-ray luminosity and σ, we can look to the degree of BCG dominance as an indicator of the local environment within the cluster core (discussed in chapter 2). This parameterises the luminosity gap between the BCG and the next brightest galaxies on the red sequence and is defined as $\Delta m_{1-2,3} = (m_2+m_3)/2-m_1$ where m_1 is the magnitude of the BCG and m_2 and m_3 are the magnitudes of the 2nd and 3rd brightest members respectively (Kim et al., 2002). In Fig. 4.7 we demonstrate that there is no trend between red sequence slope and the degree of BCG dominance.

The above results suggest that different cluster environments do not have a noticeable effect on the near-infrared or optical red sequence slope at a given redshift. Previous studies within a similar L_X range have also seen homogeneity in other related cluster properties such as the shape of the luminosity function and the blue galaxy fraction (de Propris et al. 1999; Wake et al. 2005). This means that the scatter observed in the slope evolution is most likely intrinsic. We can therefore also state that even in a homogeneous X-ray sample there are real cluster to cluster variations in red sequence slope which are probably driven by local processes with no clear link to the global properties we observe.

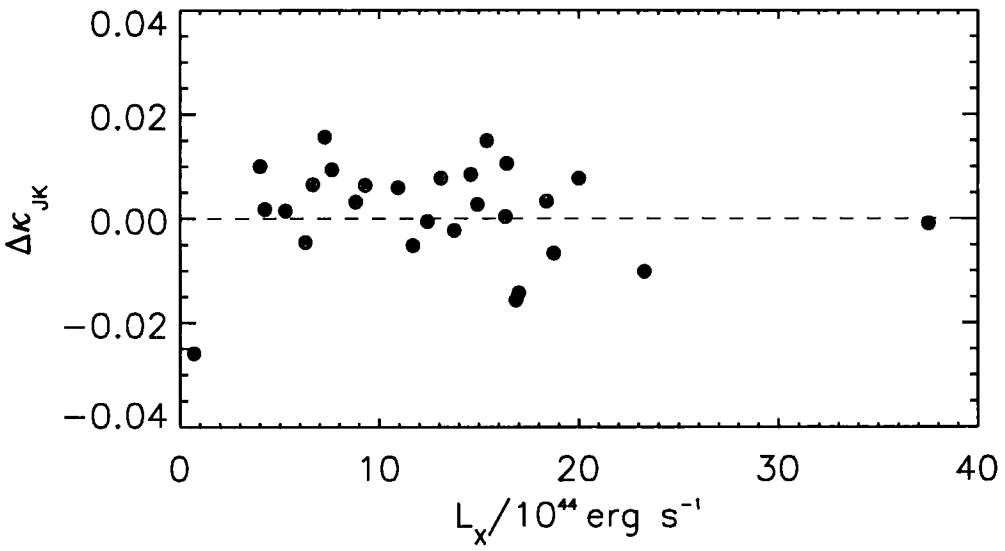

Figure 4.4: The residuals about the models in Fig. 4.3 plotted against X-ray luminosity. The correlation coefficient, r, for this plot is -0.06 meaning there is no correlation.

4.4 Summary

We have shown the cluster red sequence slope evolves with redshift for our optical and near infrared observations as seen in previous studies (Gladders et al. 1998, Lopez-Cruz et al. 2004).

The observed slope evolution agrees with that expected from the build up of the red sequence. This causes the faint end of the red sequence to be bluer compared to the bright end at high redshift as it is populated with less metal-rich galaxies. The metallicity differential along the red sequence decreases with age as the galaxies mature. As the red sequence is built up with progressively fainter galaxies this contributes to the slope evolution causing an increased gradient at high redshift. There may also be an age contribution to the slope from recent star forming galaxies transforming onto the sequence at the faint end.

We find our data to be in good agreement with slope evolution models we calculate from semi-analytical model of Bower et al. (2006) based on the Millennium N-body

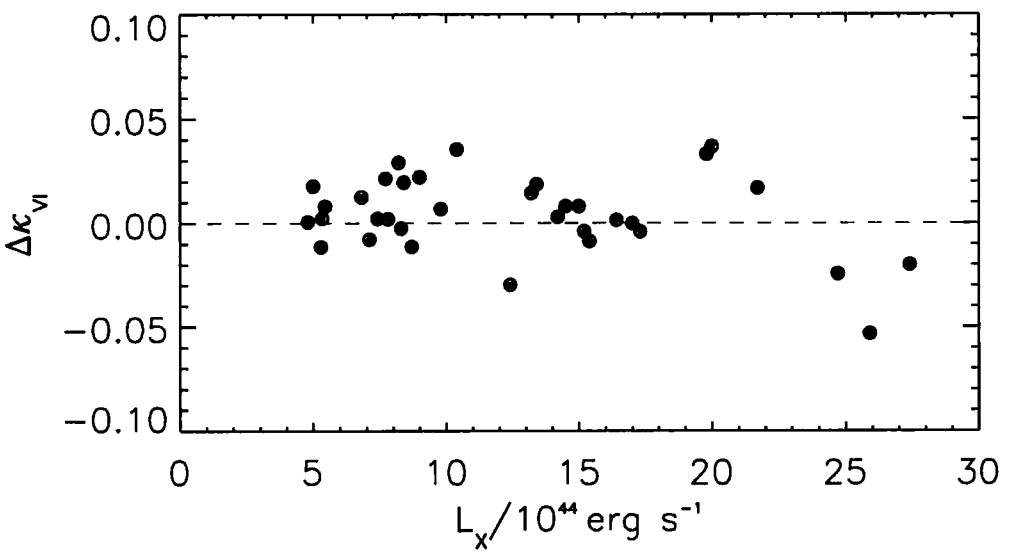

Figure 4.5: The residuals about the models in Fig. 4.2 plotted against X-ray luminosity. The correlation coefficient, r, for this plot is -0.31 meaning there is a weak negative correlation.

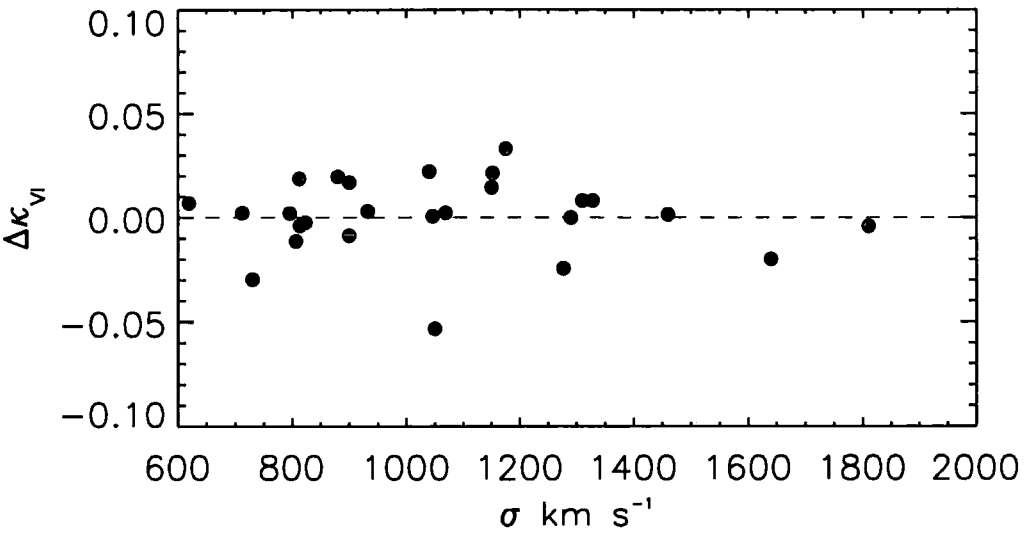

Figure 4.6: The residuals about the models in Fig. 4.3 plotted against velocity dispersion, σ. The correlation coefficient, r, for this plot is -0.05 meaning there is no correlation.

simulation (Springel et al., 2005). This demonstrates that such models that include feedback from active galactic nuclei are able to reproduce the observed cluster red sequence slope over the range of redshifts $0< z <1$.

When looking at slope trends with other observables we see no relationship between cluster slope and X-ray luminosity, velocity dispersion or BCG degree of dominance. This suggests that there is very little variation between the red sequence slopes due to the different cluster environments we consider. This implies that searching for massive clusters using the colour magnitude relation (CMR) is a viable method (Chapter 6, Barkhouse et al. 2006).

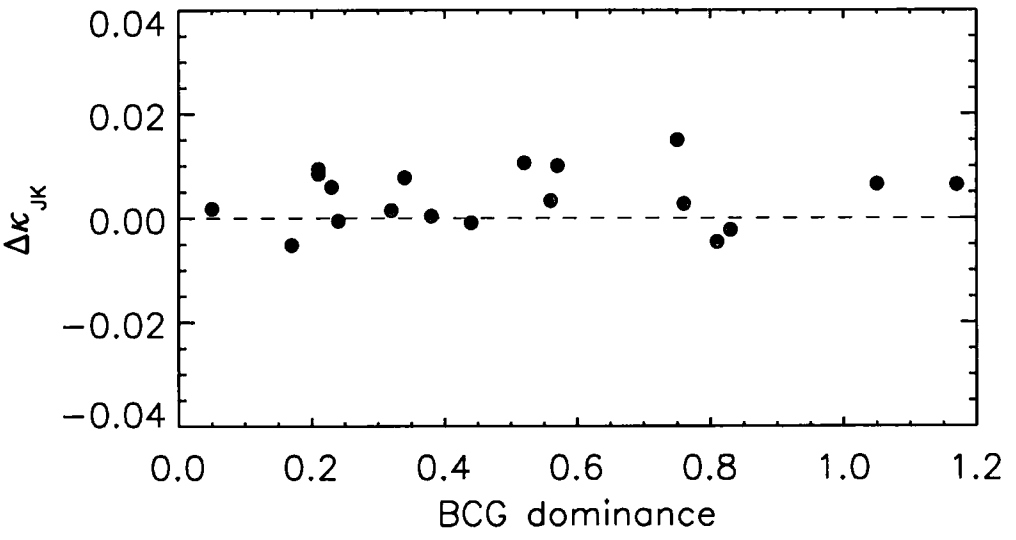

Figure 4.7: The residuals about the models in Fig. 4.2 plotted against BCG dominance. The correlation coefficient, r, for this plot is 0.12 meaning there is no correlation.

Chapter 5

UKIDSS

Overview

This chapter describes the UKIRT Infrared Deep Sky Survey (UKIDSS), a near-infrared survey of the northern sky. The main focus is on the Deep Extragalactic Survey (DXS), a sub-survey of UKIDSS which will reach a depth of J=22.3 and K=20.8 mag over 35 square degrees on completion. We provide the technical specifications of the UKIDSS survey instrument, WFCAM on UKIRT, to illustrate how the survey tiles are mosaiced on the sky. A brief description of data quality checks and examples of issues with the WFCAM output are then presented. Following this is a detailed account of image processing, mosaic creation and the extraction of independent object catalogues for the UKIDSS DXS. We then perform basic analysis on these catalogues with the creation of colour-magnitude diagrams and source counts for the individual DXS regions. This work forms the basis for the cluster selection analysis in chapter 6.

5.1 Introduction

Near-infrared (NIR) observations are an extremely useful tool for modern astronomers. The NIR window is used to study objects as diverse as luminous high redshift quasars to cool nearby objects such as brown dwarfs. This region of the electromagnetic spectrum is particularly attractive for extragalactic research for a number of reasons: 1) Extinction by dust is much less significant than at optical wavelengths; 2) The K correction is relatively small and insensitive to spectral type; 3) NIR observations of $z \gtrsim 1$ objects sample rest frame optical wavelengths allowing direct comparison with local surveys such as SDSS.

The first significant large area NIR survey was The Two Micron Sky Survey (TMSS, Neugebauer & Leighton 1969) which covered 70% of the sky and discovered ~6000 sources. With the advent of large, modern NIR detectors, it is possible to observe this region of the spectrum with greater depth and precision. The largest and most successful NIR survey to date is the Two Micron All Sky Survey (2MASS, Skrutskie et al. 2006) which has surveyed the entire sky to a depth of K=14.3 mag. The other major survey of recent years is the Deep Near Infrared Survey of the Southern Sky (DENIS, Epchtein et al. 1994) which achieves a ~2 mag greater depth than 2MASS for the southern hemisphere. Both of these surveys have made a significant impact on modern astronomy. The discovery of cool L and T dwarf stars and galaxies in the plane of the Milky Way would not have been possible without them. The next planned southern sky NIR survey will be performed with the Visible and Infrared Survey Telescope for Astronomy (VISTA) which has a large field of view and will observe to an even greater depth.

The UKIRT Infrared Deep Sky Survey (UKIDSS, Lawrence et al. 2006) is a near-infrared sky survey which began in May 2005. Once completed it will cover approximately 7000 square degrees of the northern sky. The UKIDSS survey makes use of the Wide Field Camera (WFCAM) on the 3.8m United Kingdom Infrared Telescope (UKIRT). The UKIDSS project is made up of five sub-surveys: the Large Area Survey (LAS), Galactic Plane Survey (GPS), Galactic Clusters Survey (GCS), Deep Extragalactic Survey (DXS) and Ultra Deep Survey (UDS). Each has been designed to achieve a specific set of science goals, from studying objects in the Galaxy to deep

Name	*Area* *sq. deg.*	*5 σ K band depth*
Large Area Survey (LAS)	4000 sq. degs	K=18.2
Galactic Plane Survey (GPS)	1800 sq. degs	K=18.8
Galactic Clusters Survey (GCS)	1400 sq. degs	K=18.6
Deep Extragalactic Survey (DXS)	35 sq. degs	K=20.8
Ultra Deep Survey (UDS)	0.77 sq. degs	K=22.8

Table 5.1: The five UKIDSS sub-surveys.

imaging of the early Universe. The principal targets of UKIDSS are: the coolest and nearest brown dwarfs, high-redshift dusty starburst galaxies, elliptical galaxies and galaxy clusters at redshifts 1<z<2 and the highest-redshift quasars at z ~7. Table 5.1 and Fig. 5.1 give a brief overview of the five surveys and their positions on the sky. The surveys include imaging for up to five filters, $ZYJHK$.

The UKIDSS LAS was designed to match the sky coverage of the Sloan Digital Sky Survey (SDSS, Strauss et al. 2002). The combination of the LAS, GCS and GPS form a natural successor to 2MASS and at a depth of K~18 are over three magnitudes deeper. This will also be the northern hemisphere counterpart to the VISTA survey which, when combined, will form an 'all sky' survey.

UKIDSS data are made available to members of the European Southern Observatory (ESO) community online and then to the wider world through the WFCAM Science Archive (WSA, http://surveys.roe.ac.uk/wsa/).

5.2 UKIDSS DXS

Our work concentrates on data from the UKIDSS Deep eXtragalactic Survey (DXS, Survey Head: Alastair Edge). This survey, in both J and K bands, will eventually achieve a 5 sigma point source depth of J =22.3 and K =20.8 over a 35 square degree area. The DXS itself is split into four high Galactic latitude regions of ~9 square degrees each (see table 5.2 and Fig. 5.1).

The primary aim of the DXS is to create a photometric galaxy sample at z =1-2

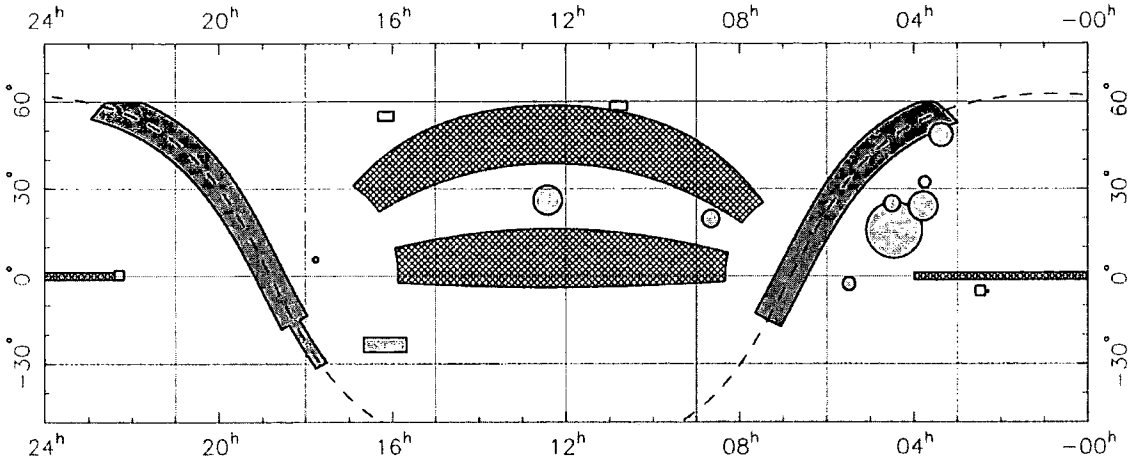

Figure 5.1: The positions of the five UKIDSS surveys in R.A. and Dec. Cross-hatch: Large Area Survey. Grey circles: Galactic Clusters Survey. Open rectangles: Deep Extragalactic Survey (note: the Ultra Deep Survey lies just west of the DXS field at 02h18m -05deg.) The Dashed line marks the Galactic plane. (Lawrence et al., 2006)

within a volume comparable to the Sloan Digital Sky Survey (SDSS, Strauss et al. 2002). The DXS will sample the rest frame optical, allowing a direct comparison with the SDSS. The principal science goals of the DXS are 1: to measure the abundance of galaxy clusters at $1< z <1.5$ in order to obtain constraints on cosmological parameters, 2: to measure galaxy clustering and bias at z>1 to test hierarchical models, 3: a multi-wavelength census of the luminosity density in star formation and active galactic nuclei (AGN). The science goals are described in detail on the DXS science case webpage (http://www.ukidss.org/sciencecase/sciencecase.html). We initially performed data quality analysis on the early DXS frames and catalogues (see §5.4). However, with the first major data release DR1 and now DR2 we have been able to perform more detailed, scientific analysis (see §5.6 and §5.7 and Chapter 6 for details). The majority of this work has been to search for high redshift clusters in two of the DXS regions. This has so far resulted in the discovery of a spectroscopically confirmed $z \sim 1$ supercluster (chapter 6, Swinbank et al. 2007).

Region	*Area*	*RA*	*DEC*
	sq. deg.	*J2000*	
XMM-LSS	8.75	02 25 00	−04 30 00
Lockman Hole	8.75	10 57 00	+57 40 00
Elais N1	8.75	16 10 00	+54 00 00
SA22	8.75	22 17 00	+00 20 00

Table 5.2: The four UKIDSS DXS fields.

5.3 WFCAM

The UKIDSS survey is only possible due to the technological advance offered by the WFCAM instrument on UKIRT, currently the most advanced NIR imaging survey instrument available. The focal plane layout of WFCAM is shown in figure 5.2. WFCAM consists of 4 detectors in a square, each separated by a gap comparable in size to a single detector, with a central autoguider. Each detector is a Rockwell Hawaii II 2048 × 2048 PACE HgCdTe array, with pixel size 0.4 arcsec. The autoguider is an optical CCD detector whose function is to track specific guide stars in the field of view to ensure accurate telescope pointing.

The layout of the detectors results in a WFCAM observation consisting of an image from each of its 4 detectors (each detector is 14 × 14 arcmin) in a square separated by a roughly detector sized gap (see figure 5.3, left). We describe such single pointings as a WFCAM 'footprint'. To make a contiguous, mosaiced image four of these WFCAM footprints are tiled to make a 4 detector × 4 detector image (see figure 5.3, right). This 16 detector square mosaic has dimensions 52 × 52 arcmin.

In addition to this tiling the UKIDSS DXS WFCAM images incorporate 'microstepping' which is a small dither pattern in the observation. The purpose of this process is to improve the point spread function sampling of the observations as the 0.4″ pixel size of WFCAM is comparable to the best atmospheric seeing. The DXS microstepping is performed by observing 4 footprint images each offset from each other by a whole number of pixels and a 1/2 pixel in a 2 × 2 grid pattern. These images are then coadded together with the fractional offsets taken into account so that the

resulting image has double the spatial sampling. Therefore, four microstep frames with an original resolution of 0.4 ″/pixel and size 2048 × 2048 pixels are converted to a higher resolution 0.2 ″/pixel 4096 × 4096 image. A full 16 detector mosaic image is therefore ∼16000 × 16000 pixels in size.

5.4 Data Quality

We have undertaken a number of data quality tests on the UKIDSS DXS data releases (Early Data Release, EDR and Data Release 1, DR1). This was done by simply visually inspecting the individual frames in the WSA archive. There are a number of data quality issues associated with some or all of the frames.

The most obvious problem, which occurs in all frames with a bright star present, is that of cross-talk which is an artifact of the detector electronics. This manifests itself as a signal on the image at multiples of 128 pixels away from a bright star in the detector read out direction. Unfortunately this type of artifact is not removed by stacking dithered images as it is always in the same position relative to the host star. For bright stars the cross-talk appears to be the spatial derivative of the profile of the star (Dye et al., 2006). The first and second order cross-talk artifacts are easy to spot as they appear doughnut shaped (see Fig. 5.4). Further orders are more difficult to identify as they appear as faint sources which could lead to artificial objects being introduced to catalogues. We have addressed this problem by writing a simple code that flags objects in the region of n×128 pixels from a bright star in the read out direction. These objects are flagged rather than removed so as not to rule out potential objects of interest near an incident of cross-talk.

There are a number of other image artifacts that are mercifully less prolific and less likely to be confused with real objects. Persistence images of saturated stars tend to appear in several subsequent frames in the telescope observation run. They are removed in the stacking process as long as the telescope pointings are not observed in the same order each time. As with most optical/near-infrared observations diffraction spikes related to the mirror supports are present with bright objects, an example of this can be seen on Fig. 5.4. Such spikes do not cause any major problems and

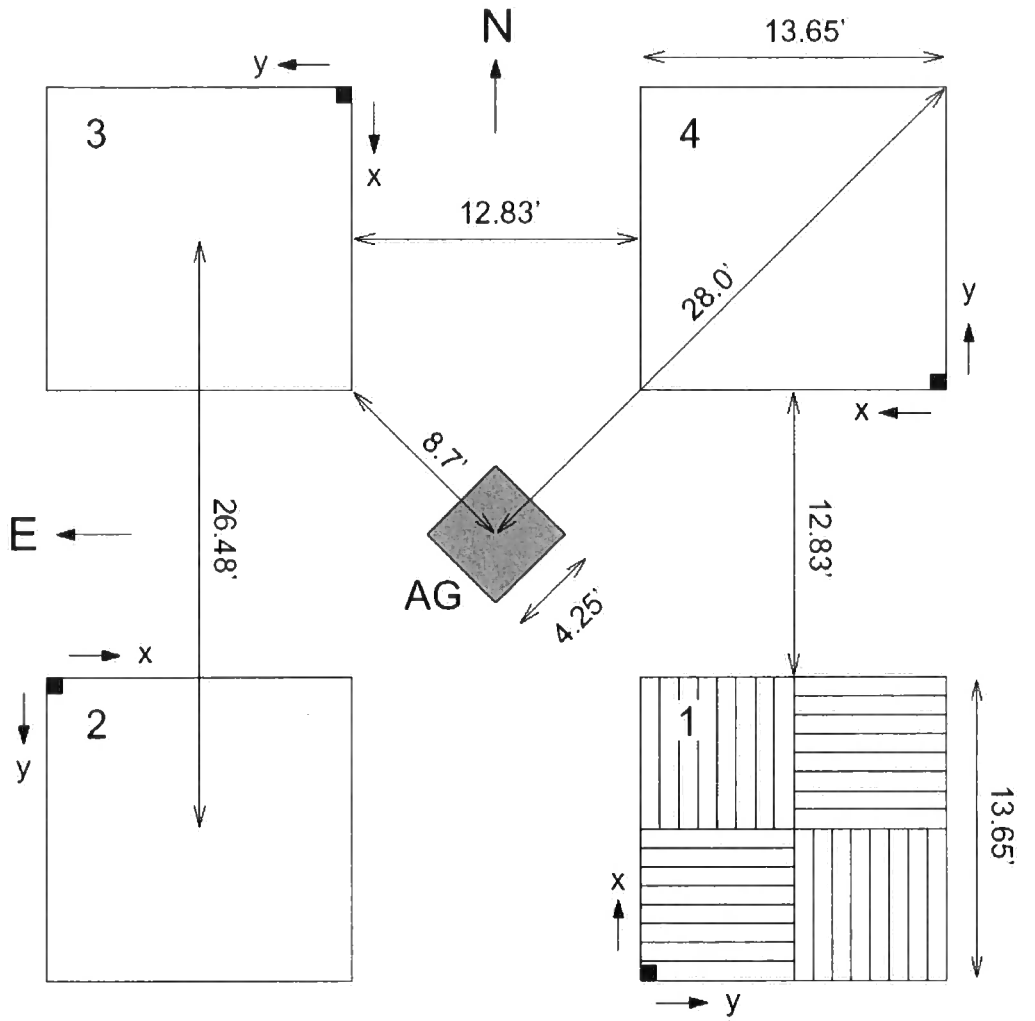

Figure 5.2: The focal plane layout of WFCAM displaying the four main detectors and the autoguider. The four readout directions are shown on detector 1. The north and east directions on the sky are denoted by N and E respectively. (Dye et al., 2006)

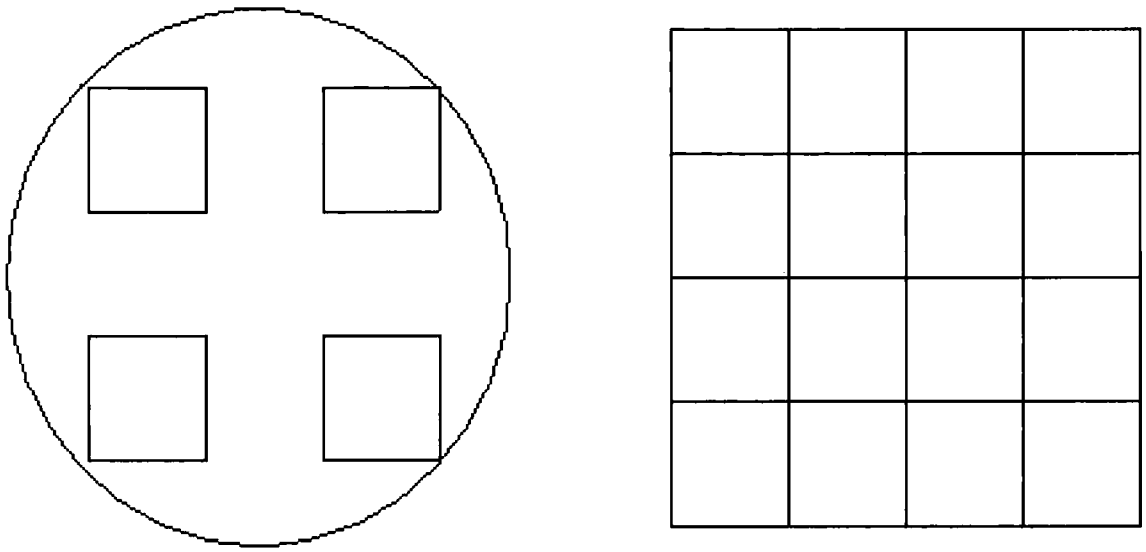

Figure 5.3: *left*: The WFCAM data frames appear as 4 image footprint. The squares represent individual detector images. *right*: The footprint frame on the *left* is then combined with three others to create a 4 detector $\times$ 4 detector contiguous mosaic. Image from URL: http://www.roe.ac.uk/atc/projects/wfcam/.

can be masked out in any analysis performed. Along with artifacts associated with the detector and telescope design, there are some images of marks or dirt on the field lens that occasionally make it into the data. This is particularly noticeable when there is a bright moon to illuminate them with scattered light. These artifacts are removed by the stacking process but in some cases it was necessary to inform the coordinators of the WSA archive that some frames were not to be used for creating science images. Such artifacts have been addressed in later observing observing campaigns with the cleaning of the mirror and the introduction of a policy not observe targets within 15 deg. of the moon.

5.5 DXS catalogue creation

We initially set about making near-infrared (J and K band) object catalogues for the deepest areas of each of the DXS regions for use in future analysis. Rather than using the official WSA catalogues we extract our own from the original images in an attempt to gain extra depth. The images we use are the 'deep stacks' created

Figure 5.4: An example of cross-talk (doughnut shaped artifacts) in the detector read out direction caused by a bright star on a WFCAM image.

by the WSA. The deep stacks are coadded images of all of the frames in the DXS. The deep stacks downloaded from the WSA archive are single WFCAM footprint images.

We now describe the method to make a full mosaic tile out of these stacks for each of the DXS regions. We first convert the astrometric projection type of the frames from ZPN to ZPX. This is because we wish to remove bad pixels from the outer edge of the images using the Image Reduction and Analysis Facility (IRAF) software which only recognises the former. We perform this conversion with a small adjustment to the fits header using IRAF's **hedit** command:

CTYPE1: RA—ZPN -> RA—ZPX

CTYPE2: DEC–ZPN -> DEC–ZPX

add WAT1_001 = wtype=zpx axtype=ra projp1=1.0 projp3=-50.0

add WAT2_001 = wtype=zpx axtype=dec projp1=1.0 projp3=-50.0

We then use IRAF's **imcopy** command to split the deep stack images into their four individual detector frames and trim the edges. This ensures the final mosaic is

as clean and cohesive as possible. We find that removing the outer 50 pixels around each tile is adequate although up to 100 pixels are removed in extreme cases. As the gaps between the detectors in the WFCAM footprint are smaller than a whole detector, this trimming does not effect sky coverage.

To make a contiguous Mosaic of WFCAM deep stacks we run the TERAPIX SWarp software on the cleaned tiles. The DR2 SA22 3.3 square degree K band image is displayed in Fig. 5.5 and a close up showing the quality of the data is in Fig. 5.6. We find that these tiled images have a highly consistent world coordinate system when compared to the WSA UKIDSS catalogue, 2MASS and the United States Naval Observatory (USNO) star catalogue. To extract the J and K band catalogues from the large mosaiced images we use the SExtractor software of Bertin & Arnouts (1996). We run SExtractor in dual mode so that the K band catalogue detections are used to extract the J band photometry. This method ensures that the same aperture sizes are used in both images to give precise colour determination. We employ 2 arcsecond apertures for this colour extraction. We also extract a total magnitude in the same way. This is SExtractor's 'Best' magnitude which is the Kron style AUTO_MAG aperture for uncrowded objects and reverts to an isophotal aperture in dense object regions. The photometric zero points for the images are calculated from the official WSA catalogues which have been shown to be remarkably consistent with 2MASS (Dye et al., 2006).

5.6 DXS colour-magnitude diagrams

We can now perform some basic analysis on the catalogues created in §5.5. This begin with the creation of colour-magnitude diagrams for the individual DXS regions. The following $J-K$ versus K colour-magnitude plots (figures 5.7, 5.8 and 5.9) employ matched 2 arcsecond apertures for the $J-K$ colour and SExtractor's 'Best' magnitude for the K band magnitude. We find K band point source, 5 sigma magnitude limits of 20.4, 20.7 and 20.5 for the Elais N1, SA22 and XMM fields respectively approaching the desired depth of K=20.8 mag. The Lockman Hole field is absent as the J band data are currently too shallow for displaying a well

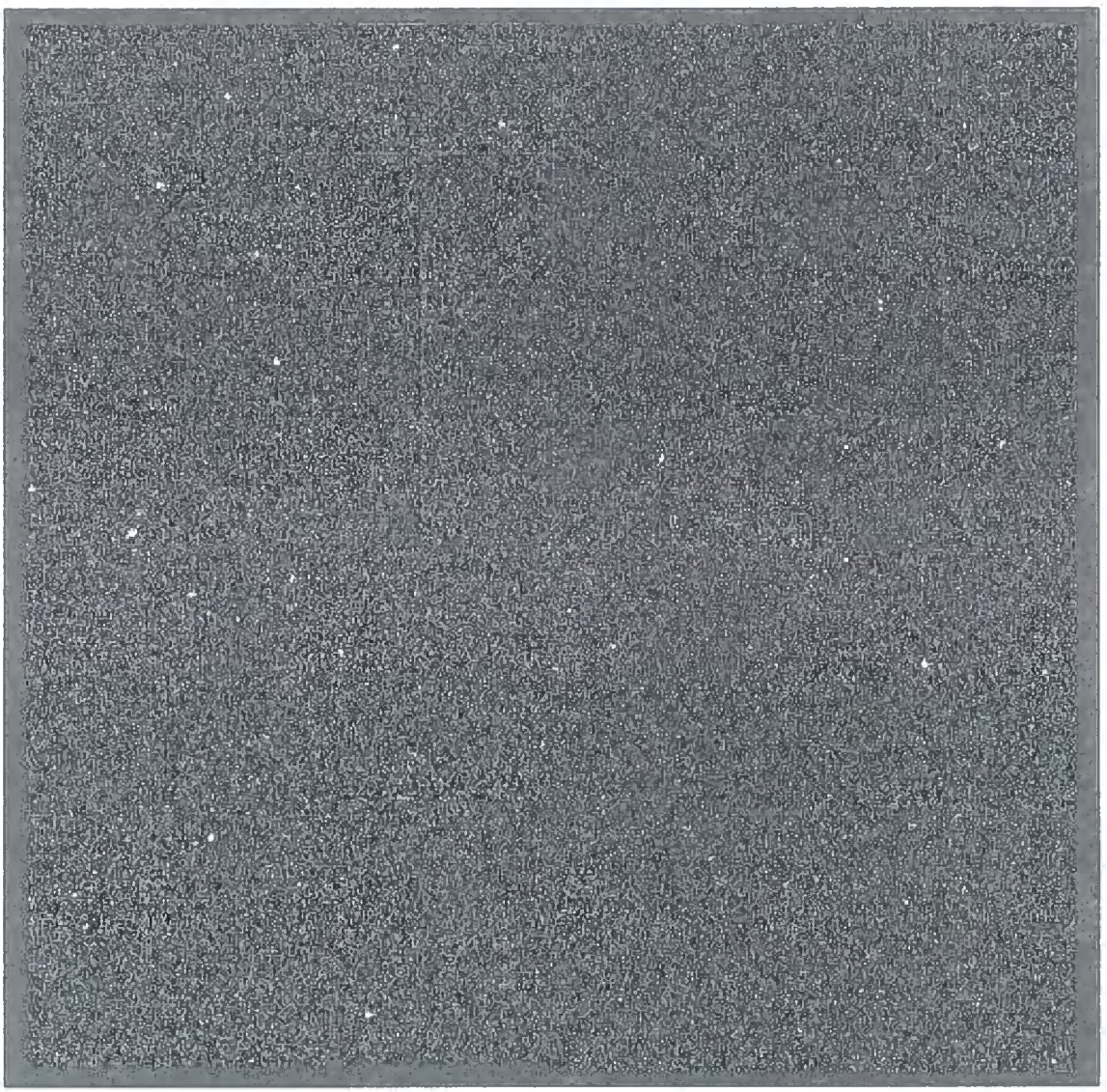

Figure 5.5: The 3.3 square degree WFCAM mosaic of the SA22 region in the K band.

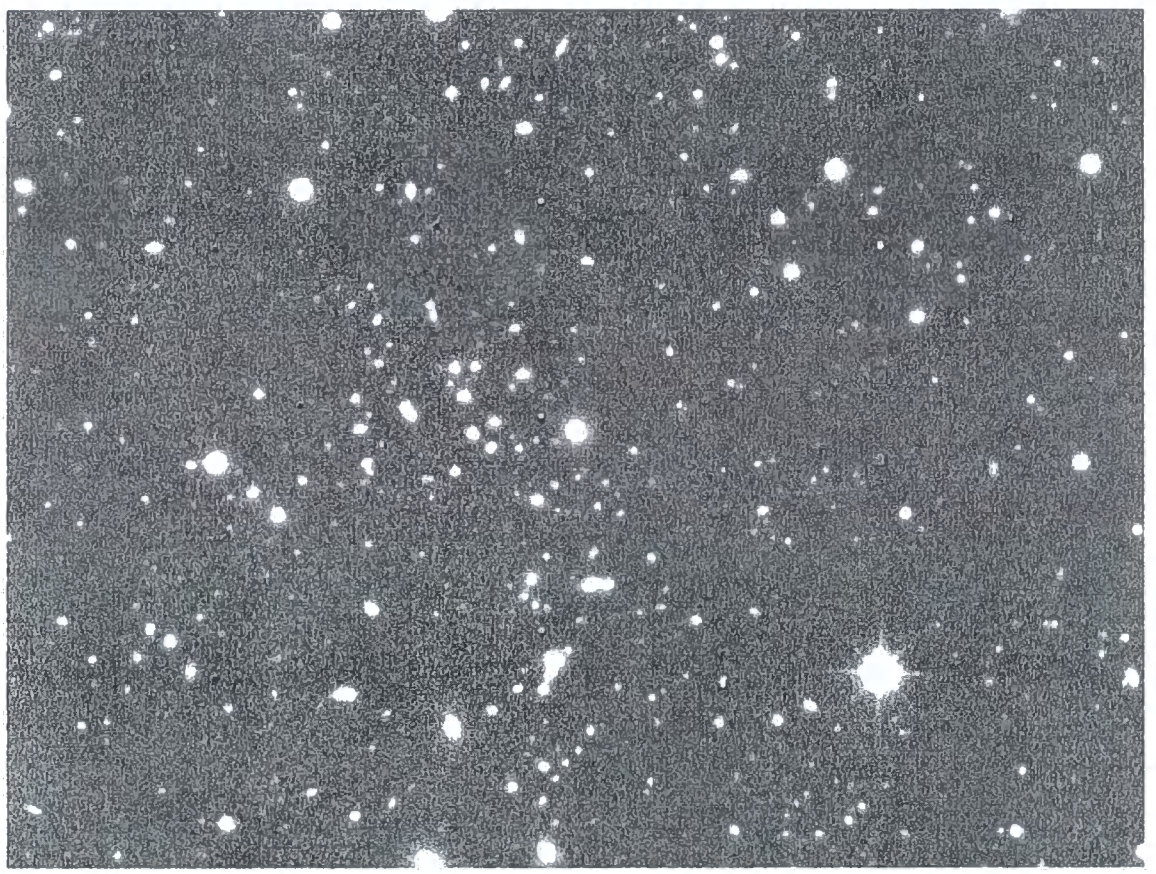

Figure 5.6: A close up image of a galaxy cluster in the SA22 K band mosaic.

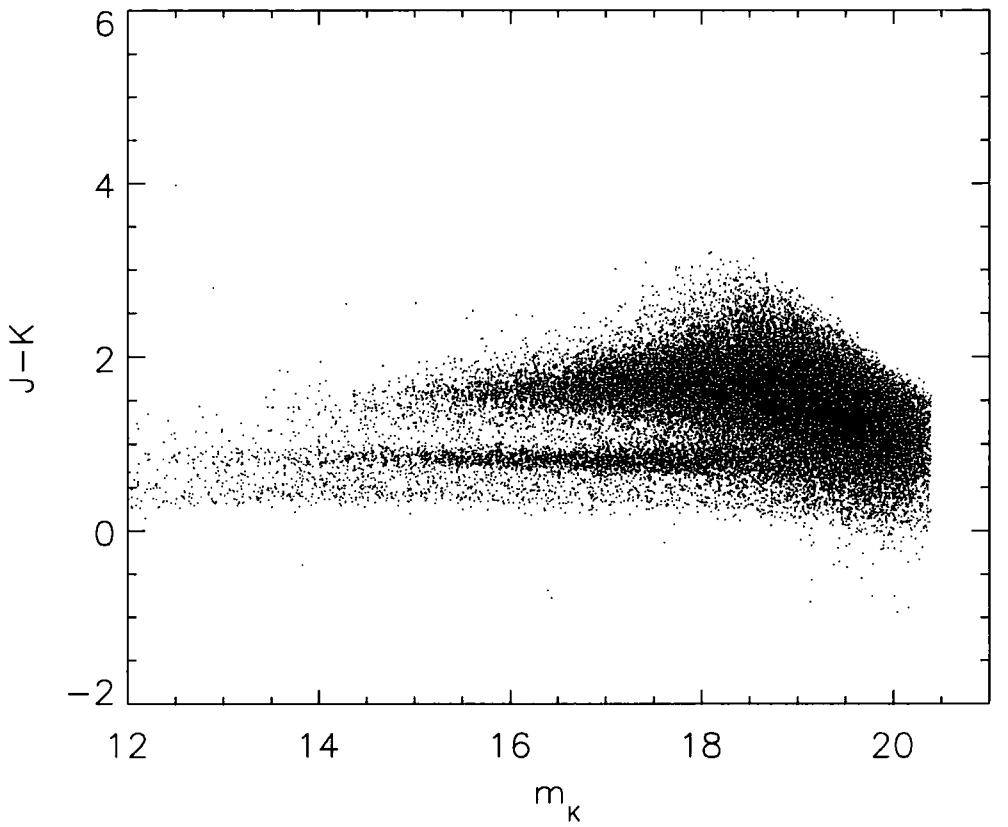

Figure 5.7: The J-K versus K colour magnitude diagram for the Elais N1 region (DR1).

defined colour-magnitude plot. The colour-magnitude diagrams come from either the UKIDSS DR1 or DR2 release (noted on plots). The UKIDSS DR3 is due in autumn 2007.

The colour-magnitude plots display two obvious features. The first is the stellar sequence comprising stars from the Galaxy. This is the prominent flat sequence with $J-K$ <1. This sequence has very little scatter demonstrating that our photometry is good across the whole image. The second feature is the galaxy sequence which is the population above $J-K$=1. This is a composite of many red sequences at all redshifts. This additional colour segregation between stars and galaxies is an additional bonus for near-infrared studies.

In Chapter 6 we successfully use these catalogues in combination with optical and mid-infrared data to search for high redshift galaxy clusters.

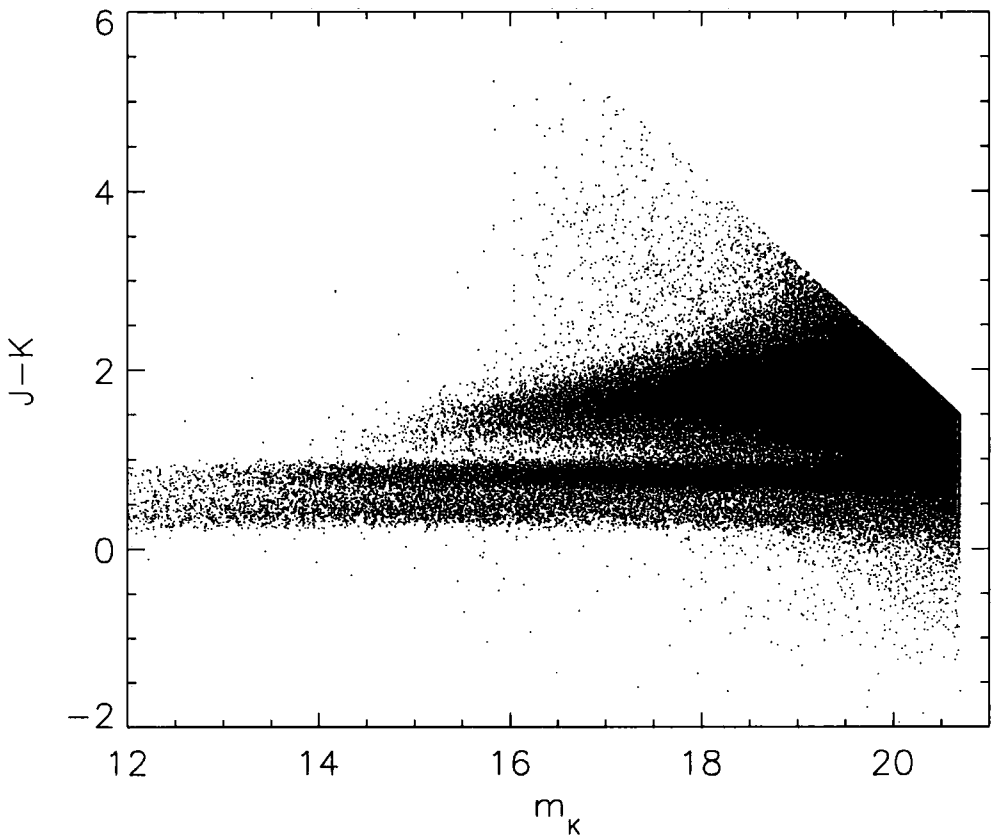

Figure 5.8: The J-K versus K colour magnitude diagram for the SA22 region (DR2). This covers a larger area than the Elais N1 and XMM-LSS fields so the point density is higher.

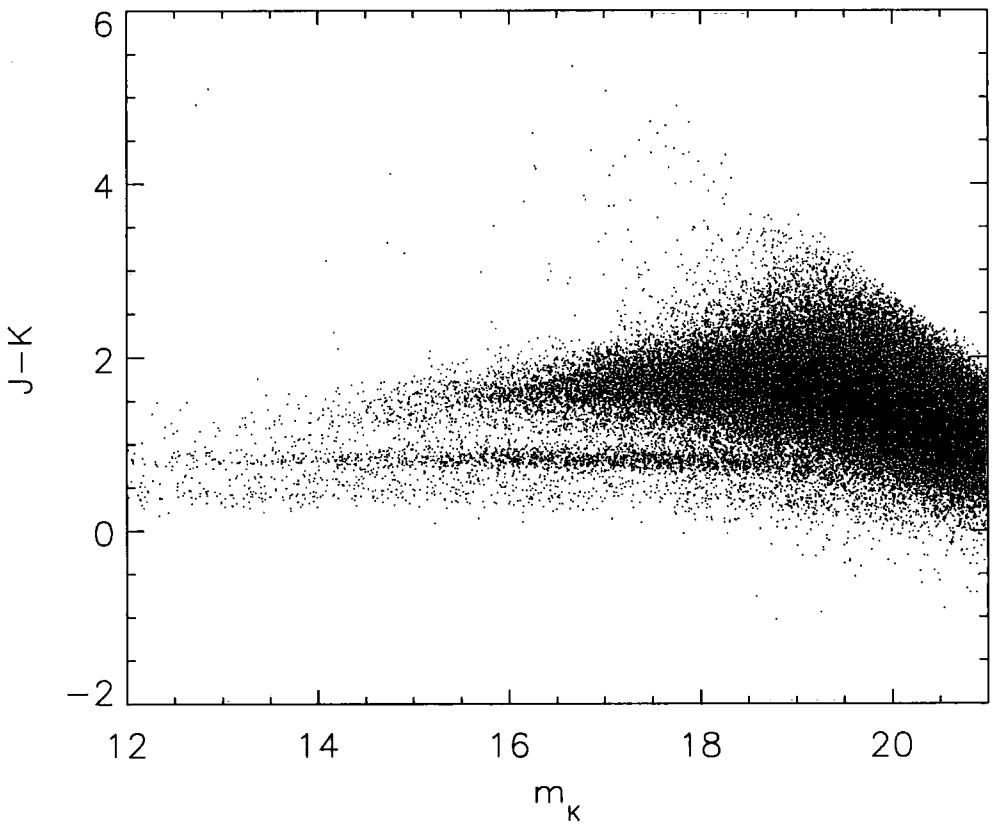

Figure 5.9: The J-K versus K colour magnitude diagram for the XMM - LSS region (DR1).

5.7 DXS source counts

Galaxy number counts have been widely used for the study of galaxy evolution and cosmology (see Koo & Kron 1992 for review). Although this is now less popular than modern cosmological techniques, it is still an interesting probe of the data quality of a survey.

We present the source counts per unit area for the sources in 3 DXS regions from §5.6. To discriminate between stars and galaxies we use the observation that in general objects with $J - K > 1$ are galaxies and those with $J - K < 1$ are stars which is in agreement with the CLASS_STAR parameter of SExtractor. Fig. 5.10 compares our DXS star counts to those of the FLAMINGOS Extragalactic Survey (FLAMEX, Elston et al. 2006). These are in good agreement and this strengthens the case for our star-galaxy separation. From Fig. 5.10 we can also see that the galaxy counts for the three DXS fields are qualitatively similar but with small field to field differences due to cosmic variance. Fig. 5.11 displays the total galaxy counts for our entire sample. We compare our counts to those from a number of similar surveys: the Calor Alto Deep Imaging Survey (CADIS, Huang et al. 2001); Kümmel & Wagner (2001); the UKIDSS Ultra Deep Survey (UKIDSS UDS, Lane et al. 2007); the Munich Near-Infrared Cluster Survey (MUNICS, Drory et al. 2001, Feulner et al. 2007). Figures 5.10 and 5.11 confirm that the UKIDSS DXS source counts from our catalogues are in good agreement with previous works demonstrating the quality of our data. The higher galaxy counts in the range $17 < m_K < 19$ compared to the other surveys is probably due to the overdensity seen at redshift 1 in the Elais N1 field (Chapter 6).

Figure 5.11 also includes the source counts from the official UKIDSS WSA catalogue. We find that this catalogue over predicts the number of bright galaxies when compared to our independent UKIDSS catalogues and the MUNICS sample. The reason for this is unclear as the photometric residuals between our catalogue and the WSA data are consistent to within 0.1mag. From studying both catalogues and images we suggest this is due to the double counting of relatively luminous, extended objects in the official WSA analysis.

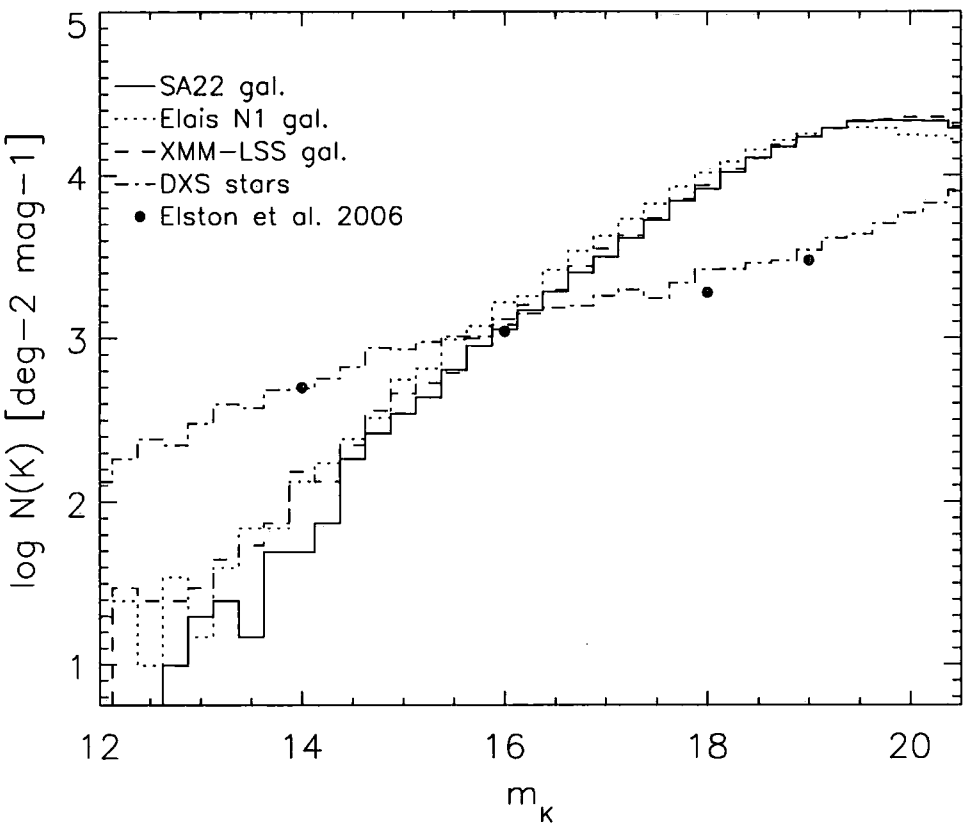

Figure 5.10: The star counts for the combined DXS sample and galaxy counts for the individual DXS regions. Uncorrected for relative completeness.

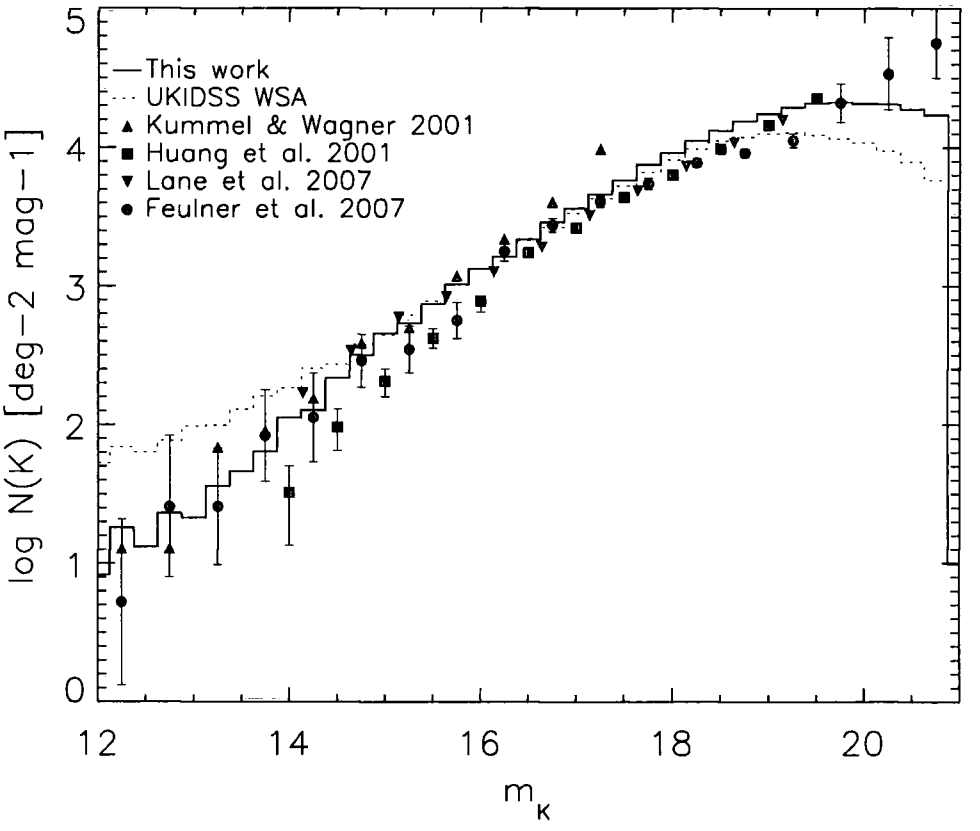

Figure 5.11: The galaxy counts per square degree for the combined DXS sample with comparison to other similar studies. Uncorrected for relative completeness.

Chapter 6

High redshift cluster selection

Overview

In this chapter we discuss methods for high redshift galaxy cluster detection and present the details of our own cluster detection algorithm. This simple algorithm selects clusters based on the near-infrared and optical properties of the red sequence, drawing on our research detailed in chapters 2, 3 and 4. We describe the application of the algorithm to object catalogues from the UKIDSS DXS fields in order to find clusters at $z \sim 1$. By comparing the observed cluster abundances to simulations we conclude that our algorithm is sensitive to cluster masses in the range $10^{13.9}M_{\odot}$–$10^{15}M_{\odot}$. To confirm the presence of the clusters we have acquired deep multi-object spectroscopy on the photometric members. This follow-up reveals a z=0.9 supercluster in the Elais N1 field and we have been awarded further time to perform spectroscopy on candidates in the SA22 field. The clusters found in this study are fed back into the high z regime of our galaxy evolution research.

6.1 Introduction

The selection of galaxy clusters was originally performed by studying photographic plates. This technique was successful for local clusters but did not have sufficient depth to select distant clusters. With the advent of wide field CCD detectors we are now in the era of deep imaging surveys with the sky coverage required to discover a significantly large number of high redshift (z >0.5) galaxy clusters. Such surveys are being undertaken in the optical (Pan-STARSS, SDSS, Adelman-McCarthy et al. 2006) and the near-infrared (UKIDSS, Lawrence et al. 2006) which can in principle detect clusters out to z=2. Finding high redshift clusters is becoming increasingly important for providing astronomers with constraints on both galaxy evolution and cosmology as shown in chapters 2, 3 and 4. In addition, gravitational lensing analysis of these clusters gives a unique opportunity to view objects in the early Universe.
To analyse data from surveys designed to find high redshift galaxy clusters a robust method for cluster detection is required. The most popular cluster detection techniques are either based on the luminous X-ray emission from the intracluster medium (ICM) or on the red sequence of passive elliptical galaxies. We discuss both these cluster detection methods in §6.2.

6.2 Cluster selection techniques

The basis for all optical cluster selection techniques is the search for over-dense regions of galaxies on the sky. A review of optical cluster selection techniques is given in Gal (2006). The earliest cluster catalogues of Abell and Zwicky utilised the simple technique of counting galaxies in a fixed magnitude interval in cells of a fixed physical or angular size. This technique proved to be very successful for finding low redshift clusters. Higher redshift cluster detection requires more sophisticated techniques to improve the contrast of clusters over the significant foreground contamination. The most popular modern optical techniques for cluster selection are the matched filter, maxBCG, cluster red sequence and Voronoi Tessellation methods. Here we give a brief overview of these methods.
The matched filter technique of Postman et al. (1996) utilises only the luminosity

and spatial distribution of galaxies in the cluster. Clusters are found by comparing observations to model cluster luminosity functions and radial profiles. As a by product of this technique one can get an estimate of total luminosity and redshift (from comparing the Schechter parameter m^* to photometric evolution models, such as those in chapter 2). The matched filter technique is powerful as it improves the contrast of clusters over the background by using a simulated optimal 'filter' for the radial profile and luminosity function. However, this technique can miss clusters that do not conform to this input 'filter'.

Another method which does not necessarily require multi-band photometry is Voronoi Tessellation (VT). For any distribution of particles it is possible to define a characteristic volume associated with each particle. This is known as the Voronoi volume. If one completely divides up a region using these volumes we have a Voronoi Tessellation. This technique can be applied to cluster selection (Kim et al., 2002). The main advantage of the VT method is that it does not assume anything about the shape of the cluster and just works with the density of galaxies. The inverse of the area of the Voronoi cell associated with each galaxy gives the local density at that point. Therefore a set of small high density cells (above a specified threshold) mark the location of a galaxy cluster.

In contrast, the maxBCG and red sequence techniques require multi-wavelength data as they both rely on the fact that the red sequence of cluster ellipticals has a narrow range in colour. The maxBCG method was originally developed for use with SDSS (Annis et al., 1999). We have shown in chapter 2 that BCGs have a small scatter in absolute magnitude and a predictable photometric evolution with redshift. The maxBCG method exploits this and calculates the likelihood that each galaxy in the survey is a BCG based on its photometry, predicted redshift and the presence of a suitable red sequence from surrounding objects. Like the other red sequence methods this can fail at high redshift $z > 1$ as the cluster galaxy population becomes increasingly heterogeneous, although red sequences are still seen out to $z \sim 1.5$ (Stanford et al., 2006). BCGs with unusually blue colours due to cool core star formation (chapter 2) will also cause the failure of this technique.

The cluster red sequence method was used by Gladders & Yee (2000) for the Red

sequence Cluster Survey (RCS). The cluster red sequence method searches for sequences that are similar to those of model or known clusters. If the colour used straddles the 4000Å break at a given redshift then the cluster ellipticals at that redshift are redder than foreground contaminants. This removes the majority of the field galaxies. Clusters are found based on overdensities of objects within overlapping slices of colour magnitude space. This technique will again provide a good estimate of the cluster redshift based on the colour of the sequence.

Moving away from optical-infrared studies, cluster selection in the X-ray is performed by searching for extended sources of X-ray emission. This X-ray emission comes from the hot gas (ICM) in the form of bremsstrahlung and atomic transitions in metals. Examples of surveys that successfully employed this method are the *ROentgen SATellite* (*ROSAT*) Brightest Cluster Survey (BCS, Ebeling et al. 1998), the MAssive Cluster Survey (MACS, Ebeling et al. 2001) and the *XMM Newton* Cluster Survey (XCS, Romer et al. 2001). However, in order to select a large number of high z cluster candidates with X-ray observations will require future surveys that combine both a wide area and a deep flux limit.

6.3 The algorithm

The simple algorithm we use to discover high redshift clusters makes use of the red sequence in optical and near-infrared bands. To write this algorithm we can draw on experience from Chapters 2, 3 and 4 which detail the evolution of the red sequence since z=1. This algorithm is similar to that used for the cluster red sequence technique of Gladders & Yee (2000).

Our red sequence detection algorithm is set to run on an object catalogue extracted from a region of sky. In our case this is a catalogue from one of the UKIDSS DXS regions with J, K and I band coverage. We initially select objects that appear to be galaxy cluster members based on their photometry. This selection helps remove false detections but also reduces the computer time required. We remove stars by selecting only objects with a $J-K$ >1 (Vega). Objects from the edge of the image catalogue are also removed to limit false object detections. By selecting a slice of

colour magnitude space based on our research from chapters 2, 3 and 4 we can begin to select clusters in specific redshift ranges. This is useful for removing field contamination as most field galaxies will lie blueward of the red sequence in high-z clusters.

The algorithm itself works by laying down an aperture on each object that is a photometrically selected member of our catalogue. The size of this aperture is determined by the size of a typical cluster core in the redshift range we are searching in. The typical cluster core size we choose is 1 Mpc in diameter which we convert to an angular diameter on the sky. This core size is chosen as it maximises the detection efficiency of the algorithm and is physically sensible. Core sizes larger than this wash out smaller structures whereas smaller apertures are prone to statistical noise as they contain less galaxies. An aperture that is overdense in objects in the specified colour-magnitude slice by 3 sigma, when compared to the background average for the field, is flagged up as a cluster candidate.

Here we give an example of the parameters required by our algorithm to detect clusters at $z \sim 1$ in a UKIDSS DXS region catalogue of near-infrared J and K band data. We first calculate the 1 Mpc angular diameter of the cluster aperture at $z = 1$, which is 125 arcsec. From studying the observations and theoretical predictions from chapter 2 we can determine the constraints to place on the photometry of our object catalogue that corresponds to red sequence galaxies at $z = 1$. These plots describe the evolution of the brightest cluster galaxy (BCG) luminosity and colour out to $z = 2$. From the Hubble diagram we can see that a typical BCG at $z = 1$ is fainter than $m_K = 15$. We therefore only look for galaxies fainter than this. From the colour evolution plot we can see that a typical BCG at $z = 1$ has a $J - K$ colour of $1.6 < J - K < 2$ so we adopt this as our red sequence slice in colour space. The colour cuts for our selection criteria are horizontal in colour-magnitude space as the red sequence slope is comparable in magnitude to the uncertainties in our photometry. However, to allow for the slope the blue cluster selection limits for the colours are sufficient to account for the typical slope and photometry of the faint end of the red sequence z$\sim$1 (chapter 4). We include a similar constraint from the $I - K$ colour of $3.6 < I - K < 4.9$. The algorithm is then run on this colour-magnitude

selected sample. Further constraints can be added by including colour-magnitude information from additional wavebands if available. In this way one can build up a robust definition of a cluster elliptical and thus improve cluster detection.

6.4 Cluster Candidates

The algorithm described in §6.3 produces cluster candidates which we can then check by studying their photometry and morphology. We look for well defined red sequences in the candidate colour magnitude plots that resemble those of $z \sim 1$ clusters. False colour red green and blue (RGB) images of the candidates are created by combining the I, J and K band images. In these we look for accumulations of candidates from the algorithm. It is often possible to identify the BCG and an obvious cluster morphology strengthening the candidate's status. The strongest candidates from this visual inspection are then put forward to be confirmed by spectroscopy.

6.4.1 The Elais N1 field

The algorithm was first applied to object catalogues for the UKIDSS DXS Elais N1 field. This region was chosen as it was the first UKIDSS DXS data available, released as part of the UKIDSS early data release (EDR, Dye et al. 2006). The catalogue covers a 0.8 square degree area in the UKIRT J and K bands plus I band data from the Subaru telescope. The observations in this field achieve a depth of K=20.4.

The algorithm identified 15 z$\sim$1 galaxy cluster candidates within the Elais N1 field. This corresponds to 19 candidates per square degree. These candidates are of varying degrees of richness. The candidate surface density is high compared to other similar photometric surveys: 10 per sq. deg. (z =0.6–1.4) from the UKIDSS Ultra Deep Field (UDS, van Breukelen et al. 2006) and 7 per sq. deg. (z =0.9–1.4) from the Red Sequence Cluster Survey (RCS, Gladders & Yee 2005). From this we conclude that the Elais N1 field may be overdense at $z \sim 1$. Examples of the red sequences and images of the candidates are shown in figures 6.1, 6.2, 6.3 and 6.4.

For comparison with cosmological simulations we analyse the cluster abundance within the Millennium Simulation (Springel et al., 2005). The analysis was performed on the Bower et al. (2006) semi-analytic model catalogue. This is a model that includes feedback from active galactic nuclei in order to match the observed break in the luminosity function at bright magnitudes. The size of the simulation is $500h^{-1}$Mpc on the side and the available catalogues provide redshift snapshots of the structural evolution within. In order to quantify the simulated cluster abundance at z=1 we count the number of dark matter halos above a certain mass within this snapshot. If we make the initial assumption that galaxy clusters reside in dark matter halos with mass greater than $10^{14}M_{\odot}$ then we find that there are 4.8 clusters per sq. deg. in the simulation. This is clearly a lower abundance than the 19 clusters per sq. deg. we have in the Elais N1 field. The evidence from the UDS and RCS observations and comparison to simulation suggest there are two possibilities for this over-abundance of clusters: 1. we are looking at an over dense region of the sky; 2. our cluster detection algorithm is able to detect clusters to a lower mass limit than the UDS and RCS.

Spectroscopic confirmation of the 5 strongest Elais N1 candidates is found in §6.5.

6.4.2 The SA22 field

With the release of UKIDSS DR1 and DR2 we were able to analyse data from the other DXS fields (chapter 5). However, only the data for the SA22 DXS field was suitable for galaxy cluster selection as the Lockman Hole field had no J band data and the XMM-LSS field was too shallow in J. The algorithm was applied to our catalogue of the SA22 field. This catalogue covers 4 $\times$ the area of the Elais N1 catalogue (3.3 square degrees). The I band observations were taken with the Cerro Tololo Inter-American Observatory (CTIO) 4m Blanco telescope (P.I: A. C. Edge, observers: J. P. Stott & D. A. Wake). The observations in this field achieve a depth of K=20.7.

The algorithm finds 28 z$\sim$1 photometric cluster candidates within the SA22 field corresponding to 9 candidates per sq. deg. Fig. 6.5 is a surface density map of the SA22 region based on our J-K and I-K colour selection displaying the cluster

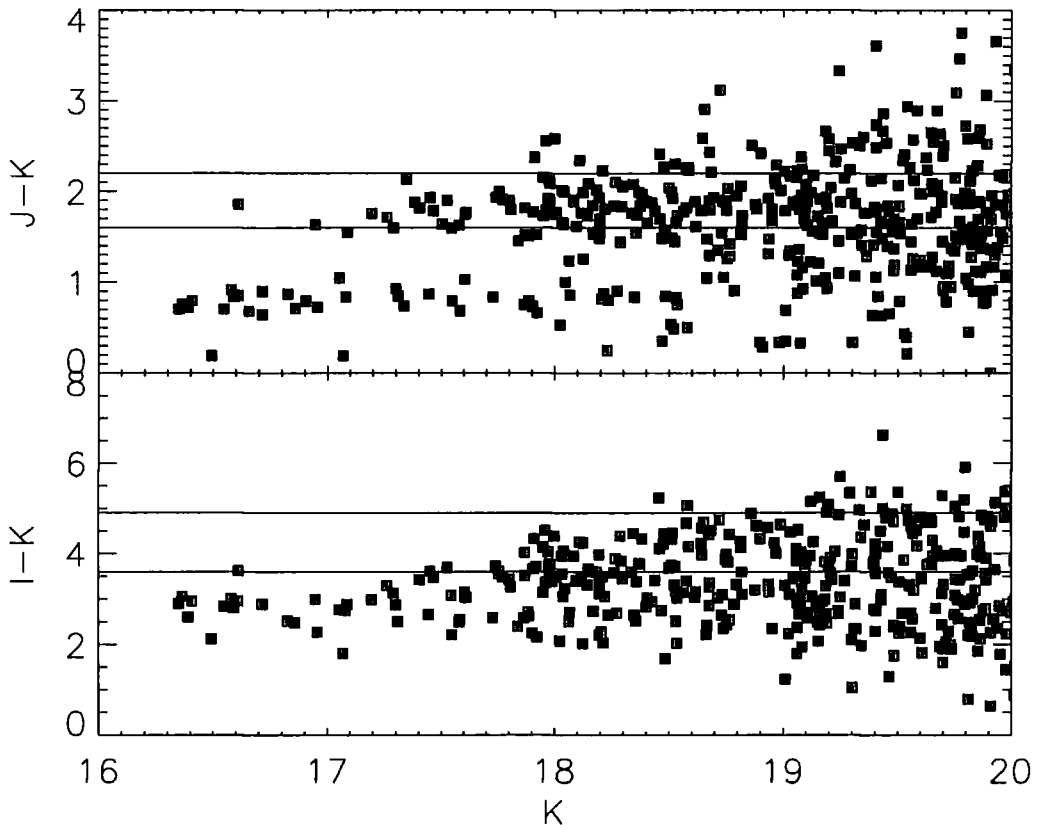

Figure 6.1: Optical and near-infrared colour magnitude diagrams for the $z \sim 1$ cluster candidate Elais N1-1. The solid horizontal lines correspond to the blue limit to the colour cuts used to identify potential cluster members.

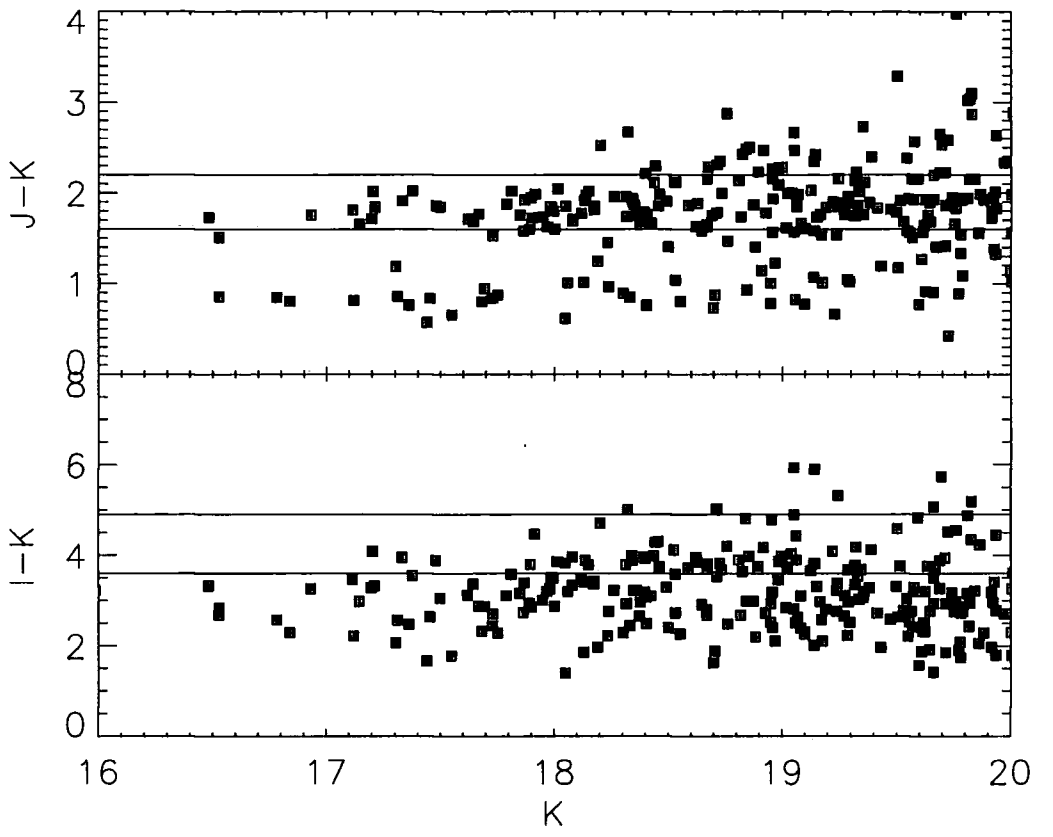

Figure 6.2: Optical and near-infrared colour magnitude diagrams for the $z \sim 1$ cluster candidate Elais N1-3. The solid horizontal lines correspond to the blue limit to the colour cuts used to identify potential cluster members.

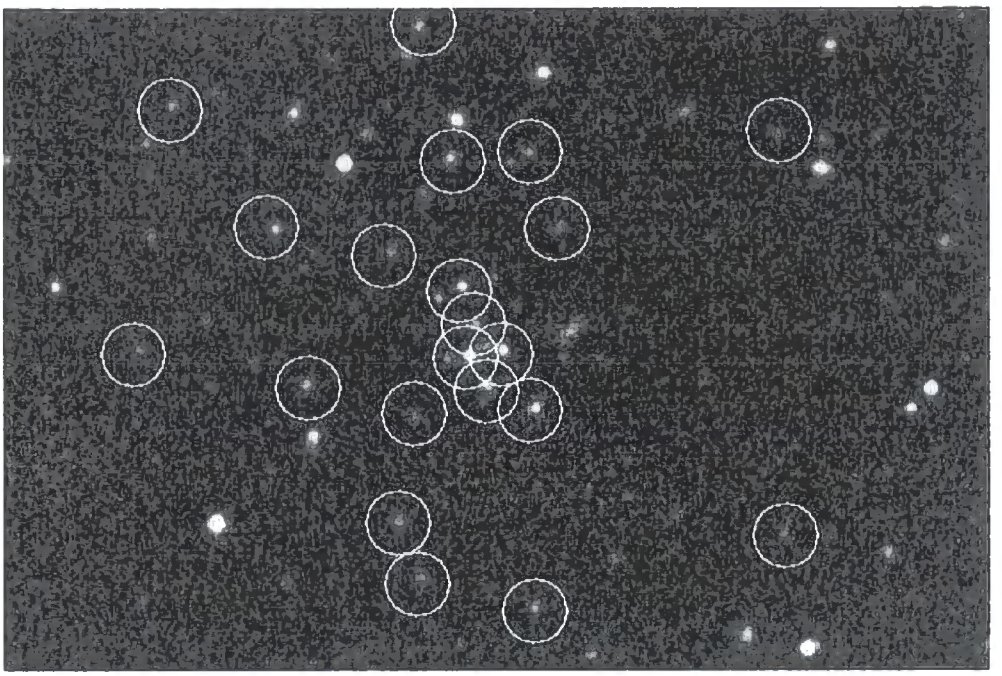

Figure 6.3: Optical near-infrared image of cluster candidate Elais N1-1. The highlighted objects are photometrically identified cluster members. This candidate was spectroscopically confirmed at z =0.88.

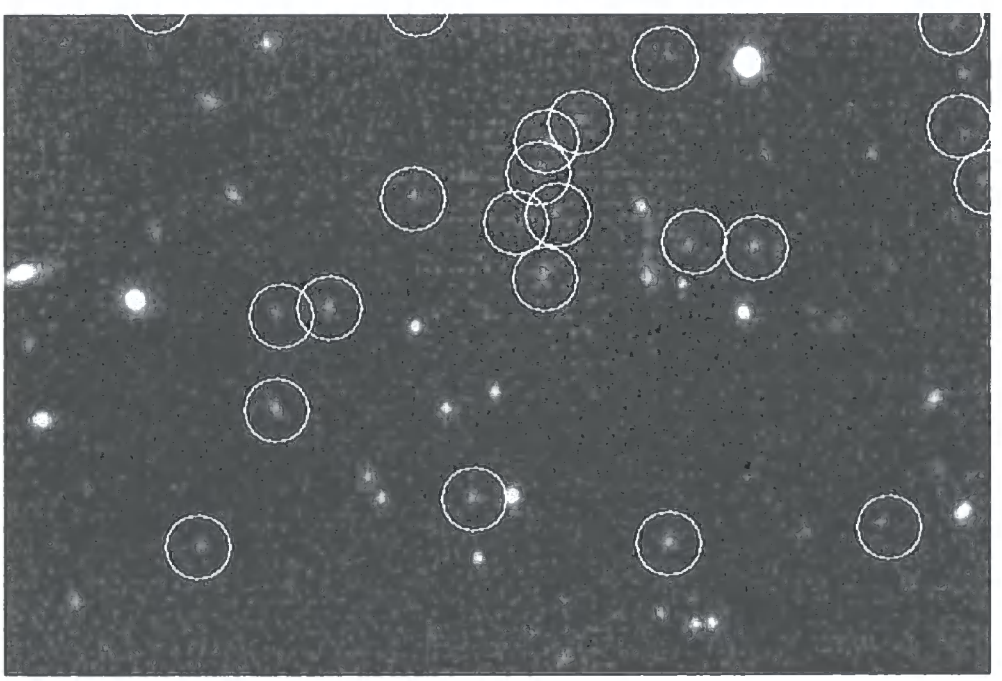

Figure 6.4: Optical near-infrared image of cluster candidate Elais N1-3. The highlighted objects are photometrically identified cluster members. This candidate was spectroscopically confirmed at z =0.897.

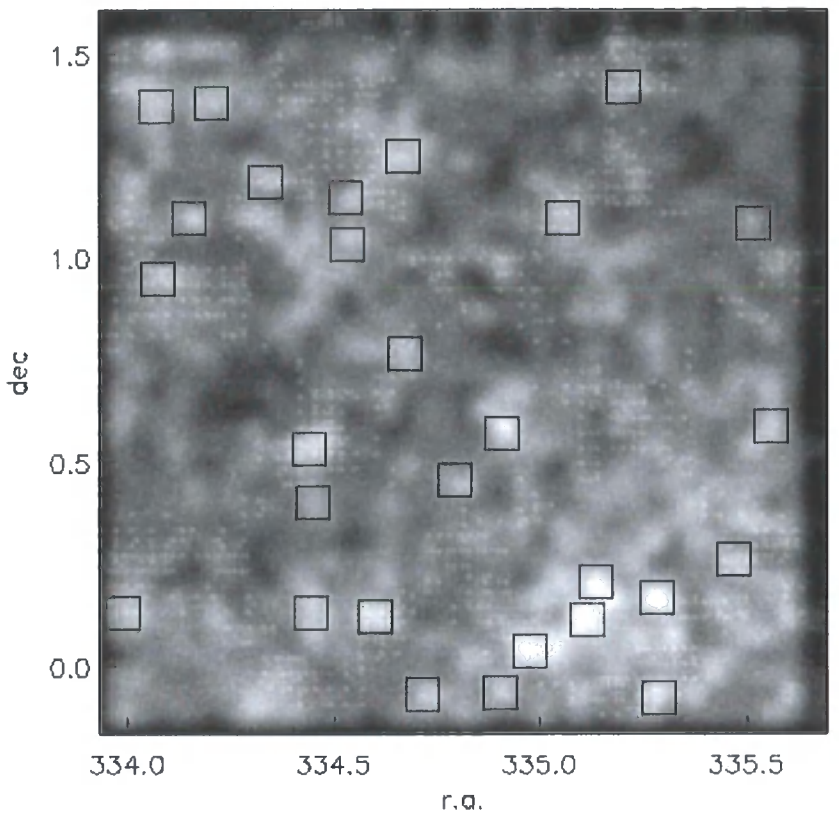

Figure 6.5: Surface density map of the SA22 region based on our J-K and I-K colour selection with the candidate clusters highlighted.

candidates in the region. This plot provides visual confirmation that the algorithm has again selected suitable targets. Fig. 6.6 is a histogram of the number of galaxies per 1Mpc cell for the SA22 region. We can see from this plot that there is a tail of overdensities with greater than 3σ significance from the random Gaussian distribution, demonstrating that our algorithm is selecting real structures above the noise. Examples of the red sequences and images of the candidates for the SA22 region are shown in figures 6.7, 6.8, 6.10 and 6.9.

The abundance of 9 candidates per sq. deg. is significantly lower that that of the Elais N1 field (19 per sq. deg.) but is comparable to the results of Gladders & Yee (2005) and van Breukelen et al. (2006). This result strengthens the case for the Elais N1 field being overdense.

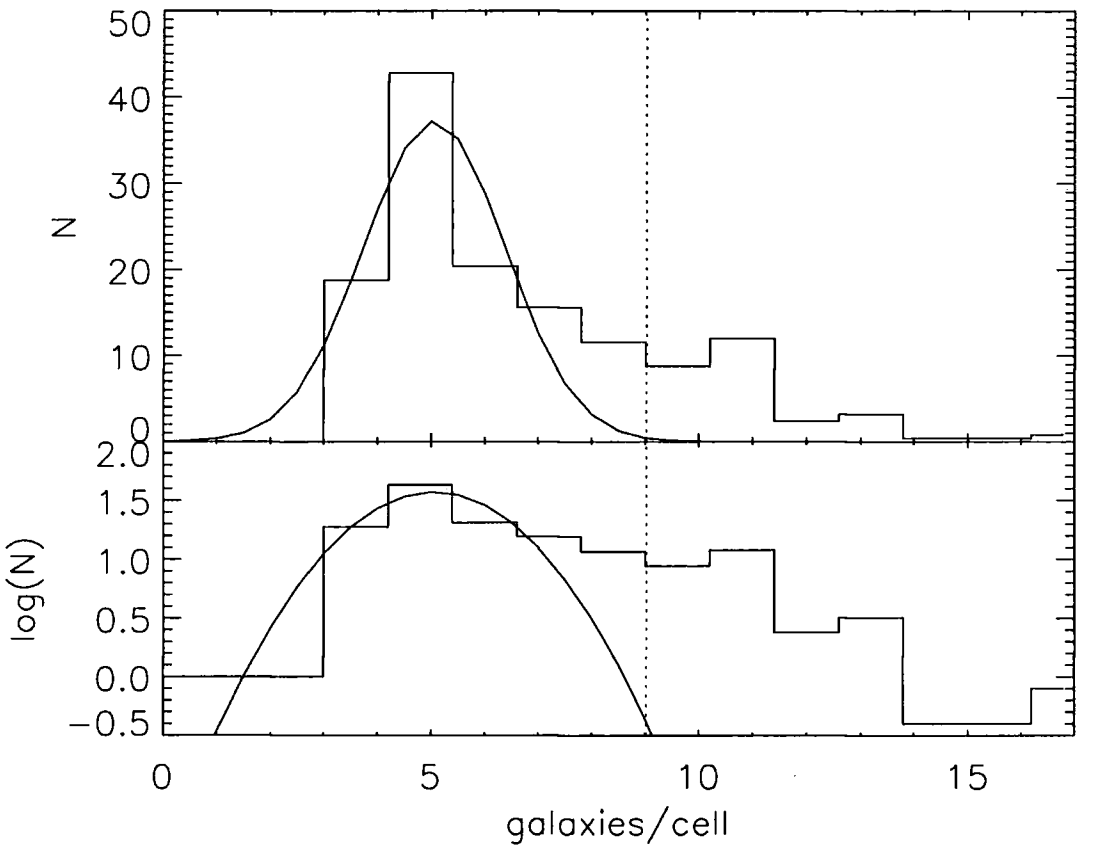

Figure 6.6: A histogram of the number of galaxies per 1Mpc cell for the SA22 region. This plot shows a significant tail of overdensities. The dotted vertical line is the 3σ limit above which we have our 28 candidates.

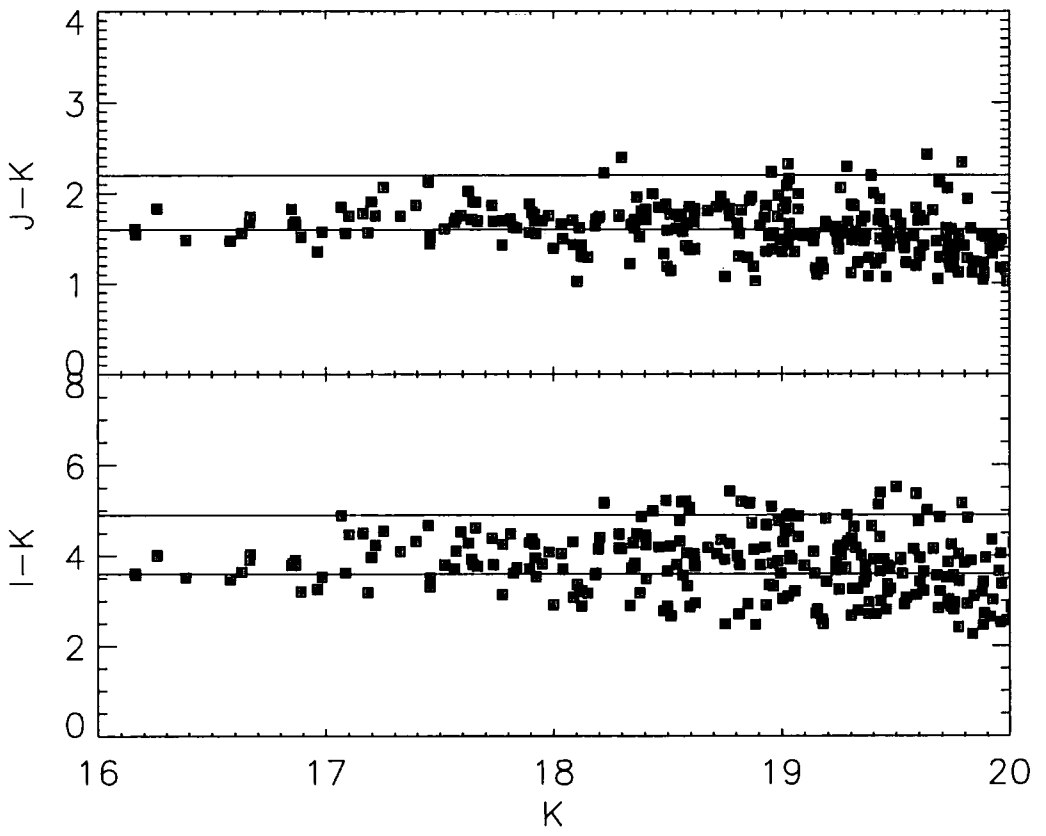

Figure 6.7: Optical and near-infrared colour magnitude diagrams for the $z \sim 1$ cluster candidate SA22-1. The solid horizontal lines correspond to the blue limit to the colour cuts used to identify potential cluster members.

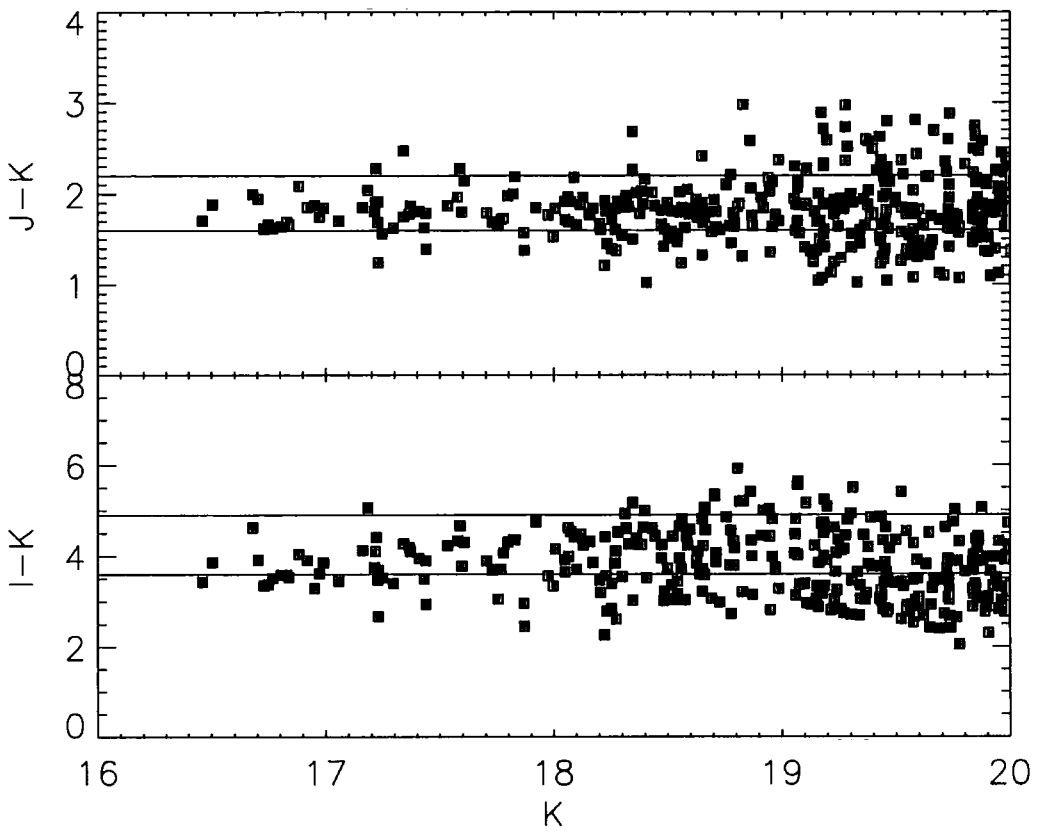

Figure 6.8: Optical and near-infrared colour magnitude diagrams for the $z \sim 1$ cluster candidate SA22-4. The solid horizontal lines correspond to the blue limit to the colour cuts used to identify potential cluster members.

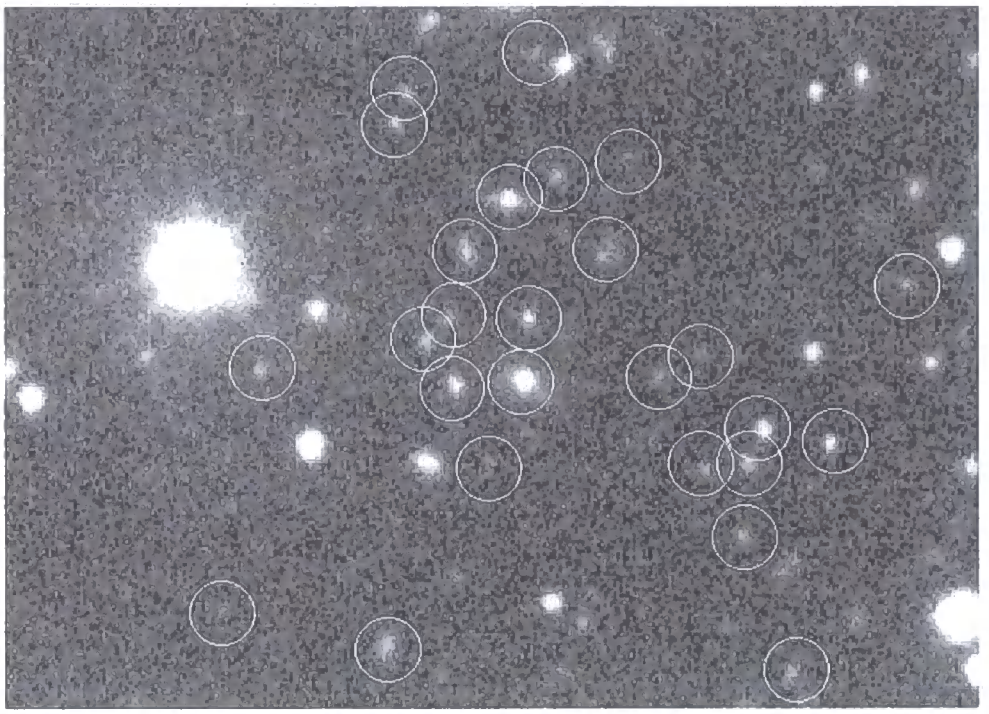

Figure 6.9: Optical near-infrared image of cluster candidate SA22-4. The highlighted objects are photometrically identified cluster members.

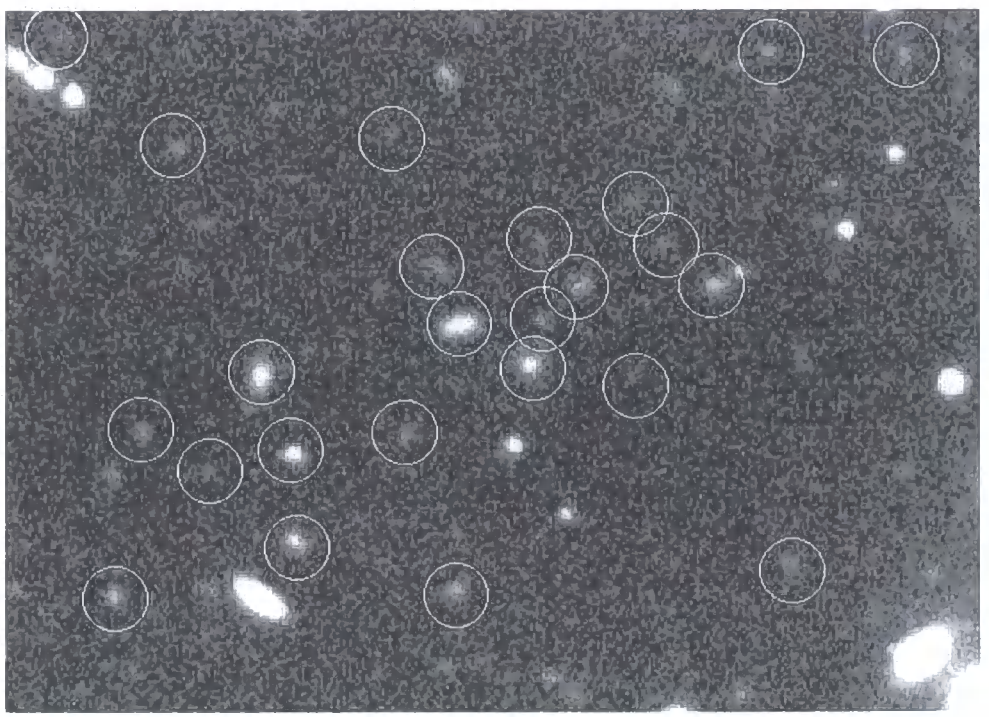

Figure 6.10: Optical near-infrared image of cluster candidate SA22-5. The highlighted objects are photometrically identified cluster members.

6.5 Spectroscopic Confirmation

Once we have our cluster candidates we then need to ascertain that they are indeed clusters and not just chance alignments. To achieve this we need spectroscopic data for the photometrically identified cluster members to confirm that they are at the same redshift.

The spectroscopic confirmation of the cluster candidates is achieved using Gemini Multi-Object Spectrograph (GMOS) on the Gemini North telescope. This instrument is ideal for our study of potential clusters as it is able to perform multi-slit spectroscopy and imaging over a 5.5 arcmin field of view. GMOS allows us to obtain ~30 slits per image mask, sufficient to confirm the presence and membership of a cluster. Our clusters are expected to be at $z \sim 1$ meaning we require good sky subtraction and removal of night sky lines so that weak spectral features can be identified. We therefore employ the Nod and Shuffle sky subtraction method (Glazebrook & Bland-Hawthorn, 2001). Nod and Shuffle works by observing the object and background alternately through the same region of the CCD by nodding the telescope. In between each observation the charge on the CCD is shuffled by a number of rows corresponding to the centre-to-centre spacing into which each slit is divided. Each alternate block is masked off so that it receives no light from the sky acting simply as an image store. The object and background exposures are repeated as desired and at the end of the sequence the CCD is read out, meaning that the read-noise only occurs once. For each galaxy the object and background blocks are subtracted to achieve the sky removal.

For the observations we use the GMOS OG515 filter in conjunction with the R400 grating and a central wavelength of 840nm. This gives a wavelength coverage of ~580-1100nm. The chip gaps on the CCD and any bad pixels are removed by performing observations in 2 different wavelength configurations of 840nm and 850nm respectively. Each cluster candidate was observed using the MOS mask through 1 arcsec wide slits for a total of 3.2 hours.

The redshifts for the cluster members are calculated by the identification of strong emission or absorption features in their spectra. The features under inspection included the [OII] 3727Å the 4000Å break, Ca H&K absorption at 3933Å, 3969Å

and the G-band at 4304Å. This analysis was performed by Mark Swinbank. A more detailed description of the spectroscopic technique, data reduction and results for our cluster candidates in the UKIDSS DXS Elais N1 field are given in Swinbank et al. (2007). Fig. 6.11 is a set of example GMOS spectra for a subset of galaxy cluster members in Elais N1.

The results confirm that all five Elais N1 candidates are in fact clusters at high redshift, including a pair of clusters in the Elais N1-4 region at z=0.88 and 1.09, proving the success of our algorithm. However, we also found that five clusters are at the same redshift (z=0.89±0.01) and spread across a 1 degree region of sky (corresponding to 30 Mpc). The redshift distribution for all of our target galaxies in the Elais N1 field is presented in Fig. 6.12. From this we conclude that we have discovered a large structure or supercluster of galaxies in the Elais N1 field. We can estimate the probability of discovering such a large system at z =1 by scaling the local space density of superclusters to the volume of the DXS survey (Swinbank et al., 2007). The probability of finding a supercluster in a field the size of Elais N1 is found to be $\sim$ 15% so although we were fortunate to study a field containing such a structure it is not improbable. This result explains the why the Elais N1 field has twice the abundance of z $\sim$1 photometric candidates as the SA22 field. If we assume that the SA22 field is a representative field on the sky then, based on abundances in the Millennium simulation, we find that our algorithm can detect clusters in the mass range $10^{13.8}M_{\odot}$–$10^{15}M_{\odot}$.

Fig. 6.13 shows the original optical-infrared colour-magnitude diagrams (in the AB magnitude system) for our 5 Elais N1 cluster candidates which were found to constitute the z = 0.9 supercluster. The now spectroscopically confirmed members of the clusters are labelled on this set of plots.

We have been awarded further observing time on GMOS on the Gemini North telescope (Principal Investigator: J. P. Stott). This is to spectroscopically confirm the status of our candidate clusters in the SA22 field and will be undertaken in autumn 2007.

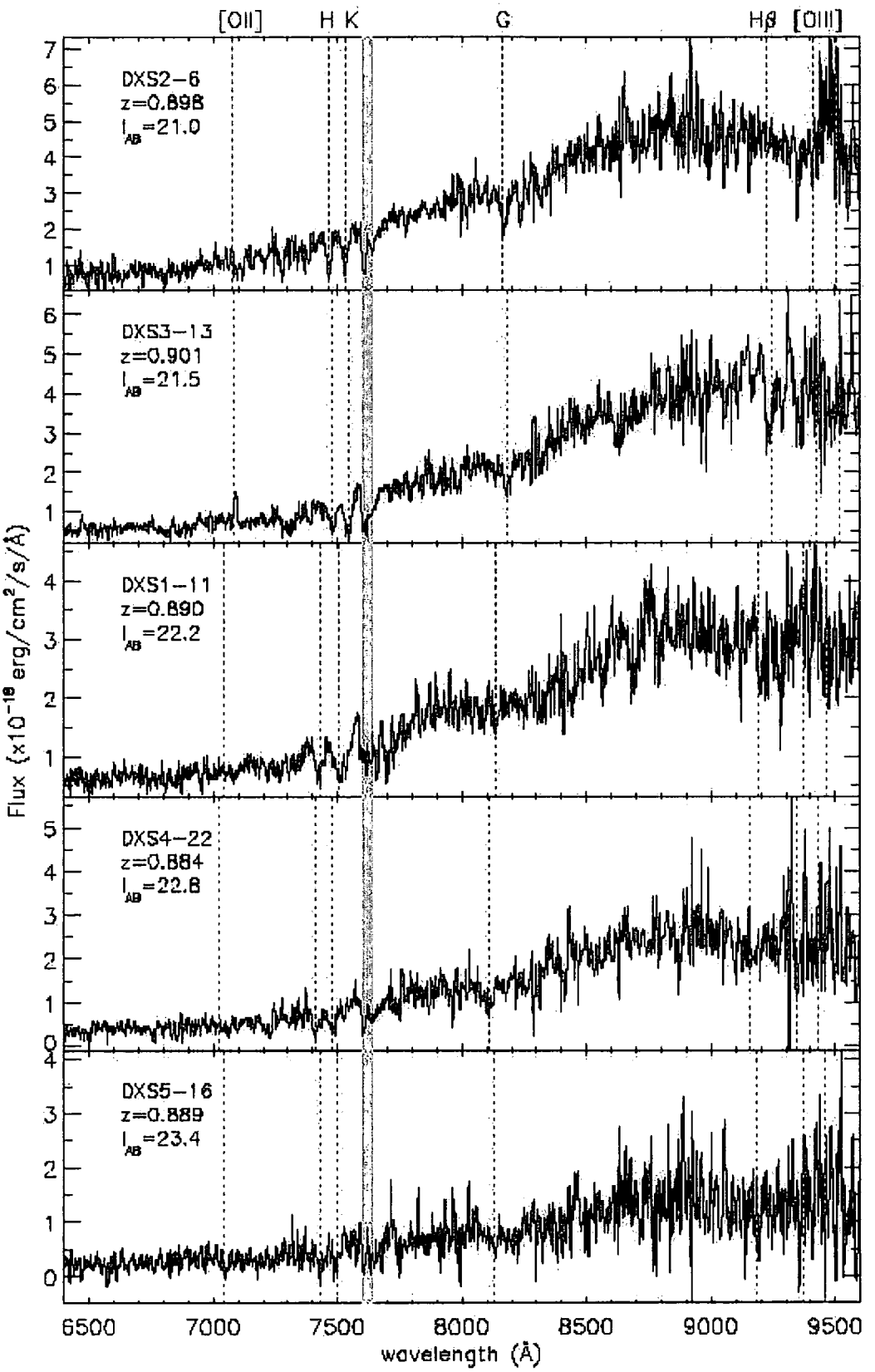

Figure 6.11: Example GMOS spectra for a subset of confirmed cluster members in the Elais N1 field (Swinbank et al., 2007).

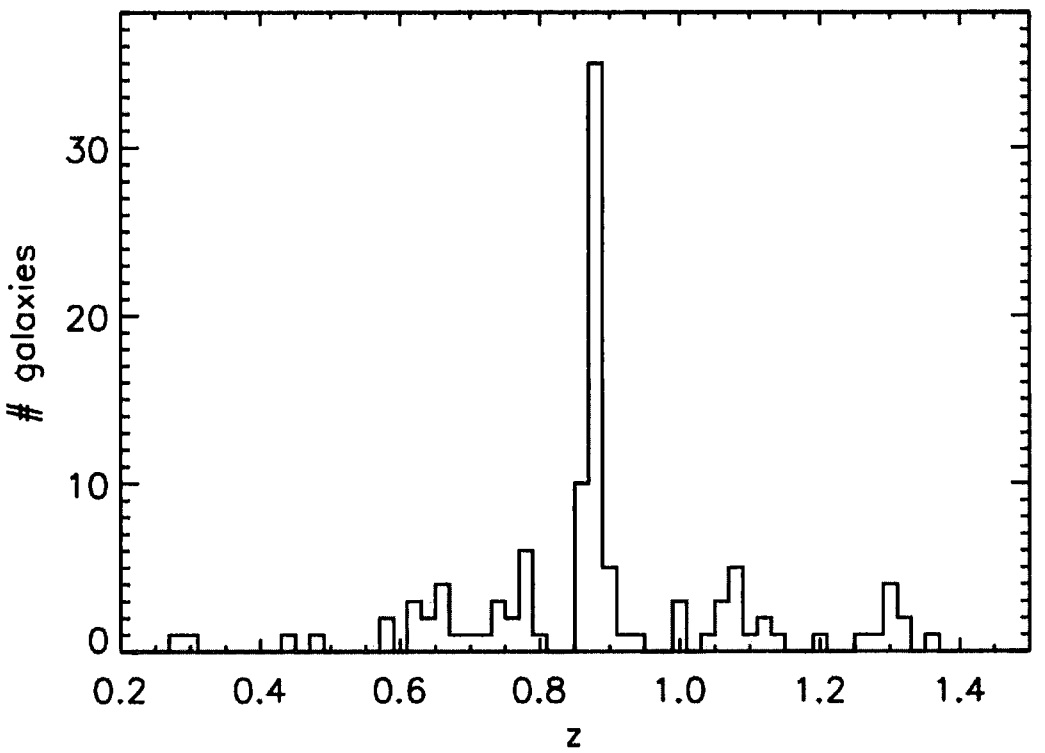

Figure 6.12: Redshift distribution for cluster members in the Elais N1 field (Swinbank et al., 2007).

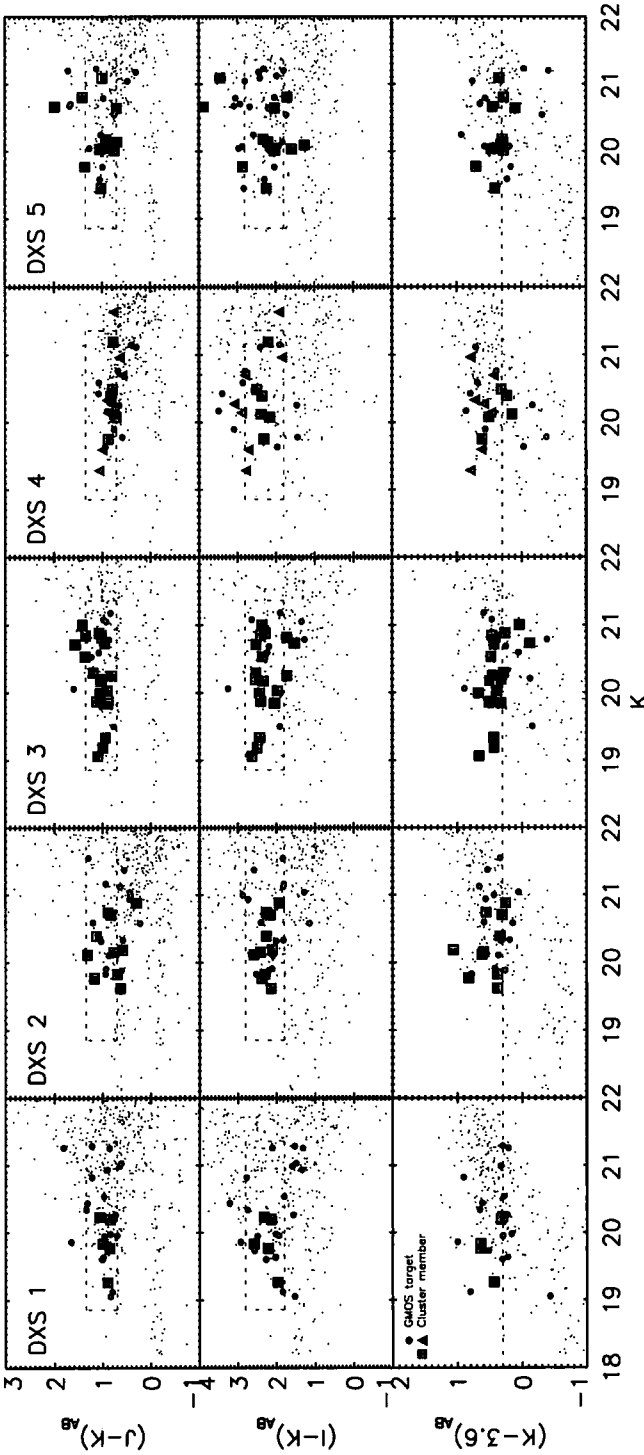

Figure 6.13: The colour-magnitude diagrams for our 5 Elais N1 cluster candidates which constitute the large scale supercluster. The spectroscopically confirmed members are highlighted.

6.6 Improvements to the algorithm and detection

There are clearly arguments to say that this simple algorithm is biased as we are predetermining the appearance of a high redshift cluster. For example we are assuming a circular core of diameter 1 Mpc. One solution to this could be to include an adaptive cluster aperture based on the total luminosity of the cluster members. The algorithm will be the basis for a study to discover $z \sim 0.5$ clusters in the Pan-STARRS all sky optical survey. It is currently being trained on a combination of SDSS and mock catalogues created from the semi-analytic models of Bower et al. (2006) based on Millennium N-body simulation (Springel et al., 2005).

The results themselves would also be improved by deeper and higher quality photometry. This would reduce the scatter in the observations of high-z red sequences improving the ease of detection by the algorithm. Greater coverage in further optical and infrared bands would improve the contrast between the cluster red sequence and field galaxies therefore pushing down the lower limit of the cluster mass detection to include poorer clusters and groups.

6.7 Summary

We have shown in this chapter that we have a simple, robust cluster detection algorithm that is successful in finding $z \sim 1$ clusters utilising 3 near-infrared and optical bands (I, J and K). We find a total of 15 cluster candidates in the Elais N1 field and 28 in SA22 which correspond to 19 and 9 clusters per sq. deg. respectively. We have confirmed utilising multi-object spectroscopy that our 5 strongest cluster candidates in the Elais N1 field comprise a $z \sim 0.9$ supercluster. With the presence of such a structure we conclude that Elais N1 is not an average field on the sky. If we assume, based on comparison with other studies, that the less cluster rich SA22 field is a more representative field and compare the cluster surface density to simulation we find that our algorithm is able to detect clusters in the mass range $10^{13.8}M_{\odot}$–$10^{15}M_{\odot}$. The lower limit to this range may be reduced with the aid of an improved algorithm in concert with higher quality multi-band photometry. This is important for future cluster mass function studies which may utilise the algorithm.

Data from these clusters are analysed and fed back into the BCG research in chapter 2 improving the high z cluster coverage of our sample and therefore the significance of our results. Further spectroscopic data on 5 more strong candidates in the SA22 field will be available in the near future and will hopefully confirm yet more high z clusters.

Chapter 7

Summary

7.1 Key results

In this thesis we provide a unified study of the evolution of rich galaxy cluster members across half the age of the Universe. This encompasses analyses of observations spanning 5 magnitudes of the elliptical/S0 red sequence from the Brightest Cluster Galaxies (BCGs) to the faint red galaxy population. We improve the significance of our results with additional high redshift clusters discovered by our cluster detection algorithm. In this way we create a consistent dataset which is used to constrain cluster galaxy evolution.

In chapter 2 we study the evolution and environment of BCGs in X-ray luminous clusters. The key result of this work is the discovery of a positive relationship between the near infrared luminosity of the BCG and the X-ray luminosity of its host cluster for the most X-ray luminous clusters. Previous studies have lacked the sample coverage of this work in the high X-ray luminosity regime required to observe this relation.

The K band Hubble diagram for the L_X corrected BCG sample is shown to follow passive evolution but this finding is not yet statistically significant. However, to improve the constraints on BCG evolution we include J-band photometry allowing us to compare the $J-K$ colour vs redshift to a set of models. We find that the high redshift BCGs appear to rule out passive evolution with a formation epoch less than redshift 2. We therefore expect that the stellar population of BCGs has

been in place since at least redshift 2, in agreement with the observations of Burke et al. (2000) and Nelson et al. (2002). By comparing the colour evolution to current semi-analytic models (De Lucia & Blaizot, 2007) we find the models to be too blue at high redshift. This suggests that these simulated BCGs form stars for a longer time period than those observed.

Our analysis of the red galaxy population in X-ray luminous clusters, in chapter 3, shows clear differences in the form of the luminosity function over the redshift range $z = 0.1$–0.5. These changes reflect an increase in the proportion of dwarf to giant galaxies in the population since $z \sim 0.5$ which we attribute to an increase in the number of dwarfs on the red sequence. We quantify this evolution using the luminosity function independent estimate of the relative evolution of the faint end, the red sequence Dwarf-Giant ratio (RDGR), which shows an increase by a factor of 2.2 ± 0.4 between $z = 0.54$ and $z = 0.13$. This is equivalent to an increase of 1.46 ± 0.14 in the relative V-band luminosity (or stellar mass) in faint red galaxies with $M_V \lesssim -20$ compared to brighter systems over this period. This increase means that in local clusters, the luminosity contributed by giant and dwarf galaxies is comparable, whereas at $z = 0.5$ the giants were the dominant population on the colour-magnitude relation.

Our results show that there is significant evolution since $z \sim 0.5$ in the faint passive galaxy population in a well-defined sample of X-ray luminous clusters. This agrees with the early results from De Lucia et al. (2004) and Kodama et al. (2004) on red galaxies in a more diverse range of structures. We conclude that a large proportion of the passive galaxy population at the faint end of the colour-magnitude sequence in local clusters either did not reside in similar, high-density environments 5-Gyrs ago (at $z \sim 0.5$) or, if they were present in these regions, then they had significantly bluer colours (suggesting they were actively star forming) and so do not fall within the colour-magnitude relation.

In Chapter 4 we confirm that the cluster red sequence slope is similar for clusters at the same redshift and evolves with redshift as seen in previous studies (Gladders et al. 1998, Lopez-Cruz et al. 2004). The observed slope evolution agrees with that expected from the build up of the red sequence. This causes the faint end of

the red sequence to be bluer compared to the bright end at high redshift as it is populated with less metal-rich galaxies. The metallicity differential along the red sequence decreases with age as the galaxies mature. As the red sequence is built up with progressively fainter galaxies this contributes to the slope evolution causing an increased gradient at high redshift. There may also be an age contribution to the slope from recent star forming galaxies transforming onto the sequence at the faint end.

We find our data to be in good agreement with slope evolution models we calculate from semi-analytical model of Bower et al. (2006) based on the Millennium N-body simulation (Springel et al., 2005). This confirms that such models that include feedback from active galactic nuclei are able to reproduce the observed cluster red sequence slope over the range of redshifts $0< z <1$.

When studying slope trends with other observables we see no relationship between red sequence slope and X-ray luminosity, velocity dispersion or BCG degree of dominance. This suggests that there is very little variation between the red sequence slopes due to the different cluster environments we consider. This confirms that searching for massive clusters using the colour magnitude relation is a viable method (Chapter 6, Barkhouse et al. 2006).

If we now combine the results from our BCG evolution and faint end studies we can begin to build up a unified picture of cluster member evolution. In this scenario the massive luminous galaxies within the cluster have been in place and passively evolving since their formation at high redshift ($z >2$) while the fainter red sequence population is being built up over cosmic time by in falling or transforming galaxies. This red sequence has a mass-metallicity gradient which manifests itself as a slope in colour-magnitude space, observed to be comparable for clusters at similar redshift and to evolve with time perhaps as a result of the red sequence build up.

We show in chapter 6 that drawing on the constraints provided by the above scenario we have created a simple, robust cluster detection algorithm that is successful in finding $z \sim 1$ clusters utilising 3 optical and near-infrared bands (I, J and K). We confirm spectroscopically that our first UKIDSS cluster candidates in the Elais N1 field comprise a $z \sim 0.9$ supercluster. Data from these clusters are analysed and fed

back into the BCG research in chapter 2 improving the high z cluster coverage of our sample and therefore the significance of our results. Further spectroscopic data on 5 more candidates in the SA22 field will be available in the near future and will hopefully confirm yet more high z clusters.

7.2 Plans for future research

By observing the colour evolution of the BCGs we find that they have been in place for at least the last 10 billion years and that current hierarchical merger models appear to continue star formation in the BCG for too long. We propose to increase and extend the high redshift coverage of this research using the BCGs we discover in the UKIDSS DXS to conclusively distinguish between evolution models.

The key result of Chapter 3 is that there has been a two fold increase in the number of dwarf red galaxies compared to giants in clusters over the last 5 billion years demonstrating that this dwarf population are either not present at high redshift or they are in the form of blue star forming galaxies. We intend to extend the study to a lookback time of 8 billion years and beyond using the highest redshift deep cluster data available from sources such as UKIDSS and XMM-LSS. This is to search for a continuation of this downsizing trend and therefore constrain the formation epoch of the less luminous red galaxies.

We will continue our research into the evolution of the red sequence slope by again increasing the redshift coverage. This study will provide improved constraints on the ever-evolving semi-analytic models, and more specifically their treatment of the mass metallicity relation along the red sequence.

The cluster finding algorithm we utilised in Chapter 6 will be used on the remaining UKIDSS DXS fields in combination with X-ray observations to look for additional high redshift candidates. We expect spectroscopic confirmation of the SA22 region clusters by the end of 2007. The algorithm will also be the basis for a study into clusters in the Pan-STARRS all sky survey and is currently being trained on mock catalogues created from semi-analytic models based on Millennium N-body simulation.

7.3 Concluding remarks

The key results of our study into the evolution of massive galaxy clusters are:

- There is a relation between the near-infrared luminosity of the brightest cluster galaxy (BCG) and the X-ray luminosity of the host cluster for the most X-ray luminous clusters.
- BCGs have been in place and passively evolving since at least redshift 2.
- There is a correlation between the presence of high luminosity H_α emission and blue near-infrared colour of BCGs. This provides a possible photometric technique for finding cool core clusters.
- We find that the number of dwarf galaxies on the red sequence has doubled since redshift 0.5. This suggests that these galaxies were either not present at high redshift or were in the form of blue star forming galaxies.
- The slope of the red sequence is comparable for clusters at similar redshift. This slope is seen to evolve as one would expect from an evolving mass-metallicity relation, in agreement with current semi-analytic models.
- We have developed an algorithm that draws on our cluster evolution research to successfully discover high redshift clusters based on their photometry. We have spectroscopic confirmation of 6 high redshift clusters, 5 of which constitute a supercluster.

7.4 Scientific Acknowledgements

In addition to the Acknowledgement section at the front of this thesis I include here several scientific acknowledgements.

This publication makes use of data products from the Two Micron All Sky Survey, which is a joint project of the University of Massachusetts and the Infrared Processing and Analysis Centre/California Institute of Technology, funded by the National Aeronautics and Space Administration and the National Science Foundation.

This work is based in part on data processed by CASU and WFAU obtained as part of the UKIRT Infrared Deep Sky Survey.

The United Kingdom Infrared Telescope is operated by the Joint Astronomy Centre on behalf of the Science and Technology Facilities Council of the U.K.

This work is based on observations obtained at the Gemini Observatory, which is operated by the Association of Universities for Research in Astronomy, Inc., under a cooperative agreement with the NSF on behalf of the Gemini partnership: The National Science Foundation (United States), the Science and Technology Facilities Council (United Kingdom), the National Research Council (Canada), CONICYT (Chile), the Australian Research Council (Australia), CNPq (Brazil), and CONICET (Argentina)

This work is based partly on observations obtained at the Hale 200 inch telescope at Palomar Observatory.

The Millennium Simulation databases used in this paper and the web application providing online access to them were constructed as part of the activities of the German Astrophysical Virtual Observatory.

Bibliography

Abell G. O., 1958, ApJS, 3, 211

Abell G. O., Corwin Jr. H. G., Olowin R. P., 1989, ApJS, 70, 1

Adelman-McCarthy J. K., Agüeros M. A., Allam S. S., Anderson K. S. J., Anderson S. F., Annis J., Bahcall N. A., Baldry I. K., et al., 2006, ApJS, 162, 38

Andreon S., 2006, MNRAS, 369, 969

Annis J., Kent S., Castander F., Eisenstein D., Gunn J., Kim R., Lupton R., Nichol R., et al., 1999, 31, 1391

Aragon-Salamanca A., Baugh C. M., Kauffmann G., 1998, MNRAS, 297, 427

Aragon-Salamanca A., Ellis R. S., Couch W. J., Carter D., 1993, MNRAS, 262, 764

Baldry I. K., Balogh M. L., Bower R. G., Glazebrook K., Nichol R. C., Bamford S. P., Budavari T., 2006, MNRAS, 373, 469

Bardeau S., Kneib J.-P., Czoske O., Soucail G., Smail I., Ebeling H., Smith G. P., 2005, A&A, 434, 433

Barkhouse W. A., Green P. J., Vikhlinin A., Kim D.-W., Perley D., Cameron R., Silverman J., Mossman A., et al., 2006, ApJ, 645, 955

Bertin E., Arnouts S., 1996, A&AS, 117, 393

Borgani S., Rosati P., Tozzi P., Stanford S. A., Eisenhardt P. R., Lidman C., Holden B., Della Ceca R., Norman C., Squires G., 2001, ApJ, 561, 13

Bower R. G., Benson A. J., Malbon R., Helly J. C., Frenk C. S., Baugh C. M., Cole S., Lacey C. G., 2006, MNRAS, 370, 645

Bower R. G., Lucey J. R., Ellis R. S., 1992, MNRAS, 254, 589

Bruzual G., Charlot S., 2003, MNRAS, 344, 1000

Burke D. J., Collins C. A., Mann R. G., 2000, ApJ, 532, L105

Butcher H., Oemler A., 1984, ApJ, 285, 426

Carlberg R. G., 1984, ApJ, 286, 403

Chabrier G., 2003, PASP, 115, 763

Clowe D., Bradač M., Gonzalez A. H., Markevitch M., Randall S. W., Jones C., Zaritsky D., 2006, ApJL, 648, L109

Collins C. A., Mann R. G., 1998, MNRAS, 297, 128

Courtney N. J. D., 2003, Ph.D. Thesis

Crawford C. S., Allen S. W., Ebeling H., Edge A. C., Fabian A. C., 1999, MNRAS, 306, 857

Dahlen T., Fransson C., Ostlin G., Naslund M., 2004, MNRAS, 350, 253

Davis M., Gerke B. F., Newman J. A., the Deep2 Team 2005, in Wolff S. C., Lauer T. R., eds, Observing Dark Energy Vol. 339 of Astronomical Society of the Pacific Conference Series, Constraining Dark Energy with the DEEP2 Redshift Survey. p. 128

De Lucia G., Blaizot J., 2007, MNRAS, 375, 2

De Lucia G., Poggianti B. M., Aragón-Salamanca A., Clowe D., Halliday C., Jablonka P., Milvang-Jensen B., Pelló R., et al., 2004, ApJL, 610, L77

De Lucia G., Poggianti B. M., Aragón-Salamanca A., White S. D. M., Zaritsky D., Clowe D., Halliday C., Jablonka P., et al., 2007, MNRAS, 374, 809

de Propris R., Stanford S. A., Eisenhardt P. R., Dickinson M., Elston R., 1999, AJ, 118, 719

Dressler A., Oemler A. J., Couch W. J., Smail I., Ellis R. S., Barger A., Butcher H., Poggianti B. M., Sharples R. M., 1997, ApJ, 490, 577

Driver S. P., Couch W. J., Phillipps S., 1998, MNRAS, 301, 369

Drory N., Feulner G., Bender R., Botzler C. S., Hopp U., Maraston C., Mendes de Oliveira C., Snigula J., 2001, MNRAS, 325, 550

Dye S., Warren S. J., Hambly N. C., Cross N. J. G., Hodgkin S. T., Irwin M. J., Lawrence A., Adamson A. J., et al., 2006, MNRAS, 372, 1227

Ebeling H., Barrett E., Donovan D., Ma C.-J., Edge A. C., van Speybroeck L., 2007, ApJL, 661, L33

Ebeling H., Edge A. C., Bohringer H., Allen S. W., Crawford C. S., Fabian A. C., Voges W., Huchra J. P., 1998, MNRAS, 301, 881

Ebeling H., Edge A. C., Henry J. P., 2001, ApJ, 553, 668

Ebeling H., Voges W., Bohringer H., Edge A. C., Huchra J. P., Briel U. G., 1996, MNRAS, 281, 799

Ellis S. C., Jones L. R., 2004, MNRAS, 348, 165

Elston R. J., Gonzalez A. H., McKenzie E., Brodwin M., Brown M. J. I., Cardona G., Dey A., Dickinson M., et al., 2006, ApJ, 639, 816

Epchtein N., de Batz B., Copet E., Fouque P., Lacombe F., Le Bertre T., Mamon G., Rouan D., et al., 1994, Ap&SS, 217, 3

Fabian A. C., 1994, ARA&A, 32, 277

Ferguson H. C., Binggeli B., 1994, 6, 67

Feulner G., Goranova Y., Hopp U., Gabasch A., Bender R., Botzler C. S., Drory N., 2007, MNRAS, 378, 429

Förster Schreiber N. M., Franx M., Labbé I., Rudnick G., van Dokkum P. G., Illingworth G. D., Kuijken K., Moorwood A. F. M., Rix H.-W., Röttgering H., van der Werf P., 2006, AJ, 131, 1891

Gal R. R., 2006, ArXiv Astrophysics e-prints

Giavalisco M., Ferguson H. C., Koekemoer A. M., Dickinson M., Alexander D. M., Bauer F. E., Bergeron J., Biagetti C., et al., 2004, ApJL, 600, L93

Gladders M. D., Lopez-Cruz O., Yee H. K. C., Kodama T., 1998, ApJ, 501, 571

Gladders M. D., Yee H. K. C., 2000, AJ, 120, 2148

Gladders M. D., Yee H. K. C., 2005, ApJS, 157, 1

Glazebrook K., Bland-Hawthorn J., 2001, PASP, 113, 197

Godwin J. G., Metcalfe N., Peach J. V., 1983, MNRAS, 202, 113

Goto T., Postman M., Cross N. J. G., Illingworth G. D., Tran K., Magee D., Franx M., Benítez N., et al., 2005, ApJ, 621, 188

Grebel E. K., 1999, IAU Symp 192, PASP, Eds P. Whitelock, R. Cannon, 192, 17

Haiman Z., Mohr J. J., Holder G. P., 2001, ApJ, 553, 545

Hogg D. W., Blanton M. R., Brinchmann J., Eisenstein D. J., Schlegel D. J., Gunn J. E., McKay T. A., Rix H.-W., et al., 2004, ApJL, 601, L29

Huang J.-S., Thompson D., Kümmel M. W., Meisenheimer K., Wolf C., Beckwith S. V. W., Fockenbrock R., Fried J. W., et al., 2001, A&A, 368, 787

Humphrey P. J., Buote D. A., 2006, ApJ, 639, 136

Jones L. R., Scharf C., Ebeling H., Perlman E., Wegner G., Malkan M., Horner D., 1998, ApJ, 495, 100

Kauffmann G., Charlot S., 1998, MNRAS, 294, 705

Kim R. S. J., Annis J., Strauss M. A., Lupton R. H., 2002, PASP, 28, 395

Kim R. S. J., Kepner J. V., Postman M., Strauss M. A., Bahcall N. A., Gunn J. E., Lupton R. H., Annis J., et al., 2002, AJ, 123, 20

Kodama T., Arimoto N., 1997, A&A, 320, 41

Kodama T., Yamada T., Akiyama M., Aoki K., Doi M., Furusawa H., Fuse T., Imanishi M., et al., 2004, MNRAS, 350, 1005

Koo D. C., Kron R. G., 1992, ARA&A, 30, 613

Kümmel M. W., Wagner S. J., 2001, A&A, 370, 384

Lane K. P., Almaini O., Foucaud S., Simpson C., Smail I., McLure R. J., Conselice C. J., Cirasuolo M., Page M. J., Dunlop J. S., Hirst P., Watson M. G., Sekiguchi K., 2007, MNRAS, 379, L25

Lawrence A., Warren S. J., Almaini O., Edge A. C., Hambly N. C., Jameson R. F., Lucas P., Casali M., et al., 2006, ArXiv Astrophysics e-prints

Lopez-Cruz O., 1997, Ph.D. Thesis, University of Toronto

Lopez-Cruz O., Barkhouse W. A., Yee H. K. C., 2004, ApJ, 614, 679

Markevitch M., Gonzalez A. H., Clowe D., Vikhlinin A., Forman W., Jones C., Murray S., Tucker W., 2004, ApJ, 606, 819

Natali F., Natali G., Pompei E., Pedichini F., 1994, A&A, 289, 796

Nelson A. E., Gonzalez A. H., Zaritsky D., Dalcanton J. J., 2002, ApJ, 566, 103

Neugebauer G., Leighton R. B., 1969, Two-micron sky survey. A preliminary catalogue. NASA SP, Washington: NASA, 1969

Perlmutter S., Aldering G., della Valle M., Deustua S., Ellis R. S., Fabbro S., Fruchter A., Goldhaber G., et al., 1998, Nat, 391, 51

Pimbblet K. . A., Smail I., Edge A. C., Couch W. J., O'Hely E., Zabludoff A. I., 2001, MNRAS, 327, 588

Pimbblet K. A., Smail I., Edge A. C., O'Hely E., Couch W. J., Zabludoff A. I., 2006, MNRAS, 366, 645

Pimbblet K. A., Smail I., Kodama T., Couch W. J., Edge A. C., Zabludoff A. I., O'Hely E., 2002, MNRAS, 331, 333

Poggianti B. M., Bridges T. J., Mobasher B., Carter D., Doi M., Iye M., Kashikawa N., Komiyama Y., et al., 2001, ApJ, 562, 689

Postman M., Lubin L. M., Gunn J. E., Oke J. B., Hoessel J. G., Schneider D. P., Christensen J. A., 1996, AJ, 111, 615

Reiprich T. H., Boehringer H., 2002, ApJ, 567, 716

Riess A. G., Filippenko A. V., Challis P., Clocchiatti A., Diercks A., Garnavich P. M., Gilliland R. L., Hogan C. J., et al., 1998, AJ, 116, 1009

Romanowsky A. J., Douglas N. G., Arnaboldi M., Kuijken K., Merrifield M. R., Napolitano N. R., Capaccioli M., Freeman K. C., 2003, Science, 301, 1696

Romer A. K., Viana P. T. P., Liddle A. R., Mann R. G., 2001, ApJ, 547, 594

Salpeter E. E., 1955, ApJ, 121, 161

Sandage A., Visvanathan N., 1978, ApJ, 225, 742

Sandage A. R., 1972, ApJ, 173, 585

Scharf C. A., Jones L. R., Ebeling H., Perlman E., Malkan M.; Wegner G., 1997, ApJ, 477, 79

Schechter P., 1976, ApJ, 203, 297

Schlegel D. J., Finkbeiner D. P., Davis M., 1998, ApJ, 500, 525

Skiff A. B., 2003, LONEOS catalogue, version 2003 Jul 15. Available via ftp://ftp.lowell.edu/p ub/bas/starcats/

Skrutskie M. F., Cutri R. M., Stiening R., Weinberg M. D., Schneider S., Carpenter J. M., Beichman C., Capps R., et al., 2006, AJ, 131, 1163

Smail I., Kuntschner H., Kodama T., Smith G., Pa ckham C., Fruchter A., Hook R., 2001, MNRAS, 323, 839

Smith G. P., Kneib J.-P., Ebeling H., Czoske O., Smail I., 2001, ApJ, 552, 493

Spergel D. N., Bean R., Doré O., Nolta M. R., Bennett C. L., Dunkley J., Hinshaw G., Jarosik N., et al., 2007, ApJS, 170, 377

Spergel D. N., Verde L., Peiris H. V., Komatsu E., Nolta M. R., Bennett C. L., Halpern M., Hinshaw G., et al., 2003, ApJS, 148, 175

Springel V., White S. D. M., Jenkins A., Frenk C. S., Yoshida N., Gao L., Navarro J., Thacker R., et al., 2005, Nat, 435, 629

Stanford S. A., Eisenhardt P. R., Dickinson M., 1998, ApJ, 492, 461

Stanford S. A., Romer A. K., Sabirli K., Davidson M., Hilton M., Viana P. T. P., Collins C. A., Kay S. T., et al., 2006, ApJL, 646, L13

Stott J. P., Smail I., Edge A. C., Ebeling H., Smith G. P., Kneib J.-P., Pimbblet K. A., 2007, ApJ, 661, 95

Strauss M. A., Weinberg D. H., Lupton R. H., Narayanan V. K., Annis J., Bernardi M., Blanton M., Burles S., et al., 2002, AJ, 124, 1810

Swinbank A. M., Edge A. C., Smail I., Stott J. P., Bremer M., Sato Y., van Breukelen C., Jarvis M., et al., 2007, MNRAS, 379, 1343

Taylor A. N., Dye S., Broadhurst T. J., Benitez N., van Kampen E., 1998, MNRAS, 501, 539

Terlevich A. I., Caldwell N., Bower R. G., 2001, MNRAS, 326, 1547

Thompson L. A., Gregory S. A., 1993, AJ, 106, 2197

Tormen G., 1998, MNRAS, 297, 648

van Breukelen C., Clewley L., Bonfield D. G., Rawlings S., Jarvis M. J., Barr J. M., Foucaud S., Almaini O., et al., 2006, MNRAS, 373, L26

van Dokkum P., Franx M., 2001, ApJ, 553, 90

van Dokkum P. G., Franx M., Kelson D. D., Illingworth G. D., 1998, ApJ, 504, L17

Visvanathan N., Sandage A., 1977, ApJ, 216, 214

Wake D. A., Collins C. A., Nichol R. C., Jones L. R., Burke D. J., 2005, ApJ, 627, 186

Wilson J. C., Eikenberry S. S., Henderson C. P., Hayward T. L., Carson J. C., Pirger B., Barry D. J., Brandl B. R., et al., 2003, in Iye M., Moorwood A. F. M., eds, Instrument Design and Performance for Optical/Infrared Ground-based Telescopes. Edited by Iye, Masanori; Moorwood, Alan F. M. Proceedings of the SPIE, Volume 4841, pp. 451-458 (2003). Vol. 4841 of Presented at the Society of Photo-Optical Instrumentation Engineers (SPIE) Conference, A Wide-Field Infrared Camera for the Palomar 200-inch Telescope. pp 451–458

Worthey G., Trager S. C., Faber S. M., 1995, ASP Conference Series, Volume 86, Fresh views of elliptical galaxies, Edited by Buzzoni, A. Renzini, A and Serrano, A, p. 203

Zwicky F., Kowal C. T., 1968, in CGCG6 "Catalogue of Galaxies and of Clusters of Galaxies", 1968, Volume VI Pasadena: California Institute of Technology. pp 0–+